NOTICE

The quality of this microform is heavily dependent upon the quality of the original thesis submitted for microfilming. Every effort has been made to ensure the highest quality of reproduction possible.

If pages are missing, contact the university which granted the degree.

Some pages may have indistinct print especially if the original pages were typed with a poor typewriter ribbon or if the university sent us an inferior photocopy.

Reproduction in full or in part of this microform is governed by the Canadian Copyright Act, R.S.C. 1970, c. C-30, and subsequent amendments.

AVIS

La qualité de cette microforme dépend grandement de la qualité de la thèse soumise au microfilmage. Nous avons tout fait pour assurer une qualité supérieure de reproduction.

S'il manque des pages, veuillez communiquer avec l'université qui a conféré le grade.

La qualité d'impression de certaines pages peut laisser à désirer, surtout si les pages originales ont été dactylographiées à l'aide d'un ruban usé ou si l'université nous a fait parvenir une photocopie de qualité inférieure.

La reproduction, même partielle, de cette microforme est soumise à la Loi canadienne sur le droit d'auteur, SRC 1970, c. C-30, et ses amendements subséquents.

Canada

Precision Measurements of the Magnetic Moment of Dilute Nickel Alloys

by

Donald Morris Hunter

BSc., Simon Fraser University, 1980

A THESIS SUBMITTED IN PARTIAL FULLFILLMENT

OF THE REQUIREMENTS FOR THE DEGREE OF

MASTER OF SCIENCE

in the department

of

Physics

SIMON FRASER UNIVERSITY

August 1988

ISBN 0-315-48756-9

APPROVAL

Name : Donald Morris Hunter

Degree : Master of Science

Title of Thesis : Precision Measurements of the Magnetic Moment of Dilute Nickel Alloys

Examining committee :

Chairman : M. Plischke

A. S. Arrott
Senior Supervisor

E. D. Crozier

G. Kirczenow

R. F. Frindt
Examiner

Date Approved : August 5, 1988

PARTIAL COPYRIGHT LICENSE

I hereby grant to Simon Fraser University the right to lend my thesis, project or extended essay (the title of which is shown below) to users of the Simon Fraser University Library, and to make partial or single copies only for such users or in response to a request from the library of any other university, or other educational institution, on its own behalf or for one of its users. I further agree that permission for multiple copying of this work for scholarly purposes may be granted by me or the Dean of Graduate Studies. It is understood that copying or publication of this work for financial gain shall not be allowed without my written permission.

Title of Thesis/Project/Extended Essay

Precision Measurements of the Magnetic Moment of Dilute Nickel Alloys

Author:

(signature)

Donald Hunter

(name)

18 Aug 1988

(date)

Abstract

A moving sample magnetometer system capable of making measurements of sample magnetic moment reproducible to 5 ppm was constructed. This system collects data under microcomputer control for applied fields in the range ± 12kG and sample temperatures within ± 10 K of ambient. High field ($8<|H(kG)|<12$) measurements at 290.45 K and 293.55K were made of the moment per gram of a number of dilute (0.1 to 1.5 at. %), substitutional Ni alloys, $Ni_{1-x}M_x$, where M is one of Ti, V, Cr, Mn, Fe, Co, Cu, Zr, Nb, Mo, Pd, Hf, Ta, W, Pt, or Au. These alloys were produced for muon spin rotation (μSR) studies, made at ambient temperatures, of the hyperfine field B_{hf}. In order to extract B_{hf} from the μSR frequencies it is necessary to subtract the Lorentz field $B_L = 4\pi M_S/3$ (where $M_S = M_S(T)$ is the spontaneous magnetization or moment per unit volume in the muon sample). The measurements described here allow an estimation of B_L for an alloy at a given temperature.

Samples were supplied in the form of accurately machined right cylinders with height to diameter ratios from ~ 1/2 to 1 and masses from ~ 2 to 5 grams. For each different size there was machined a matching Ni standard made of the Ni alloy base material whose chief impurity is 110 ppm Fe by weight. Measurements are taken with the sample's symmetry axis normal to the direction of the applied field. Sample shape, large grain sizes, and the presence, due to method of production, of macroscopic voids complicate the estimation of B_L. The effects of the sample's shape and magnetic images in the pole faces of the electromagnet used are minimized by measurement relative to matching standards. The large grain size and presence of voids result in a variation of apparent sample moment upon rotation about its symmetry axis. Accordingly, the average of twenty successive measurements, where each measurement is followed by a sample rotation of $\pi/10$, is taken as proportional to sample moment.

Recently a calculation of the concentration dependence of infinitely dilute, substitutional Ni transition metal alloys has been made. Assuming a simple power law temperature dependence of moment, where the exponent in the power law is the same for Ni and its alloys, our room temperature results are corrected to 0 K and compared with results of the above calculation.

To

Jean Melinda Hunter

Acknowledgements

This work and its author have gained much from their association with Tony Arrott.

Calvin Winter originally designed and constructed the moving sample magnetometry system and the subsequent efforts of Al Kleinschmidt improved its performance considerably.

My thanks to Robert I. Grynszpan and his group at ENSAM for supplying the samples and the results of measurements which served to characterize them.

The encouragement and advice of many people made substantial contribution to the best of this thesis. My thanks to Frank Wick and Stephen Purcell for yeoman service in this regard.

Technical assistance, in the forms of machining, electronics, and support buoy this work. I have learnt much from and appreciate the patience and good humour displayed by the technical staff of this university. The coil mount(s) owe their existence to the generosity and skill of Mark Holzer who on two occasions machined from dusk til dawn during the Xmas break of 1986. I gratefully acknowledge the artful assistance of Ken Urquhart in matters analytical and otherwise.

Boredom was seldom a problem, thanks to the crop of fine fellows; Steve, Jeff, Ken, Mahesh, Ross, Brett, John, Terry, Les, Rudolf,.....

Table of contents

Chapter 3. Results and discussion

List of tables

List of figures

Chapter 1. Introduction

This thesis describes measurements of magnetic moment made using a moving sample magnetometer (MSM). This chapter begins with an introduction of the basic idea of MSM. A brief overview of relevant magnetic concepts and theory is then presented. Finally the motivation for the experiments is considered.

1.1 Moving sample magnetometer

Two common approaches to determining magnetic moments are the induction and force methods. The first relies on Faraday's law and hence involves relative motion while the second relies on the force exerted on a magnetic moment in a field gradient. These two methods return information about the magnetic moment of the sample as a whole. Their relative merits are discussed by Foner[1]. In either case, a sample's shape and its orientation with respect to the direction of an applied magnetic field are of great importance. Most importantly, as will be discussed in the theory section below, these two considerations affect the uniformity of the direction of magnetization (magnetic moment/unit volume) over the sample's volume.

The MSM is a high precision version of the induction method. MSM finds its origins in the extraction method of Weiss and Forrer[2]. With this method the change in flux upon extracting a sample from a coil system fixed between the pole faces of an electromagnet is measured by the deflection of a ballistic galvanometer. Here the galvanometer effectively integrates the induced emf, the deflection being taken as proportional to sample moment. For the MSM described here, a voltage is obtained by integration, employing active electronics, of the voltage induced in stationary coils by the motion of a sample relative to them. The resulting integrated voltage is directly proportional to the sample's magnetic moment. Unfortunately, as will be described below, the pole faces of the electromagnet used render the proportionality constant field dependent.

The coil configuration used is shown below in fig. 1.1. The sample is moved vertically from midway between one pair to the other. As indicated by the arrows the coils within a pair couple to the sample in the same sense, while upper and lower pairs are connected in opposition. Coils have the largest possible diameter that the constraint of a fixed 2 inch stroke length will allow. Coil separation within a pair is as small as possible, being limited by the requirement that coils be mounted independently of the part of the apparatus concerned with sample motion. This ensures that the impulse associated with sample motion imparts as little in the way of microphonics as possible to the signal. Moreover, this separation is close to the Helmholtz separation, which (along with the large coil diameters relative to sample size) makes the signal less sensitive to sample positioning. The use of two such pairs has two advantages. Firstly the voltages induced in each pair of coils by the motion of the sample are of the same sense, so that the total signal is twice that obtained with a single pair of coils as shown in the inset. More importantly, voltages due to time variations of the applied field buck between upper and lower pairs.

A sample moving vertically between stationary endpoints located between upper and lower pairs induces across them a voltage

$$V(t) = -\frac{\partial}{\partial t}\int_S \mathbf{B}\cdot\mathbf{dA} \ ,$$

where **B** is the magnetic field associated with the magnetized sample. The integral, representing the instantaneous flux through the coils in their frame, is over the surface S spanning the four pickup coils. The above voltage is integrated in time from before the sample starts to move until sufficiently long after the sample comes to rest at 2 that any time variation of flux is negligible (due to either decaying eddy currents or magnetic aftereffects in the pole faces). This integrated voltage, excluding an instrument related offset voltage described below, is proportional to the sample moment (assumed to be the same at the positions 1 and 2). This result is independent of the path taken between endpoints.

Fig. 1.1

Basic principle of the MSM; motion yields induced signal (shown inset) the time integral of which is proportional to sample magnetic moment.

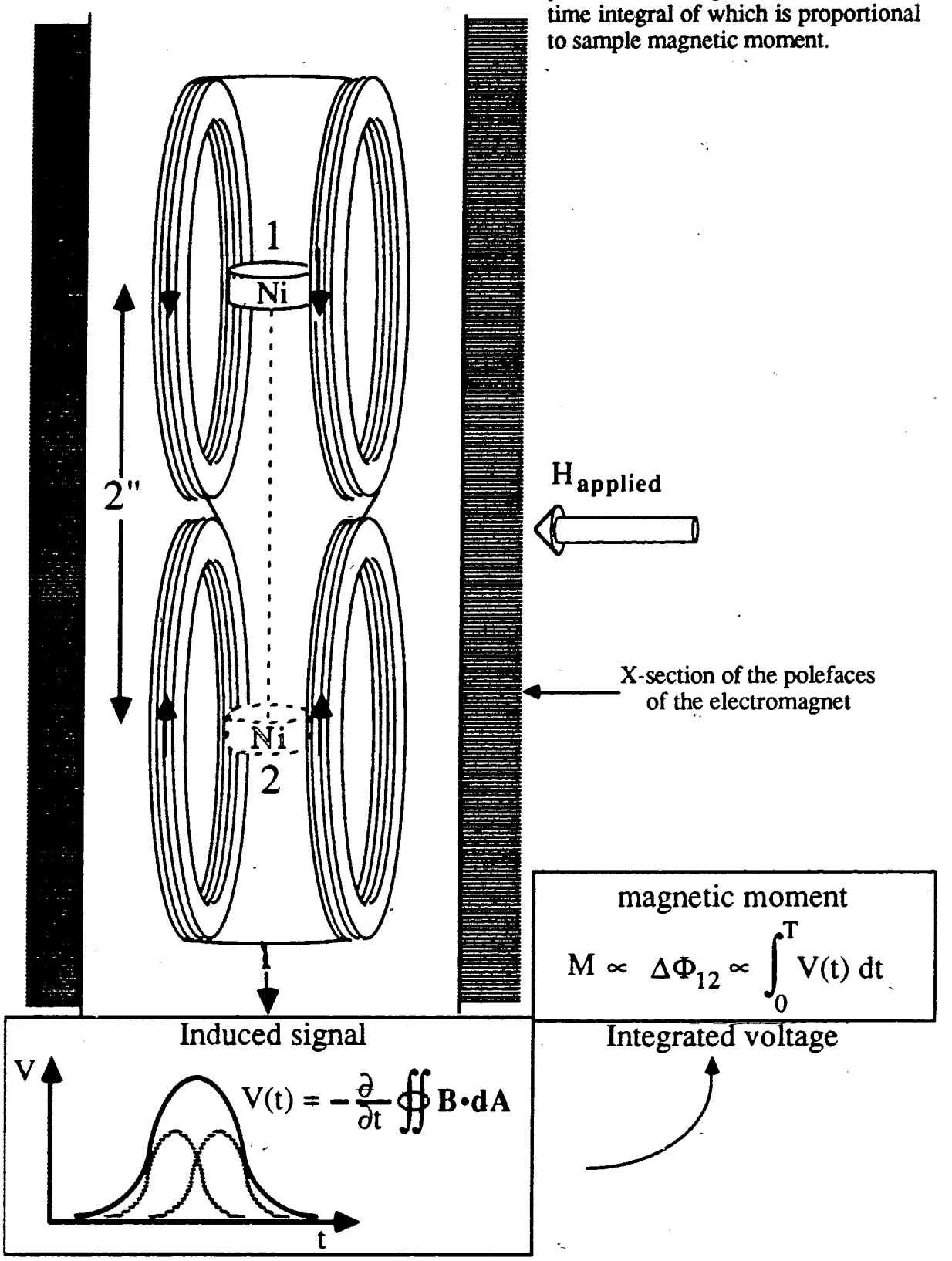

Before further discussion of the measurements and their motivation, relevant aspects of magnetic theory are considered.

1.2 *Magnetic concepts and theory*

The fundamental concept is that of the magnetic moment. Classically it is a quantity that arises naturally when considering the average magnetic field produced by a system of charges describing stationary orbits[3]. The magnetic moment **m** (assuming that all particles have the charge to mass ratio e/m and that v « c) may be written,

$$\mathbf{m} = \frac{e}{2mc}\sum \mathbf{r} \times \mathbf{p}, \qquad (1.1)$$

where the sum is over particles. Note the relationship between **m** and the angular momentum **L** = **r** x **p**. An equivalent description in terms of continuous current densities **j** is

$$\mathbf{m} = \frac{1}{2c}\int \mathbf{r} \times \mathbf{j}\, dV. \qquad (1.2)$$

It follows that a linear current, I, flowing in a planar loop which encloses an area, A, produces a magnetic moment of magnitude IA/c whose direction is normal to the plane in the sense given by the right hand rule. The vector potential, **A**, of the far field associated with any magnetic moment **m** is given by the purely dipolar expression

$$\mathbf{A} = \frac{\mathbf{m} \times \mathbf{r}}{r^3}. \qquad (1.3.1)$$

At a point **r** away from a dipole moment **m**, is a magnetic induction (given by the curl of (1.3.1)) of

$$\mathbf{B}(\mathbf{r}) = \frac{3\mathbf{m}\cdot\mathbf{r}}{r^5}\mathbf{r} - \frac{\mathbf{m}}{r^3}. \qquad (1.3.2)$$

At this point it is necessary to draw a distinction between macroscopic and microscopic current densities. The former is associated with the mean drift velocity of free charge carriers resulting from the presence of an electric field while the latter is everything else (often referred to as bound currents). These two contributions are represented as the curls of two corresponding fields, so that the total current density is the sum,

$$\mathbf{j}_{free} + \mathbf{j}_{bound} = \frac{c}{4\pi}\nabla \times \mathbf{H} + c\,\nabla \times \mathbf{M}. \qquad (1.4)$$

Expressing the magnetic field **B** as $\mathbf{H} + 4\pi\mathbf{M}$ allows Ampere's law for magnetostatics ($\partial E/\partial t = 0$) to be written in a form suitable for practical application: $\nabla \times \mathbf{H} = 4\pi\mathbf{j}_{free}/c$. Substituting $\mathbf{j}_{bound}$ into (1.2) above gives[4]

$$\mathbf{m} = \int \mathbf{M}dV. \qquad (1.5)$$

So the magnetization **M** is the volume density of magnetic moment not due to free currents. Associated with **M** are $-\mathbf{M}\cdot\mathbf{H}$ and $\mathbf{M} \times \mathbf{H}$, respectively, the energy and torque densities in an applied field **H**.

Ferromagnetic materials, such as Fe and Ni and their dilute alloys, are characterized by a state of spontaneous magnetization (in the absence of an externally applied magnetic field). This state is stable up to a critical temperature above which the material becomes paramagnetic. This magnetization results from interactions between the electrons in these structures. In analogy to the classical moment discussed above there are quantum mechanical moments associated with the electron's spatial and internal degrees of freedom. Electrons possess an intrinsic spin angular momentum, $|S| = \hbar/2$. Associated with an electron's spin is a magnetic moment of magnitude $\mu_B = e\hbar/2mc \approx 6(10^{-9})$ eV/G (Bohr magneton). Similarly there is a moment associated with the

orbital (spatial) angular momentum, **L**, of the electrons. However it turns out that for the materials considered here the spatial angular momentum is of secondary importance. The crystalline field of the structure largely removes the degeneracy of **L** states. Expectation values are zero for nondegenerate states. The angular momentum **L** is said to be quenched[5].

Foremost of the interactions, solely responsible for the existence of spontaneous magnetization, is the exchange interaction. This interaction is related to the following fact: identical particles are indistinguishable. As a consequence of the above, a system of two or more noninteracting particles must be represented by state functions that are either antisymmetric or symmetric with respect to the exchange (of the spatial and spin coordinates) of any two of the particles. Electrons, along with all particles of half integral spin (known as Fermions), exhibit the antisymmetric behaviour. The particular details of the application of the above idea to a given system are not important here. Only the basic result is of importance; exchange forces the coulomb energy of a system of electrons to depend on the total spin of the system. As a consequence of the above, energy varies with the relative orientation of neighbouring spins. For ferromagnets parallel alignment of neighbouring spins is the lowest energy state. The exchange interaction may be thought of in terms of an effective field, where this field provides a restoring torque which tends to bring adjacent spins into alignment. In Fe and Ni, at absolute zero, saturation (all moments aligned) magnetizations, M_S, of the order of 2.2 and 0.6 μ_B/atom are observed.

For a crystalline structure the magnetization can be given in units of Bohr magnetons per atom, the volume being implied by knowledge of the lattice parameters. It is common terminology to refer to the mass density of magnetic moment, σ, as magnetization, also. Which of σ or $M = \sigma\rho$ (where ρ is the density of the material) is being referred to as "magnetization" is clear from context.

Phenomenological approach

A microscopic description of metallic magnetism is a formidable task when exchange alone is considered. Throughout most of this thesis magnetization processes are considered from a phenomenological point of view. This viewpoint rests on the following two facts. At a given temperature below T_c the direction of the magnetization $M_s(T)$ varies slowly on the atomic scale. Secondly, the magnitude of the spontaneous magnetization is a very weak function of the applied magnetic field. Together these facts allow the magnetization to be represented by a continuous unit vector field. A phenomenological approach, known as micromagnetics (pioneered by W.F. Brown[6]), employs variational energy minimization procedures to model magnetic interactions over such a field. The number of specific problems that may be solved with this approach is limited by available computing power and the age of the universe. However, the results of applying energy arguments to simple systems provide qualitative answers to questions asked of the actual (complex) systems considered here. For example, in order to model the behaviour of polycrystalline samples, an approximate averaging procedure may be used[7]. The primary influences on the direction of magnetization are now presented.

Considering only exchange, which is independent of the orientation with respect to the crystalline axes, the thermodynamic state of a crystal is a function of only the magnitude of $\mathbf{M}$[4]. In general however there are anisotropies, so that $\mathbf{M}$ and $\mathbf{H_a}$ (an externally applied field) are seldom in the same direction.

Magnetocrystalline anisotropy

There exists a coupling between an electron's spin and its orbital angular momenta. In the rest frame of a bound electron there is a magnetic field due to the motion of the charged nucleus about it. The energy of the electron spin in this field as produced in a magnetic metal effectively couples the spin to the symmetry of the lattice. This coupling results in preferred directions (with respect to the crystal axes) for magnetization. For cubic crystals a magnetocrystalline anisotropy

energy density, E_K, may be written phenomenologically[8] as,

$$E_K = K_1(\alpha_1^2\alpha_2^2 + \alpha_2^2\alpha_3^2 + \alpha_3^2\alpha_1^2) + K_2\alpha_1^2\alpha_2^2\alpha_3^2 + \ldots \ , \qquad (1.6)$$

where the α_i's are direction cosines of the magnetization with respect to the lattice. The parameters K_1 and K_2 are known as the first and second anisotropy constants (functions of temperature) respectively. Typically, the magnitude of K_i decrease with increasing i. Considering only the first term of (1.6) energy minima occur in the six <100> (as is the case for Fe) and eight <111> (as is the case for Ni) "easy" directions (all other directions being "harder") for positive and negative K_1 respectively. Experimentally determined values[9] are, for Fe; $K_1 = 4.81(10^5)$, $K_2 = 1.2(10^3)$ and for Ni; $K_1 = -5.5(10^4)$, $K_2 = -2.5(10^4)$, in units of erg/cc. The total energy density may be written,

$$E = -\mathbf{H}\cdot\mathbf{M} + E_K \ . \qquad (1.7)$$

The field dependence of the direction of **M** is determined by minimizing the total energy (1.7). Consider for example application of a field in a {100} plane, in a direction other that along an easy axis. The direction that **M** takes is determined by a balance between opposing torques due to crystalline anisotropy and the applied field **H**. In a cube face the expression (1.6) reduces to $E_K = 2K_1\cos^2\theta\sin^2\theta$, where the second term has been neglected (a good assumption for Fe) and θ is the angle that the magnetization, **M**, makes with an easy direction (<100> for $K_1 > 0$). For $K_1 > 0$ magnetization prefers to lie along a cube edge. The picture in a cube face is shown in the vector diagram below.

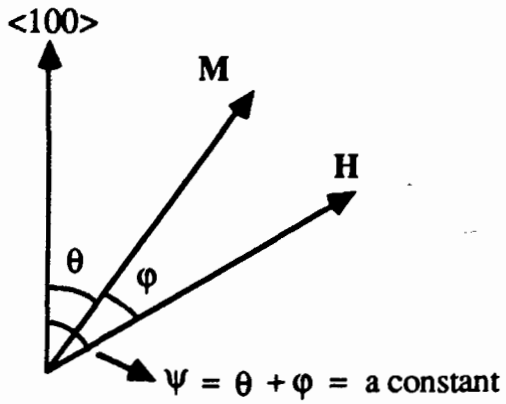

where $|\mathbf{M}| = M_s$ and the above expression for E_K applies. The total energy density is

$$E = 2K_1\cos^2\theta\sin^2\theta - M_sH\cos\varphi\ .$$

Equilibrium states are given by $\partial E/\partial\theta = 0$. Consider the stability of the two states $\pm M_s$ when **H** is in either direction along an easy axis; corresponding to values for ψ of 0 and π. Stability is assured when $\partial^2E/\partial\theta^2 > 0$. Consider the sign of $\partial^2E/\partial\theta^2$ near the four states given by $\theta = 0$ and $\theta = \pi$ for $\psi = 0$ and $\psi = \pi$. Schematically the situation may be represented as,

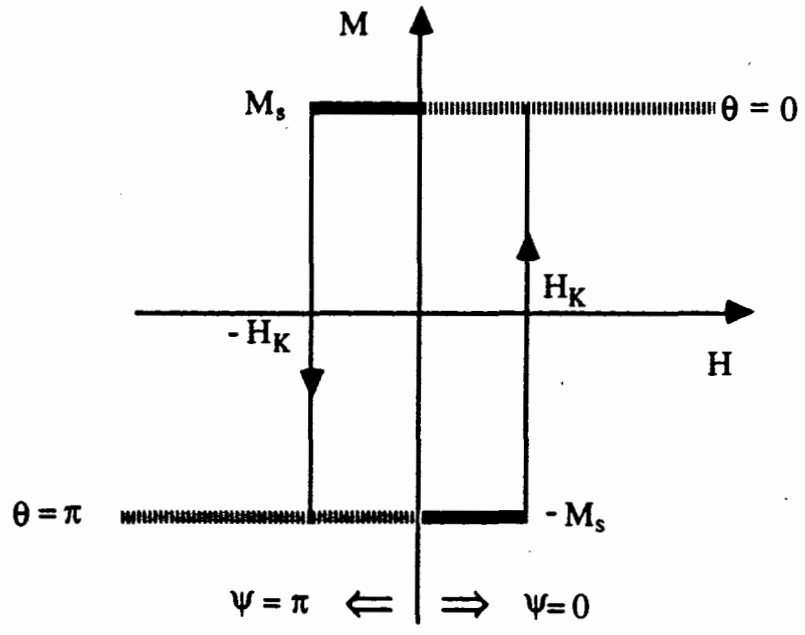

where $M = M_S\cos\varphi$ and the quantity $2K_1/M_S$ is referred to as the anisotropy field, H_K. The four stability regions are indicated by the heavy lines. There are sudden jumps of the moment direction at $\pm H_K$. This field behaviour, irreversible in both the sense of field cycling and thermodynamically (system passes through non-equilibrium states in such a rapid fashion at the fields $\pm H_K$ that the change cannot be made isothermally), is a simple example of a common phenomenon called hysteresis. Such hysteresis always accompanies cubic anisotropy.

In general the field at which the magnetization is reduced to zero is known as the coercive field, H_c (usually it is understood that saturation has been reached).

Approach to saturation

For field directions other than along the easy or hard directions $H \rightarrow \infty$ is required to reach saturation ($\pm M_S$). The field dependence of the approach to saturation due to crystalline anisotropy, where the approximation $M = M_S(1 - \varphi^2)$ is valid, is obtained by identifying (from the torque balance equation with $\sin\varphi \sim \varphi$) $\varphi = (-1/M_S H)(\partial E_K/\partial\varphi)_{\varphi = 0}$. So that the approach to saturation goes like

$$M(H) = M_S\left(1 - \frac{b}{H^2}\right), \qquad (1.8)$$

where the value of b depends on the form of E_K. Simply stated the above reflects the fact that in order to overcome a finite opposing torque with the field torque going as $\sin\varphi$ an infinite applied field is required. This argument applies no matter what the source of the torque (e.g. for shape anisotropy discussed below).

In higher fields M is found to have a 1/H field dependence. This is attributed to the presence of inclusions with different M_S and structural imperfections. These and other contributions to the approach to saturation are discussed in the review by Stoner[10].

Dipolar interactions

The energy of two dipole moments, $\mathbf{m}_1$ and $\mathbf{m}_2$, separated by a distance $\mathbf{r}$ is[11],

$$U = \frac{1}{r^3}[\mathbf{m}_1\cdot\mathbf{m}_2 - 3(\mathbf{m}_1\cdot\hat{\mathbf{r}})(\mathbf{m}_2\cdot\hat{\mathbf{r}})]. \qquad (1.9)$$

An estimate of the magnitude of U in solids can be made by assuming a moment of 1 μ_B per atom and an interatomic distance, r, of 2 Å, is given by $\mu_B^2/r^3 \sim 10^{-4}$ eV. Accordingly, if the moment alignment in ferromagnets were dipolar in origin, Curie temperatures would be ~ 1 K (assuming $U \sim k_B T_C$). However, the r^{-3} dependence is long ranged relative to the exchange interaction, so that the dipolar interaction becomes increasingly important with increasing crystal size.

Demagnetizing field

From the viewpoint of micromagnetics[6], in the absence of crystalline anisotropy, the total energy density at a point $\mathbf{r}$ is

$$E(\mathbf{r}) = -\mathbf{M}\cdot\mathbf{H} + \frac{1}{2}\nabla\cdot\mathbf{M}(\mathbf{r})\int\frac{\nabla\cdot\mathbf{M}(\mathbf{r}')}{|\mathbf{r} - \mathbf{r}'|}d^3\mathbf{r}', \qquad (1.10)$$

where $\mathbf{r}$ and $\mathbf{r}'$ are field and source points respectively (the 1/2 factor prevents double counting). Dipole-dipole interactions account for the second term, its value depending on the external shape (limits of integration) of the crystal. Its effect is best seen by considering a simple example; a uniformly magnetized (to saturation) sphere. The divergence of $\mathbf{M} = M_S\hat{\mathbf{z}}$ at the surface is equivalent to a surface charge density. These charges produce, within the sphere, a "demagnetizing" field $\mathbf{H}_{dem} = -4\pi M_S/3\,\hat{\mathbf{z}}$ which is uniform over its volume, V. So, in the absence of an applied field, the field at any point within the sphere, $B_i = 4\pi M_S - 4\pi M_S/3 = 8\pi M_S/3$. The field external to the sphere is that of a magnetic dipole moment at the centre of the sphere of magnitude $M_S V$. A similar situation exists for the converse of the above, that is a spherical void within a space of uniformly magnetized material. The field inside the cavity,

known as the Lorentz field[12], is $\mathbf{B}_L = 4\pi M_s/3\ \hat{\mathbf{z}}$. Now consider the dipole energy of a spherical volume, V_c, of material anywhere within a uniformly magnetized sphere. The energy of this dipole moment, $M_s V_c$, is zero since the field at the dipole is $\mathbf{B}_L + \mathbf{H}_{dem} = 0$ (ignoring the $8\pi M_s/3$ contribution due to the dipole itself). So the dipole-dipole energy of the uniformly magnetized sphere is zero.

For any uniformly magnetized ellipsoid of revolution, there exists a uniform demagnetizing field, $\mathbf{H}_{dem} = -4\pi(D_\perp M_\perp + D_{||} M_{||})$, where the two D's are the demagnetizing factors corresponding to the components of **M** along and normal to the symmetry axis. Values of D vary between the limits of 0 for a long needle magnetized along its length, and 1 for flat pancakes magnetized normal to the flat surface. For the uniformly magnetized sphere there is a single D = 1/3. For ellipsoids of revolution, the internal field $\mathbf{B}_i$ may be written

$$\mathbf{B}_i = (\mathbf{H}_a - \mathbf{H}_{dem}) + 4\pi\mathbf{M} = \mathbf{H}_a + 4\pi(1 - D)\mathbf{M}, \qquad (1.11)$$

where $\mathbf{H}_a$ is an externally applied field, $|\mathbf{M}| = M_s$, and the term in brackets is the internal field $\mathbf{H}_i$. Dipole-dipole energy (second term of (1.9)) here is $4\pi M_s(1/3 - D)$.

In general, demagnetizing fields vary in both magnitude and direction over the volume of an arbitrarily shaped crystal. Their distribution is determined by a minimization of the total free energy. Such calculations involve a 6-fold integration and so are readily done only for highly symmetrical cases.

Shape anisotropy

For the above situation $\mathbf{H}_a \,||\, \mathbf{M}$ only for $\mathbf{H}_a$ along a principal axis. In this case one speaks of a uniaxial shape anisotropy, where the equilibrium state of the sample (disregarding crystalline anisotropy for the moment) is determined by the balance of torques due to $\mathbf{H}_{dem}$ and $\mathbf{H}_a$. The anisotropy field in this case is $4\pi(D_\perp - D_{||})M_s$.

The response in, say, the z direction, of an isotropic material to the driving force, $(H_i)_z$, is indicated by either the permeability, $\mu_z = (B_i)_z/(H_i)_z$, or the susceptibility, $\chi_z = (M)_z/(H_i)_z$. For simplicity consider an ellipsoid of revolution magnetized along a principle axis for which (1.10) is the simple scalar relation, $B_i = H_a - 4\pi(1-D)M$ and $M = \chi H_i$ (or $B_i = \mu H_i$ where $\mu = 4\pi\chi + 1$).

In order to reduce the magnetostatic energy , $-M \cdot H$, H_i should be kept as small as possible. Materials which have $H_c = 0$ and below saturation approach the ideal of $\chi \rightarrow \infty$ are said to be magnetically soft (Ideally Soft Materials ISM). In this limit the internal field H_i would be zero. This may be viewed as a negative feedback or bootstraping situation in which M_i increases just enough to balance the change in H_a that caused it. A circuit analogy is shown below.

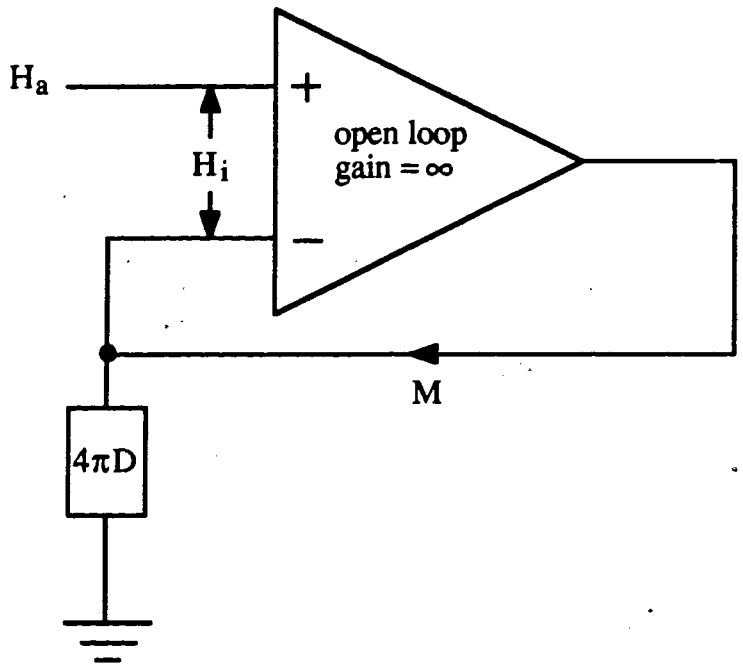

For an ISM, M versus H_i becomes the linear function $M = (1/4\pi D)H_a$ between the saturation states $\pm M_s$. In principle this allows the calibration of magnetization in terms of H_a. In fact the low field slope of the magnetization curve of structurally and chemically pure Fe and Ni spheres may be used to calibrate induction type magnetometers[13]. Note that this method assumes that magnetic "images" (see below) do not change with field.

Domains

Until now, in the absence of shape anisotropy, the lowest energy state has been assumed to occur for a crystal uniformly magnetized along an easy direction. With increasing size it becomes energetically favourable to break this uniform state up into a number of smaller volumes, known as magnetic domains, each uniformly magnetized (known as spontaneous magnetization) in an easy direction such that $\nabla \cdot \mathbf{M} = 0$ throughout the crystal (thereby removing the 2nd term of (1.10)). For this discussion it is convenient to picture the magnetization **M** as made up of magnetic moments, or spins, localized on lattice sites of the crystal. Between domains, are regions known as domain walls where spins change orientation from that of one domain to the next in such a way that $\nabla \cdot \mathbf{M} = 0$. It turns out that an abrupt reorientation, occurring between two adjacent spins, one in each of the two domains, is unnecessarily costly in exchange energy. In fact the width of domain walls, in the absence of applied and crystalline anisotropy fields, is limited only by magnetostatics. Crystalline anisotropy acts to limit the extent or width of domain walls, the increase in this energy eventually outweighing the decrease in exchange energy. Such a domain structure reduces crystal energy by reducing the energy of all spins by a small amount, while increasing the energy of only a small number of spins (those making up domain walls) by a relatively large amount.

Armed with the above concepts we now turn to a discussion of the processes of magnetization that occur when a magnetic material is subjected to an externally applied field.

Technical magnetism

Domain structure was first postulated in order to explain the magnetization, by the application of an external field, of a piece of "unmagnetized" material.

Consider what happens if a field is applied along the [100] easy direction in an unmagnetized single crystal of Fe. Spins that make some angle with the [100] direction will experience a torque. This includes domain wall spins and the spins of domains oriented at right angles to the [100] direction. Focus on what happens at the 180 deg. domain wall, known as a

Bloch wall, that separates two adjacent regions magnetized in the [100] and [$\bar{1}$00] directions. Imagine a plane of spins running through and normal to a 180 deg. Bloch wall. This wall is characterized by the fact that spins reverse direction only by turning out of the plane. Wall spins, in aligning themselves with the [100] direction, will, due to the exchange interaction between adjacent spins, drag adjacent spins with them. This results in the displacement of the wall into the [$\bar{1}$00] region, reversing spins as it goes. Meanwhile whole domains oriented normal to these, attempt to rotate against anisotropy torques (due to either shape or crystalline ($2K_1/M_S$) fields). The relative ease with which domain walls move and domains of the above sort rotate will determine the evolution of the magnetization of the crystal as a whole as the applied field is increased in magnitude.

The form of the hysteresis curves for magnetically "soft" Fe and Ni is now described. In pure (structurally and chemically) single crystals of Fe and Ni, domain wall motion occurs long before the field is large enough to begin rotating unfavourably oriented domains. The [$\bar{1}$00] domains are reversed in internal fields of the order of a small fraction of a gauss. The initial differential susceptibility, defined as $\chi_{diff,i} = (\partial M/\partial H)_{H=0}$, is relatively large in such materials. As the field is increased χ_{diff} increases to a maximum, $\chi_{diff,m}$, thereafter decreasing to zero in the limit $H_a \rightarrow \infty$ where all moments are aligned with the field.

The region in which χ_{diff} decreases is known as the "knee" of the hysteresis curve. For these materials (and in general) the path followed from the demagnetized state to a state near saturation ($M_S - M \ll M_S$: referred to as "technical" saturation), referred to as the "virgin" curve, is not retraced as the field is cycled between extremes. However, after a few cycles the curve, known as a "major loop", becomes reproducible. On decreasing $|H_a|$ the magnetization does not decrease as rapidly as it increased, having a value for $|H_a| = 0$, M_r , known as the remanence. The hysteresis curve, which passes through the points $(0,\pm H_c)$ and $(\pm M_r,0)$ is generally symmetrically placed about the origin. Features of the hysteresis curve described above are shown graphically below.

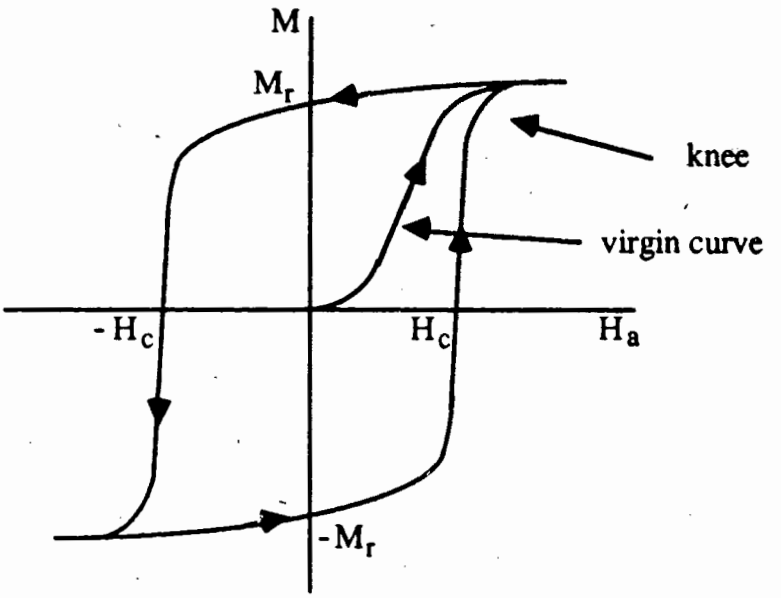

The following are some experimentally determined[14,9] magnetic parameters of pure, well annealed Fe and Ni at room temperature:

Table 0:*Room temperature magnetic parameters of Ni and Fe*

	Fe	Ni
$4\pi M_s$(G)	1580	6000
H_K(Oe)	560	230
H_c(Oe)	0.01	0.7
μ_{max}	350000	600

where $H_K = 2K_1/M_s$ and, μ_{max} is the maximum effective (i.e.B/H) permeability (which is defined as the slope of a straight line form the origin to the point at which it just touches the magnetizing part of the hysteresis curve). For Fe, with increasing concentration of impurities such as C and N, μ_{max} decreases while H_c increases.

The situation in which fields are cycled between symmetric limits whose magnitude is less than that required to achieve technical saturation is now considered. The loop described follows the major loop, departing only when $|H_a|$ is decreased, then joining it again upon sufficient field reversal. As these limits increase, for the part of the curve where $|H_a|$ decreases, permeability decreases for a given field. A schematic representation of the upper part of two such loops obtained on cycling the field between symmetric limits of ±12 kG and ±13 kG is shown below.

Note that as $|H_a|$ decreases the permeability for the ±12 kG curve is greater than that of the ±13 kG.

1.3 Motivation

Hyperfine field at a muon

A series of dilute alloys starting from high purity Ni were made by R.I. Grynszpan et al.[15] for the purpose of studying muon spin rotation (μSR) and positron annihilation. The muon technique used returns information about the local magnetic field, B_μ, at the interstitial sites occupied by a μ^+ during its lifetime ($\tau_\mu = 2.2\mu$sec). The mobility of the μ^+ at the ambient temperatures used is such that an average over all interstitial sites is taken before its parity violating beta decay. Parity violation results here in a strongly anisotropic angular distribution of the decay positrons with respect to the muon spin direction. P. Dassonvalle has developed[16] a theory of the hyperfine field, B_{hf}, in such alloys. Muon experiments were done in zero applied field. Contributions to the local magnetic field seen at interstitial sites in ferromagnetic Ni by the μ^+ in this case are now considered. Spin polarized conduction electrons produce a Fermi contact hyperfine field about the μ^+ (see Schenck[17]). The primary contribution may be viewed as a spherical distribution of magnetization centred at the μ^+. It follows that the field at the μ^+, as discussed in the theory section above, is $8\pi M_{eff}/3$, where M_{eff} is the effective magnetization at the μ^+. There is also a contribution due to the magnetization of the sample as a whole. Samples are right cylinders, not spheres, and have macroscopic voids in them because of the way they were made using a plasma furnace to maintain purity. However the magnetization is sufficiently soft in the well-annealed samples that the internal magnetic fields (due to shape and strain anisotropies), in zero applied field, are negligible compared to the hyperfine fields. Accordingly the local field at the muon, $\mathbf{r}_\mu$, may be written,

$$\mathbf{B}_\mu = \mathbf{B}_{hf}(\mathbf{r}_\mu) + \mathbf{B}_{dip}(\mathbf{r}_\mu), \tag{1.12}$$

where the second term may be evaluated as a superposition of dipole field contributions. These contributions are viewed as resulting from moments localized on lattice sites of the FCC

structure. The method employed to evaluate this contribution is due to Lorentz[12]. A sum over dipole contributions is broken into two separate subsums. A discrete sum over moments (which depends on their precise microscopic arrangement) is made over a sphere (assumed small compared to the domain size) centred about the interstitial location of the μ^+. The sum over this sphere is independent of sphere radius providing it is large enough. In zero applied field (no demagnetizing field), the rest of the sample makes a contribution, known as the Lorentz field, $B_L = 4\pi M_s/3$, where M_s is the spontaneous magnetization in the domain. The first subsum is zero for interstitial sites in a FCC structure (this is true for all points having cubic symmetry with respect to the lattice).

Estimating the Lorentz field

In order to extract the hyperfine field, B_{hf}, from the muon spin rotation results it is necessary to correct for the Lorentz field which is ~-3 times the hyperfine field. The magnetization should be determined to better than 0.01% in order to complement the precision of the muon measurements. As muon measurements were carried out in zero applied field, the geometry of the sample is not important. For magnetization measurements, an applied field is necessary and the geometry of the sample can be a severe limitation on the accuracy of the determination of the spontaneous magnetization. Precision techniques have been developed for measuring cylindrical specimens[18]. A further complication arises from the fact that the spatial distribution of sample flux is distorted by the nearby presence of the pole faces of the electromagnet used to apply an external field. One speaks of images of the sample moment in the pole faces, the magnitude of which are proportional to the sample moment and the permeability of the pole faces. The geometry of sample flux distribution and hence the "image" contribution to the measured moment depends on both sample shape and the field history of the pole faces. This situation is handled by making measurements of Ni alloy moment relative to Ni standards of the same size and shape. The presence of voids results in a dependence of measured moment on the orientation of the sample with respect to the field direction. All of the above requires a precise

control of the positions of both Ni alloy sample and its matching standard with respect to the magnetometer (polefaces plus pick-up coils). In order to correct to the temperature of the muon experiments measurements are made at the two temperatures, T = 290.45 K and T_1 = 293.55 K, allowing a linear interpolation of values at T to be made.

The construction and operation of a MSM magnetometry system designed to make the best of this bad situation is described below in chapter 2. In chapter 3 results of room temperature measurements of magnetic moment per gram and its temperature rate of change for the Ni alloys are presented and discussed. The application to the correction of muon data for the Lorentz field with these data are briefly discussed. Finally a comparison between the results of recent local spin density functional calculations (LSPD) and a temperature corrected version of the magnetization data is made.

Chapter 2. Experimental apparatus and procedure

Sample preparation and characterization

The Ni alloys used here were produced by Robert I. Grynszpan, P. Dassonvalle, and Patrick Langlois at CECM Vitry, France[15]. Descriptions of sample preparation and characterization which follow are almost entirely based upon the description given in the thesis of Pascal Dassonvalle[16] as translated and augmented by R. Grynszpan. Inclusion of this, in some cases, incomplete information is justified by its importance for meaningful interpretation of the magnetization data presented in this thesis. Any uncertainties as to sample origin and concentration may be alleviated upon returning the samples to Paris where either a careful look at the previously unavailable records of Pascal Dassonvalle and/or repetition of measurements on these samples can be made.

In order to attempt a theoretical explanation of observed phenomena in dilute binary alloys two questions must be answered; what is the alloy's composition and how are its constituents distributed?

The goal was to produce, high purity, dilute (here being ≤1.25 at. %), binary alloys $Ni_{1-x}T_x$ where T is a transition metal solute that forms a substitutional solid solution of single phase with the Ni solvent. The structure of such an alloy is that of the solvent which in this case is FCC. The theoretical abstraction of a dilute binary alloy is a single solute atom substituting for a solvent atom in a structurally perfect solvent matrix. To approach this in practice care must be taken with sample preparation in order to eliminate all possible inhomogeneities of structure and concentration. Such a solid solution is given the name "terminal" emphasizing that on a temperature-composition diagram it is represented by a vertical line in a single phase field which consists of a continuous series of solid solutions from pure Ni up to the solid solubility limit at the solidus curve. A second phase may result from the precipitation of solute rich inclusions. This situation is highly undesirable as it makes the μSR and magnetization data sample dependent. Such data, given detailed sample knowledge, may be of some interest in itself.

Stoichiometry, size and distribution of such inclusions may be inferred from the results of x-ray, x-ray fluorescence,TEM, and positron annihilation experiments[16].

2.1 Sample preparation

Impurity concentrations, in ppm by weight, determined by neutron activation analysis of the "pure" Ni used as an alloy base are shown below in Table 1[16].

Table 1: *Neutron activation analyses of Ni alloy base material*

Fe	110* (5.5)		Sb	≤	0.07
Cu	2.7* (3)		Mo		0.06 (2)
Al	≤	1	Sr	≤	0.04
Pb	≤	1	Ag	≤	0.03
Zn	≤	0.87	W		0.022 (1)
Zr	≤	0.6	Ba	≤	0.02
Tl	≤	0.5	Sc	≤	0.017
Bi	≤	0.2	Hf	≤	0.01
K	≤	0.2	Ta	≤	0.01
Rb	≤	0.12	Cs	≤	0.005
Na	≤	0.1	Ga	≤	0.002
Co	≤	0.095** (10)	Sc		0.0013 (5)
As	≤	0.08	La	≤	0.001
Cr	≤	0.08	Mn	≤	0.001
Au	≤	0.07			

Total impurities ≤ 120 ppm by weight
** after correction
* apparent percentage
( ) error in last significant figures.

For details of the above analysis (such as corrections (**and*) made for "parasitic" reactions) see Dassonvalle's thesis[16]. Excepting Fe at 110, impurities are in total below 10 ppm by weight.

Added metals

Added metals, having a minimum purity of 99.95% (wt.), add at most 20 ppm of unanalysed impurities to the overall impurity. In all cases added metals were weighed to within 10^{-4} g before and after alloying (to keep track of any deviations from the nominal concentration before alloying). Some samples were subjected to neutron activation analysis at several different locations in the sample. In this way both homogeneity and agreement with the nominal value of concentration were tested. Results of neutron activation analyses as well as indications of precipitation from TEM and μSR experimental results are presented together with other data, obtained here, which serve to characterize the samples, at the end of this section in Table 2.

Alloy preparation

There were two different methods of sample preparation. All but 5 (and possibly 2 more) of the 60 samples were prepared in the following way.

Plasma furnace

After precise weighings a given solute material was placed in a hole drilled in the top of Ni base material. The above was alloyed in a plasma furnace under a H-Ar atmosphere. In the liquid state, the alloy is held in quasi-levitation on the end of a vertically mounted cold Cu finger. The presence of Ar reduces the loss of material due to evaporation onto the walls of the apparatus while H undoubtedly reduces impurities such as C, O, S, etc.. Unfortunately, many macroscopic voids are produced due in part to the presence of H. In an attempt both to remove such voids and improve the chemical homogeneity of such a sample, it was remelted several times under an atmosphere of Ar alone. Contamination by the Cu finger was checked by neutron activation analysis and was found to be negligible.

The typical result of the above was an oblate ellipsoidal shaped alloy, being approximately 10 mm in height, 16 mm in diameter, and 10 g in mass. At this stage grains having columnar or basaltic structure were oriented towards the symmetry axis and had, typically, a volume of from

5 to 0.5 mm^3. It is possible that void diameters may increase from bottom to top and that their distribution would tend to follow the columnar grain structure.

After an electrochemical polish, samples were annealed 4 hrs at 1050°C in a 3 10^{-7} Torr vacuum and then slowly cooled (10 hours to reach ambient temperature). During cooling the furnace current is cut off to avoid producing a remnant magnetization of the sample. The magnetic field produced by the current in the furnace windings defines a preferred direction about which the solute orders itself. Such a process is commonly referred to as magnetic annealing, owing to the production of a remanent magnetization this results in a sample dependent contribution to the internal magnetic field.

Induction furnace

The Ni standards labelled G and H, Pt alloy F, Mn alloy E, and possibly the Mn alloy 12 and Co alloy 7, were prepared as discussed below. There is some uncertainty with regard to the last two because they, unlike the others, are not of the large size expected for this method. However, in the complete list of neutron activation analysis (N.A.) results, for Ni alloy samples as supplied by R. Grynszpan, which includes samples not considered here, the induction furnace method is indicated for two entries which are believed to correspond to these two samples. This belief, in the case of Co alloy 7, is based on the fact that the "as made" concentration, 0.91 at. % (atomic %), which accompanied the samples prepared for magnetization measurements, agrees with N.A. concentration, 0.944 ± 0.028 at. %, of the only unaccounted for, above mentioned entry. In the case of Mn alloy E the "as made" concentration was given as 0.91 at. %. However, there is no entry from R. Grynszpan's table which corresponds to this, the highest being 0.445 at. %. Based on the results of the relative, with respect to Ni, change in magnetization to be described below, Mn alloy E corresponds to an entry, prepared by the induction furnace method, with a N.A. determined concentration of 0.110 ± 0.015 at. %.

Precisely weighed constituents were placed in a high purity fused alumina crucible which had been previously degassed for 12 hours at 1100°C. Further degassing, under either a

10^{-5} Torr vacuum or, for solutes (Cr, Mn, etc.) with vapor pressures greater than that of Ni, 10 Torr of Ar, was done with filled crucible in place in the Balzer induction furnace used for alloying. After several minutes of mixing, the liquid bath was cast in a cold Cu mold. Again, negligible contamination, due to either crucible or mold, was found. While such alloys exhibit good chemical homogeneity, structurally there are cavities and variable grain sizes.

To improve the above situation, remeltings were followed by annealing for 4 hours in either a 2 10^{-6} Torr vacuum or 20 and a 16 hour cooling. The typical result is a cylinder approximately 10 mm high and 45 mm in diameter, having a polycrystalline structure, with grain volumes ranging from 1 cc for pure Ni to 10 mm^3 for a 1 at. % Mn alloy.

Neutron activation has shown W and Cr impurities by 15 and 2 ppm by weight respectively (from the thermal baffles of the Czochralsky puller).

Preparation of samples for magnetization measurements

Signal per gram of an alloy sample is measured relative to that of its matching in size, shape, and metallurgical origins, Ni standard. This is done to ensure that for a sample and its standard, contributions to signal due to, field dependent, magnetic images and demagnetizing fields, scale in the same manner. In this way it is hoped that their signals per gram are more nearly in the same ratio as the desired ratio of their spontaneous magnetizations.

After the μSR measurements were completed the samples were prepared for magnetization measurements as follows. Cylinders were spark cut from the samples along their cylindrical axes. They were subsequently machined to the nominal dimensions (height × dia.) of either 6.5 x 9.5 or 9.5 x 9.5 mm (as possible). Such samples were centreless ground to within ± 0.01 mm in diameter and ± 0.005 mm in height and then lightly chemically polished (to reduce surface roughness and remove the damage layer). Final heat treatment consisted of the same annealing conditions for all samples of 4 hours at 1050°C followed by cooling for 10 hours under a 3 10^{-7} Torr vacuum. For each size a sample of Ni base material of the same dimensions was prepared in the same manner.

2.2 Sample characterization

Below are described measurements, made here for this thesis, which serve to characterize the state of the Ni alloy samples.

Density measured and expected

Samples were carefully weighed to within ± 5 μg using a Mettler Microbalance. Their volumes and hence densities were calculated from careful measurements of height and diameter using a micrometer. Due to a sample's surface roughness and rounded edges these densities are lower than they would otherwise be.

An "expected" variation of density with concentration, for a given alloy series, was taken as a least squares linear fit to published data[19] of the variation of lattice parameter with concentration. Where possible, data for slowly cooled alloys of the lowest concentration were used. In cases, such as Ta and Zr, where no such data was available, the approximation known as Vegard's law was used to obtain an "expected" variation. This approximation takes the average atomic volume of a binary alloy as the linear combination, weighted by concentration, of those of its two pure constituents. Values of lattice constants used were obtained from Mirkin[20]. Note that for Zr, for which the stable phase at room temperature is HCP, the lattice constant of the quenched high temperature BCC phase was used. For Hf, which has a hexagonal structure, no attempt was made to estimate "expected" density variation.

Comparison of measured density, ρ, with expected values for the Ni standards and each alloy series (excepting Hf) is shown, as a relative percentage change, $\Delta\rho/\rho$, in Table 2 below. Errors reflect uncertainties in the measurements of dimensions. This table compares density, calculated from measurements of mass and dimensions, with expected density. The column headed "P" lists indications of precipitation from μSR and TEM data; p and P, respectively. The code is; 1= p or P , 0=no evidence of precipitation, and -1=no neutron activation data available.

Table 2:*Nickel alloy compositions and densities*

Solute	Label	C(at.%)	ρ(g/cc)	Δρ/ρ(%)	P	Mass(g)
Ti	N59	0.147(02)	8.8271(82)	-0.879	+1	4.06692
	N34	0.262(02)	8.8616(83)	-0.437	+1	4.08280
	N35	0.538(11)	8.8252(82)	-0.714	+1	4.06602
	N14	0.910(00)	8.8146(82)	-1.090	-1	4.06113
V	N58	0.150(01)	8.7444(72)	-1.833	+0	4.00765
	N53	0.251(11)	8.8119(99)	-1.045	+0	2.67054
	N32	0.537(13)	8.8593(73)	-0.427	+0	4.07492
	N13	0.923(05)	8.8340(87)	-0.595	+1	3.30205
Cr	N61	0.144(06)	8.8735(57)	-0.400	+0	3.31639
	N33	0.233(30)	8.8622(56)	-0.510	+0	3.31596
	N21	0.545(05)	8.8760(50)	-0.293	+1	4.08702
	N24	0.886(24)	8.8226(66)	-0.825	+1	2.68878
Mn	N12	0.110(15)	8.8750(50)	-0.358	+0	4.08898
	NIE	0.750(00)	8.8663(40)	-0.509	-1	5.80469
Fe	N45	0.252(07)	8.8143(56)	-1.033	+0	3.29955
	N54	0.542(07)	8.7999(49)	-1.125	+0	4.05087
	N11	0.922(03)	8.8609(66)	-0.349	+0	2.69786
Co	N27	0.241(17)	8.8612(50)	-0.559	+0	4.06780
	N06	0.526(23)	8.8530(63)	-0.641	+0	2.08443
	N52	0.777(23)	8.8439(56)	-0.735	+0	3.30153
	N07	0.944(28)	8.8053(63)	-1.163	+0	2.07048
	N08	1.198(14)	8.8811(50)	-0.304	+0	4.08706
	N10	1.517(13)	8.8744(50)	-0.367	+0	4.07648
Cu	N01	0.262(05)	8.8807(50)	-0.354	+0	4.07917
	N02	0.559(22)	8.8833(50)	-0.332	+0	4.09251
	N51	0.910(00)	8.8249(49)	-0.994	+0	4.07535
	N03	0.957(44)	8.8732(64)	-0.454	+0	2.08697
	N04	1.220(14)	8.8593(51)	-0.616	+0	3.05362
	N05	1.532(03)	8.8588(66)	-0.629	+0	2.70245
Zr	N37	0.256(04)	8.8481(49)	-0.561	+1	4.07658
	N38	0.547(03)	8.7981(51)	-0.949	+1	3.03815
	N29	0.888(01)	8.8253(49)	-0.437	+1	4.06698
Nb	N43	0.252(07)	8.8509(50)	-0.700	+0	4.06609
	N56	0.573(06)	8.8696(50)	-0.513	+0	4.08969
	N25	0.906(02)	8.8700(50)	-0.532	+1	4.09410
Mo	N41	0.245(14)	8.8576(50)	-0.709	+0	4.07856
	N42	0.550(01)	8.8537(47)	-0.879	+0	3.31747
	N18	0.905(05)	8.8931(64)	-0.584	+1	2.08524

Table 2 (continued)

Solute	Label	C(at.%)	ρ(g/cc)	Δρ/ρ(%)	P	Mass(g)
	N50	0.257(04)	8.8815(50)	-0.426	+0	4.09581
Pd	N57	0.549(01)	8.8682(56)	-0.675	+0	3.32424
	N26	0.909(03)	8.7911(51)	-1.659	+0	3.03162
Hf	N60	0.262(01)	8.8402(49)	-	+1	4.07293
	N39	0.259(02)	8.8101(56)	-1.504	+0	3.30097
Ta	N40	0.548(04)	8.9275(50)	-0.600	+0	4.10951
	N28	0.901(01)	8.9773(52)	0.543	+0	3.08701
	N55	0.252(08)	8.9168(50)	-0.385	+0	4.10858
W	N49	0.543(07)	8.9758(52)	-0.234	+0	3.08498
	N20	0.912(01)	9.0135(50)	-0.455	+0	4.15278
Pt	NIF	0.750(00)	9.0126(41)	+1.132	+0	5.90607
	N17	0.902(02)	9.0362(51)	-0.263	+0	4.16326
	N30	0.257(02)	8.9162(50)	-0.392	+0	4.10057
Au	N16	0.541(03)	8.9530(50)	-0.469	+0	4.12320
	N15	0.913(01)	9.0191(50)	-0.369	+0	4.15735

With regard to the alloy series two features should be noted. Firstly, measured densities are typically speaking, ~ 1/2 % lower than expected. This is certainly due to in part to the overestimation of the volume. It may also indicate an average background volume of voids for this method of production. Secondly, in many cases measured densities are much more than 1/2 % below expected values. These anomalous values strongly suggest two possibilities; firstly that these samples contain a proportionately larger volume of voids and secondly that compositions are inaccurately known. As discussed below in the section entitled "voids", an asymmetric distribution of voids may lead to large variations of signal upon 2π rotation of samples about their symmetry axes, as well as an overall reduction in sample moment. In these cases the amplitude and form of the variations were compared with those of the more well behaved samples. No clear cut difference between these two groups was noticed. Also, correlations between variations with composition of measured densities and relative change in magnetization were not found to be conclusive.

Density of standards

The lattice parameter and corresponding density for Ni were taken to be 3.5238 Å[20] and 8.91172 g/cc[19] respectively. The measured densities for the 5 standards used are,

Table 3:*Densities of Nickel standards*

Label	ρ(g/cc)	Δρ/ρ (%)
NIA	8.8532(66)	-0.7
NIB	8.6092(50)	-3.4
NIC	8.7962(57)	-1.3
NID	8.6565(48)	-2.9
NIG	8.8908(40)	-0.2.

Standards NIB and NID show the largest discrepancies. Although NIB is the least dense it shows a smaller variation of integrated signal upon rotation about its symmetry axis than does NID. This may simply reflect a more asymmetric distribution of voids in the latter case. Note that the NIG standard whose measured density is closest to expected is the only one which was prepared with the induction furnace method.

Visual inspection

In general terms samples have a "shiny" metallic finish and, particularly visible on the end faces, machining marks from turning on a lathe. Particular features of note are of three kinds;

1/ voids visible (to the naked eye) at the surface as pits,

2/ the appearance, particularly visible on the end faces, of interference colours which are different for the different grains made visible by them,

3/ dull patches, characterized by diffuse scattering and greater surface roughness.

Surface voids are found on 20 of the samples, ranging in size from ~1/8 mm to ~2/3 mm. The largest sizes (in mm), for the samples (element (sample no.)) Fe(45),Ni(D),V(32), and

W(49) are 2/3,1/2,1/2, and 1/3 respectively. A surface void, being asymmetrically placed, might be expected to lead to large variations of signal upon 2π rotation of the sample. However, the form and amplitude of this variation for samples in the group above and for samples without noticeable sample voids do not differ significantly.

Interference colours are thought to be due to a thin layer of oxide of the solute element since they occur only for the highest (except in the case of Zr for which all the samples show colours and there is clear evidence of precipitation) concentration alloys in series. Presumably the thickness of the layer and hence its colour depend on the orientation of the surface which varies from grain to grain. These colours are observed for the following samples (solute, (as made concentration),sample no.);Ti(.91)14, Ti(.55)35, V(.91)13, Mo(.91)18, Nb(.91)25, Mn(.75)E, Zr(.26)37, and Hf(.26)60. Note that after mechanically polishing the Ti samples the colours were no longer visible.

Dull patches occur on the following samples; Zr(.55)38, Zr(.91)29, Ta(.91)28, Nb(.26)43,Co(.59)6, Co(.91)52, Cu(.26)1, and Cu(.91)51. Relative to the Zr samples the rest have small patches which could be described as minor discolourations. For Zr(.55)38 and particularly for Zr(.91)29 for which there is only a narrow metallic band about the waist, the dull patches have a greater surface roughness which strongly suggests that they are not of single phase.

SAM (Scanning Auger Microprobe) analysis of Ti alloy series

A Perkin Elmer model 595 SAM was used to determine the surface composition before and after Ar^+ ion sputtering. The ratio of Ti concentrations before and after sputtering were found to be from ~2 to 4. After sputtering, compositions for all but the .15 at. % sample (for which the signal to noise ratio was ~2) agree with as made and N.A. results within uncertainties. In summary, the Ti concentration decreases with depth near the surface (sputtering depth).

X-ray Fluorescence of Ti and V alloy series

A Cameca model SX-50 electron microprobe system was used to determine the composition, over an endface of Ti and V alloy series samples. This fully automated system combines a scanning electron microscope with four independent wavelength dispersive spectrometers of the Rowland circle type for the analysis of x-ray fluorescence. Samples were shrink fit into the centre of cylindrical delrin mounts 1" in diameter and ~ 3/4" high, one endface of the sample being flush with the delrin mount endface. Samples in their delrin mounts were mechanically polished by hand, using diamond paste and a short nap cloth pad, in order to provide microprobe access, without the need for refocusing, to as smooth a surface as possible (signal is a function of surface topography). In some cases a final polish was made with a solution consisting of a colloidal suspension of 70 nm silica particles in a basic solution commonly used for polishing Si wafers (Rodel Products, Scottsdale Arizona). This method combines mechanical with chemical polishing and results in a very smooth (relative to diamond polish method) surface having visible evidence of grain structure due to preferential etching of grains. Sample charging was prevented by evaporating a thin carbon film over the (sample/delrin sample mount) surface. Two of the spectrometers were employed in parallel, one calibrated against the Ni standard H and the other against a pure rutile (TiO) or Vanadium standard. Measurements of Ti and Ni fluorescence signals were made at 100 points in an irregular pattern over the whole of the polished sample endface. After each 10 measurements, the probe was returned to the same position on the sample and a measurement taken, in order to determine machine reproducibility. The standard deviation, σ, of these 10 measurements represents, in all cases, reproducibility to less than one part per thousand ($\sigma/\sqrt{10}$) for 100 such measurements. Averages(standard deviations) of concentrations in atomic percent, preceded by sample numbers, are shown below.

Table 4: *X-ray flourescence compositions of dilute Ti and V alloys with Nickel*

Titanium	XRF	N.A.	Vanadium	XRF	N.A.
59	0.151(0.011)	0.147(0.001)	58	0.156(0.003)	0.150(0.000)
34	0.285(0.034)	0.262(0.002)	53	0.317(0.004)	0.251(0.011)
35	0.594(0.061)	0.538(0.011)	32	0.822(0.006)	0.537(0.013)
14	0.963(0.060)	0.910(0.000)	13	0.910(0.007)	0.923(0.005)

Note that Ti sample heterogeneity, as indicated by standard deviations (~10 %), is ~10 times that of V. For Ti these values are higher than but within $\pm\sigma$ of as made and N.A. results. For V however, sample 58 and particularly samples 32 and 53 are more highly concentrated than N.A. indicates, not agreeing within $\pm 10\sigma$ in the latter two cases.

The measurements described above sample to a depth ~ 1μm, while N.A. is by comparison a bulk measurement. In this sense the XRF results may be concluded to indicate chiefly Ti and V sample heterogeneity of composition "near" the surface. How closely these numbers reflect the bulk is answered in part by the SAM results above for Ti since sputtering depths used were small compared to 1μm. However the large discrepancy noted for V sample 32 above is curious, especially considering the magnetization data to be presented below in chapter 3 for this series.

2.3 Experimental layout

The moving sample magnetometry system described here has evolved from the original constructed by C. Winter[21]. A block diagram of the entire system is shown in fig. 2.1. Almost all functions are under direct computer control (exceptions are the six temperature controllers, which are self contained and sample changes, which must be made manually). The North Star Horizon computer was programmed in the interpretive Microsoft BASIC 80 language. Arrows indicate whether a signal is data input or a control output. The system may be broken down into four main parts; field control and measurement, control and measurement of sample temperature, sample motion and finally, conditioning of the induced signal. For emphasis, the primary signal path is shown in bold. Details are found below of how measures of field, temperature, and integrated signal are obtained.

Magnitude of the applied field, as measured by a NMR magnetometer, is collected in a BCD (binary coded decimal) form by the computer via one of its parallel input/output boards. There are three relays through which signals may be selected by the computer (termed SCANNER in fig. 2.1) for measurement by a FLUKE 8842A digital ("5 1/2" digits) voltmeter and subsequently read by the computer via an IEEE 488 bus. To facilitate field (F) setting a measure of the applied field, as given by the output of a Hall probe type gaussmeter, is selected by the computer for measurement by the digital voltmeter via a reed relay. The integrated signal is selected by one of two Crydom PVR3301 photovoltaic relays. Drift and noise performance of these relays were found to be far superior to garden variety reed relays. The other "PVR" selects a measure of the sample temperature, in the form of a conditioned version of a Cu-constantan thermocouple voltage.

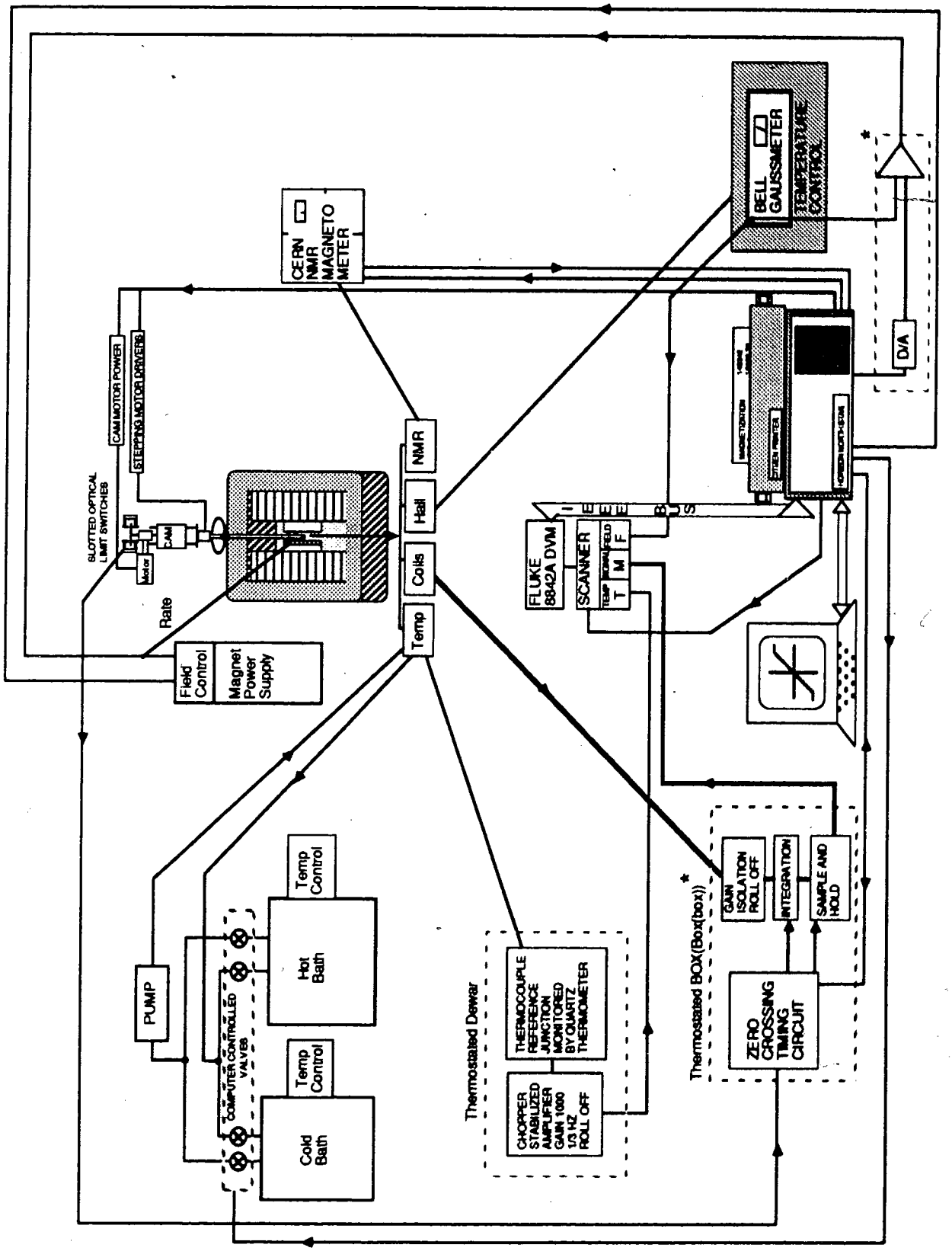

Fig. 2.1 Block diagram of the entire MSM system.

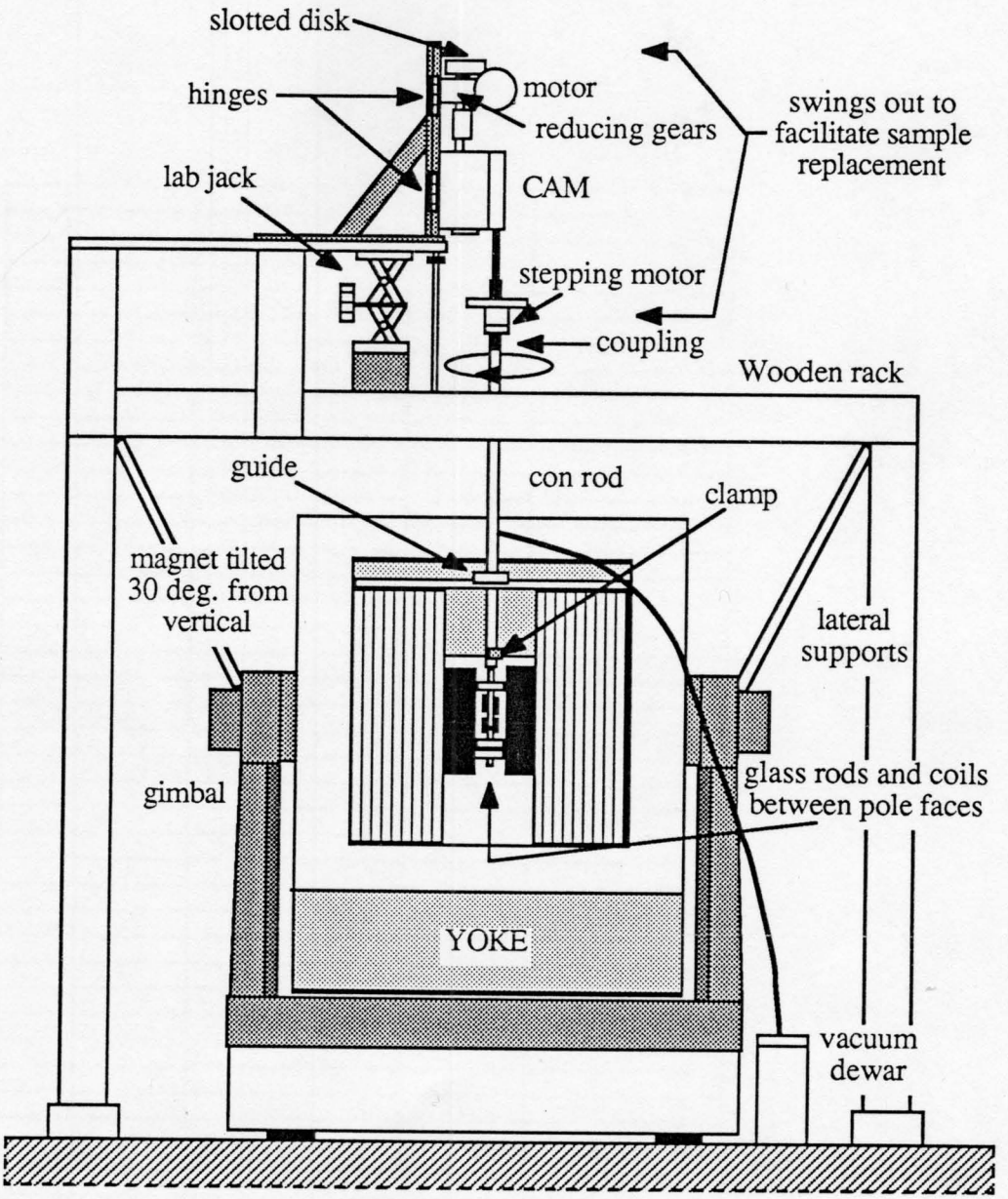

Fig. 2.2 Layout (1:17 scale)

Fig. 2.3 ELECTROMAGNET:cross section

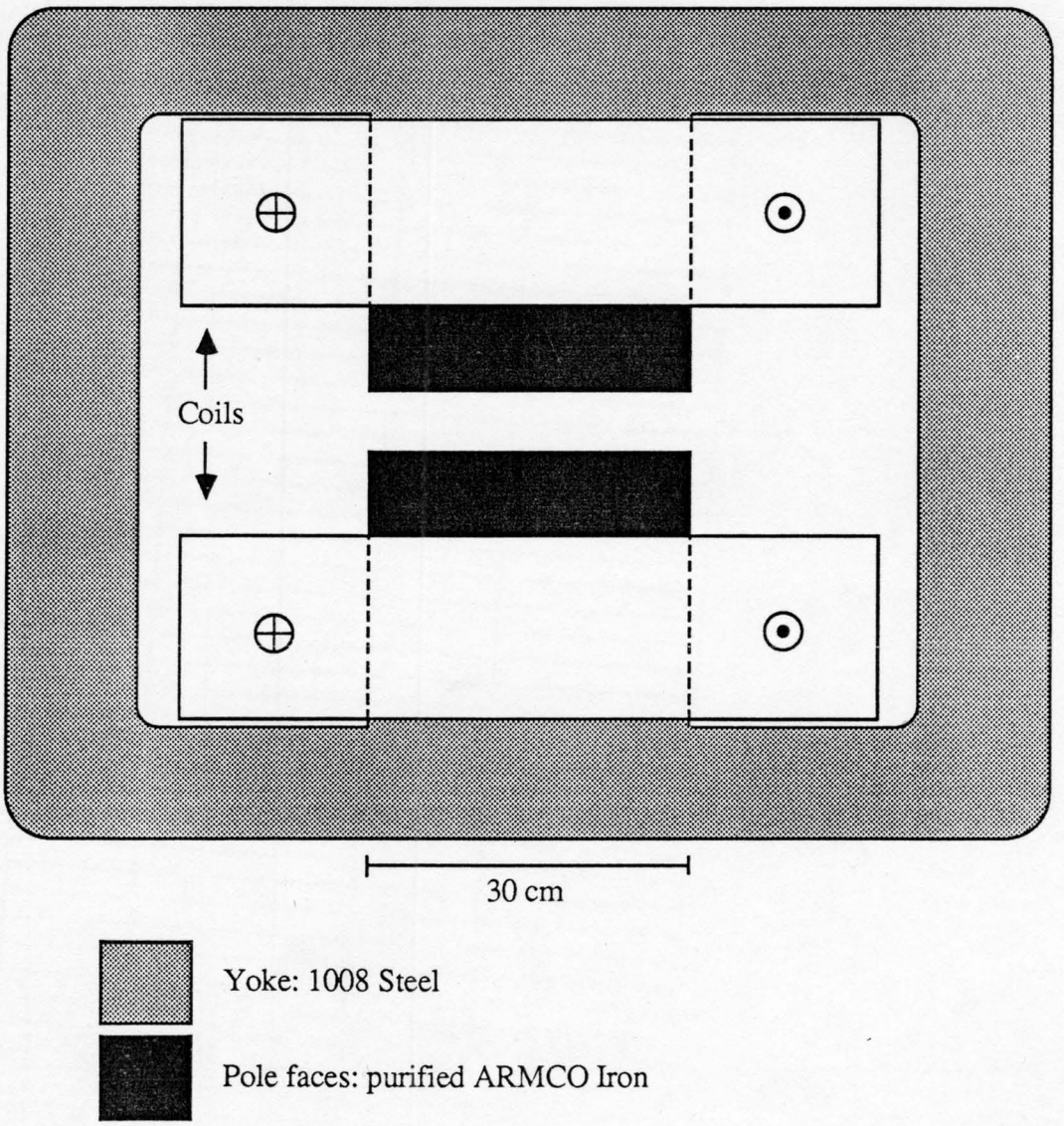

Field control and measurement

Field control

An external magnetic field was applied to samples via a tap water cooled, low voltage, MAGNION type L-128 electromagnet (see fig. 2.2) which has a 2.25" air gap between right cylindrical, 12" diameter, ARMCO #120-225-471 iron pole pieces, powered by a MAGNION/HARVEY-WELLS HSR-1365B 3 phase 220V supply. A cross section of the magnet is shown in fig. 2.3. A custom board in the microcomputer allows control of field functions such as: ON,OFF,FORWARD, and REVERSE field, by means of relays in the MAGNION FCC-4 field regulator. Fields of up to 13 kG were set and stabilized by the integration of the sum of two external error voltages by the field regulator. The first error voltage, applied to the control input of the field regulator, is proportional to the difference between a computer generated field set voltage and the analog output of a BELL model 660 digital gaussmeter with a BELL model HTJ6-0608 S Hall probe (serial no. 101248) placed ~3 1/2" off the center of and midway between the pole faces (see fig. 2.4). The Hall probe is located from the coil mount a distance sufficient to avoid excessive variation of applied field due to sample motion. A coil wrapped around the end of one pole face, known as the rate coil, generates the second error voltage which supplies differential feedback to the field regulator.

Long term stability of field settings is improved by thermostating some of the key components. The gaussmeter, along with a fan, resistive heater, and thermistor is contained in a box whose temperature is maintained to within ±0.2 K by a proportional controller (see right hand side of fig. 2.1). The D/A converter that generates the field set voltage and the comparator which provides an error voltage to the control input of the field regulator are both inside a large box with 1/2" thick aluminium (Al) walls.

Thermostated chamber

This Al box is within a temperature controlled chamber (see BOX(Box(box)) lower left hand side of fig. 2.1) which itself is part of a system that maintains temperature control of critical, signal related electronics. These electronics, which are responsible for the amplification with roll off, integration, and subsequent sample and hold of the raw signal from the pick-up coils, will be discussed below in some detail. Including the room, this system comprises three separately thermostated chambers. The innermost, a 1x1x2 ft. box with 1/16" thick copper walls, along with the aluminium box mentioned above, is contained within a ~2x2x2 ft. box of 1" thick styrofoam construction. Proceeding inwards from the room, each chamber achieves a successively higher and finer control of temperature. Such a layered design relies on the fact that the degree to which a chamber's temperature can be controlled is limited by the influence of its surroundings to which there is a net heat flux. Room temperature, depending on the time of year, is controlled to within from ±1 K to ±5 K over a 24 hr. period. A muffin fan draws room air into the styrofoam chamber on demand from a thermistor located near a second, inner fan, which provides circulation. Under normal operation the muffin fan is never at rest, due to low friction and its angular momentum, thus producing a continuous displacement of the warmer air out through holes in the styrofoam walls. The net effect of this, is to provide a temperature controlled (to within ±0.2 K) heat sink for the innermost copper box. Inside the copper box, an on-off controller supplies power to a nichrome heater, strapped to the front of a circulation fan, on demand from a thermistor located just downwind. While the controller in the styrofoam box is in operation the temperature in the copper box is held to within ±0.02 K of what is typically 303 K.

Field measurement

Magnetic field measurements were made with a CERN-EP type 9298 NMR magnetometer. For details of its design and operation see K. Borer and G. Fremont[22]. The NMR technique

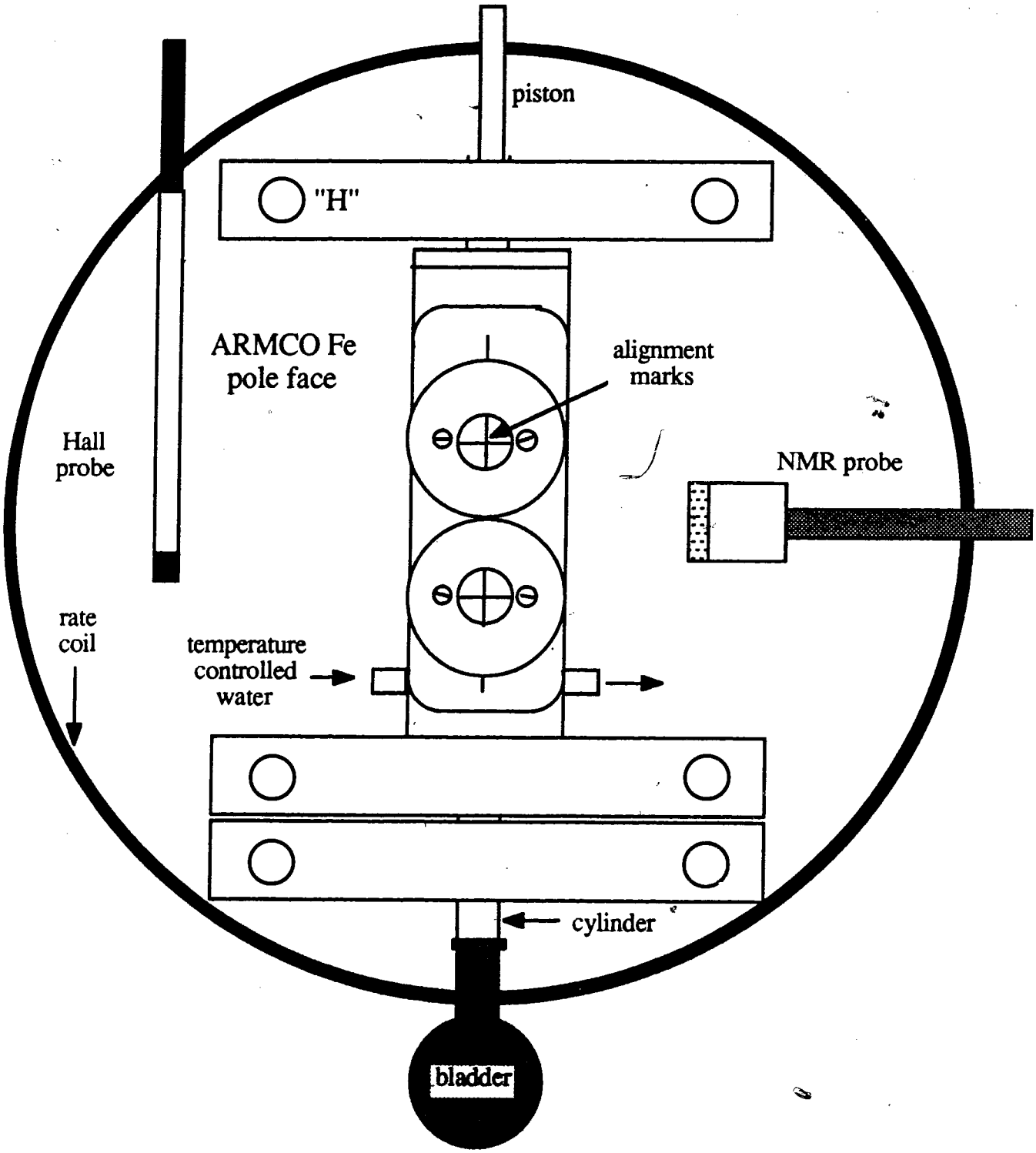

Fig. 2.4 Field's eye view.

used here relies upon the linear proportionality constant between the magnitude of a static magnetic field H and the corresponding frequency of RF induced precession of proton spins about this field being known with high precision (4257.608(12)Hz/G in a cylindrical sample of water). The extent to which this is true is demonstrated by the fact that NMR is used as a primary magnetic field standard. The entire system comprises a NMR probe, probe amplifier box, and a double width NIM plug in. Five separate 0.1M $NiSO_4$ aqueous probes, with overlapping ranges, allow field measurements to be made from 1 to 21 kG. Since measurements of field are made when the sample is at rest the NMR probe is located (see fig. 2.4) closer to it than the Hall probe may be. For a given field range (probe) computer controlled measurements can be made. Coarse adjustments corresponding to a given field setting can be made by applying a computer generated voltage to the V_{in} input on the rear panel of the NIM plug in. Fine adjustments are made, over an adjustable preset range, by the automatic NMR signal search and lock capability of the device itself. A BCD output of the 7 digit display of field in gauss (to a 0.01G resolution), strobed at 4 Hz, is read by the computer.

Field uniformity (as measured with nothing between the pole faces except a Hall probe), is indicated by the change in the field from its 12 kG value at the symmetric midpoint between the pole faces. In the radial direction the field changes in an approximately parabolic fashion, falling by ~1/2 G (or 1 part in 24000) 2" from the centre. Along the symmetry axis there is a similar smooth drop. A decrease of ~0.06 G (or 1 part in 200000) is seen 5/8" from the centre. This value would correspond (half way through the samples motion) to an axial variation over the volume occupied by a sample of 2 ppm. The corresponding field variation between the middle and an end of the 2" sample stroke is approximately 10 ppm.

Dynamic effects due to pole faces

The existence of a number of dynamic effects were inferred from the time evolution of induced and integrated signals. In all cases observations are attributed to the magnetic state of the cylindrical Fe pole faces of the electromagnet used.

Eddy currents

After the field was changed, there was a 90 second delay before a measurement was taken. This was done in order to avoid complications related to time effects. For example, due to eddy currents, a change in the electromagnet current changes the magnetic state of the pole faces from the outside in. The time constant for this was found to be of the order of seconds.

Note that, as shown by Winter[21], the coils must be located symmetrically with respect to the pole faces in order to avoid a contribution to the induced signal of a voltage proportional to the 2nd derivative of the magnet current. This voltage is due to eddy currents in the soft Fe pole faces of the electromagnet.

Field overshoot

As more care was taken with the measurement the resolution and reproducibility of the measurements improved. Nonetheless this diligence failed to remove an unexplainable feature of the measurements; signals made for two fields of opposite direction differed by an amount greater than could be attributed to the difference of their magnitudes. That is, greater than the signal change expected from the field dependence of the signal at this field. The relative size of the difference was seen to decrease when smaller field steps were taken. The mystery remained until the magnet power supply cooperated by losing its ability to set fields using the "sweep" mode. Now forced to use the "regulate" mode, the asymmetry of forward and reverse signals was seen to increase.

Field control damping differs for these modes; underdamped for regulate and more nearly critically damped for sweep. This resulted, for a field set from 0 to 12 kG, in the appearance of an up to ~2% field overshoot where little or none existed before. Percentage overshoot is independent of the size of the field change, so that small overshoots accompany small field changes. Originally the field sets in the forward and reverse directions were unequal. With the addition of overshoot this difference increased.

As discussed above, there is an "image" contribution to the signal whose maghitude is proportional to the permeability of the pole faces. Permeability and hence the signal depend on what minor loop the pole face is on. Loop identity is defined by the maximum field attained. The larger this field, the less the permeability (see "Theory" above) and hence signal as the pole faces approach technical saturation. Such behaviour was confirmed by programming successively larger field overshoots. With increasing overshoot the signal decreased, at first rapidly, then more slowly, apparently towards a limiting value.

The situation was much improved by adjusting the field sets so magnitudes were the same in either direction. Further improvement may possibly be achieved by either making large field changes in smaller steps or repairing the sweep mode of the magnet power supply. It is assumed that field set behaviour is sufficiently symmetric and reproducible that such effects may be ignored.

Magnetic aftereffect

After the 90 second delay made before measurement, even though changes in the applied field were too small to account for it, the measured signal was seen to decrease with time in an exponential fashion. The magnitude of this effect was found to be largest for the lowest field used; 8 kG. The magnitude of this change was such that it was necessary to discard the first of 20 measurements taken at this field. This first measurement was typically 3 to 4 times the amplitude of the variation seen upon rotation of the sample; up to 5 parts in 10000.

By far the most likely explanation for this observation is that, due to C and N interstitial impurities, there was a magnetic aftereffect occurring in the Fe pole faces of the electromagnet. Such an effect would result in a relaxation of pole permeability. This effect results from the fact that, given time, these mobile impurities inhabit sites of preferred energy which depend on the local orientation of the magnetization. When a domain wall has been stationary for a length of time long compared to the time required to obtain a sufficient degree of preferred orientation, any subsequent change of the field will require that the wall "escape" from this stabilized state.

Consider the typical situation of a length of domain wall pinned at its ends by two impurity sites. Upon increasing the field, the initial shape of the wall is similar to that of a length of chain draped over the lip of a bathtub, with a pronounced bulge near the midpoint of that wall (or chain). This protrusion, before it is stabilized by interstitials, responds more readily to a driving field. Consequently, immediately after a field change (that follows a sufficiently long period for which there was no field change), the permeability will decrease with time in a fashion related to the diffusion of the thermally driven, "barrier jumping" interstitials. The magnitude of this decrease, for a given field change, is proportional to the volume of domains at the new field and the concentration of interstitials. The larger volume of domains at lower fields explains why the magnitude of the change is largest there. Verbal communication[24] with an individual involved in electromagnet manufacture suggests that their carbon content is from 30 to 50 ppm. For such a concentration at room temperature the time scale observed is reasonable[23].

Sample translation

The part of the apparatus concerned with sample translation and positioning is now described. One of the two (one for each of two sample diameters (nominally 9.5 and 8 mm,)) delrin Ni alloy sample mounts used, is shown in fig. 2.5. The two differ only by the diameter "A" of the hole which accepts the sample. Samples were held in place by virtue of the fact that A's are slightly smaller than sample diameters ("shrink" fit). Gripping the mounted sample with the hand warms and expands the mount allowing easy sample replacement. The sample is pushed to the bottom of the mount where it makes good thermal contact with the thermal grease coated Al "tophat" (see fig. 2.5). This tophat is used as the anchor point for the junction of a Cu constantan thermocouple. The mounted sample is pushed over the end of the "piston", care being taken to thread the junction into a hole drilled in the tophat. Again an undersized hole provides a "snug" fit, which keeps sample plus mount in place, and "hand warming" is used to facilitate removal (note that removal without warming may result in cold flow of the delrin and loss of fit). The "piston" shown in fig. 2.6, is a pyrex tube, 8 mm O.D. and 5 mm I.D., which

Fig. 2.5 CROSS SECTION OF SAMPLE MOUNT (■ Mat.:Delrin)

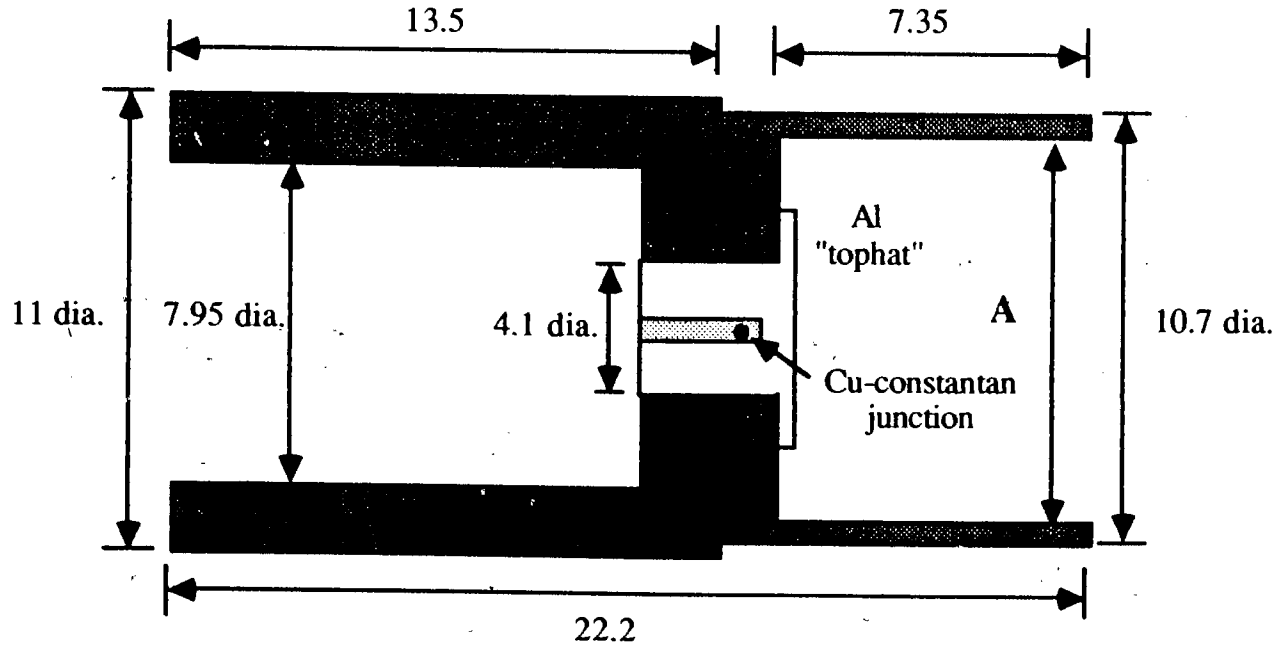

Dimensions are in mm.

A is either 9.5 or 8 mm in diameter.

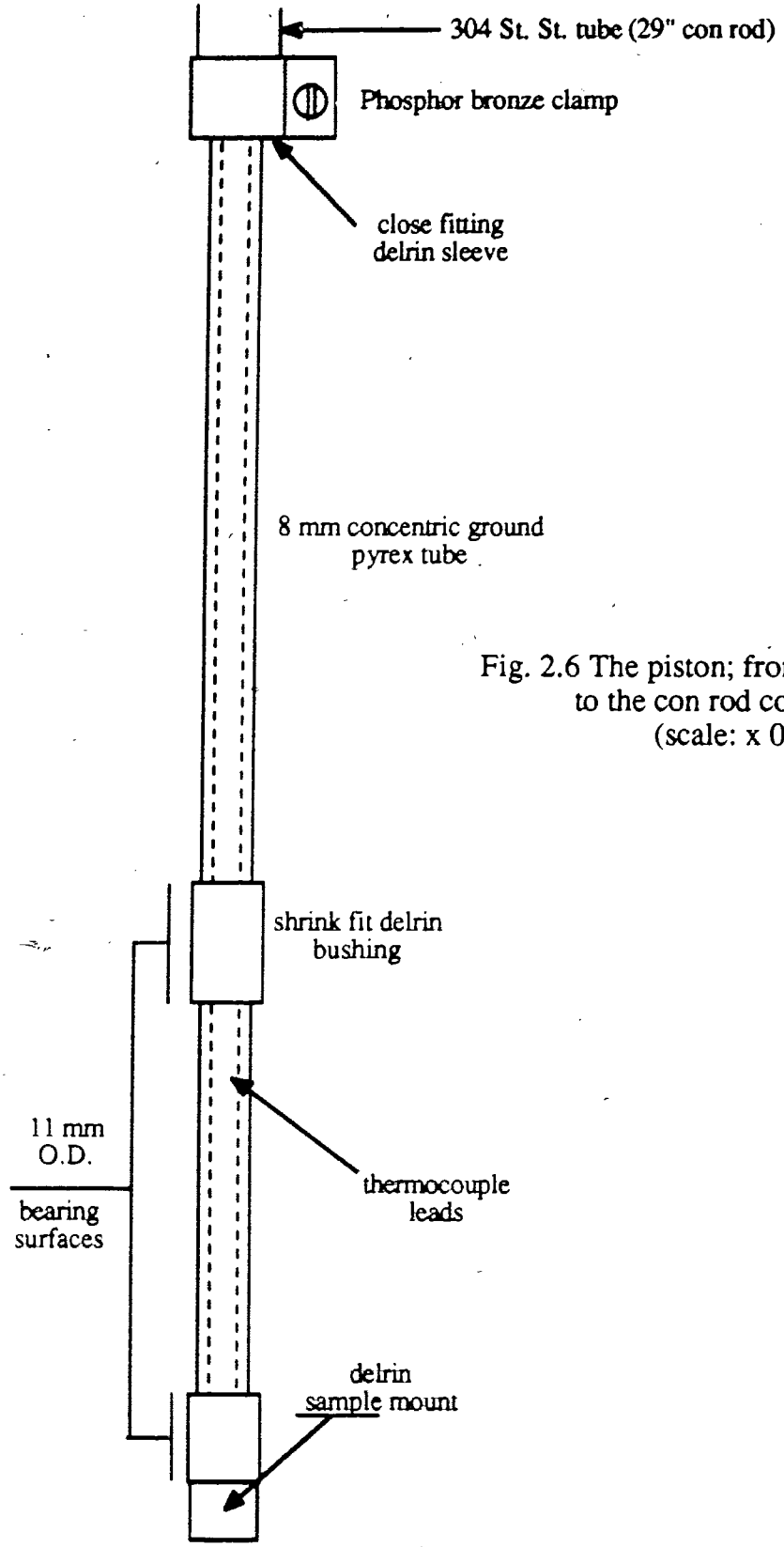

Fig. 2.6 The piston; from sample mount to the con rod connection. (scale: x 0.9)

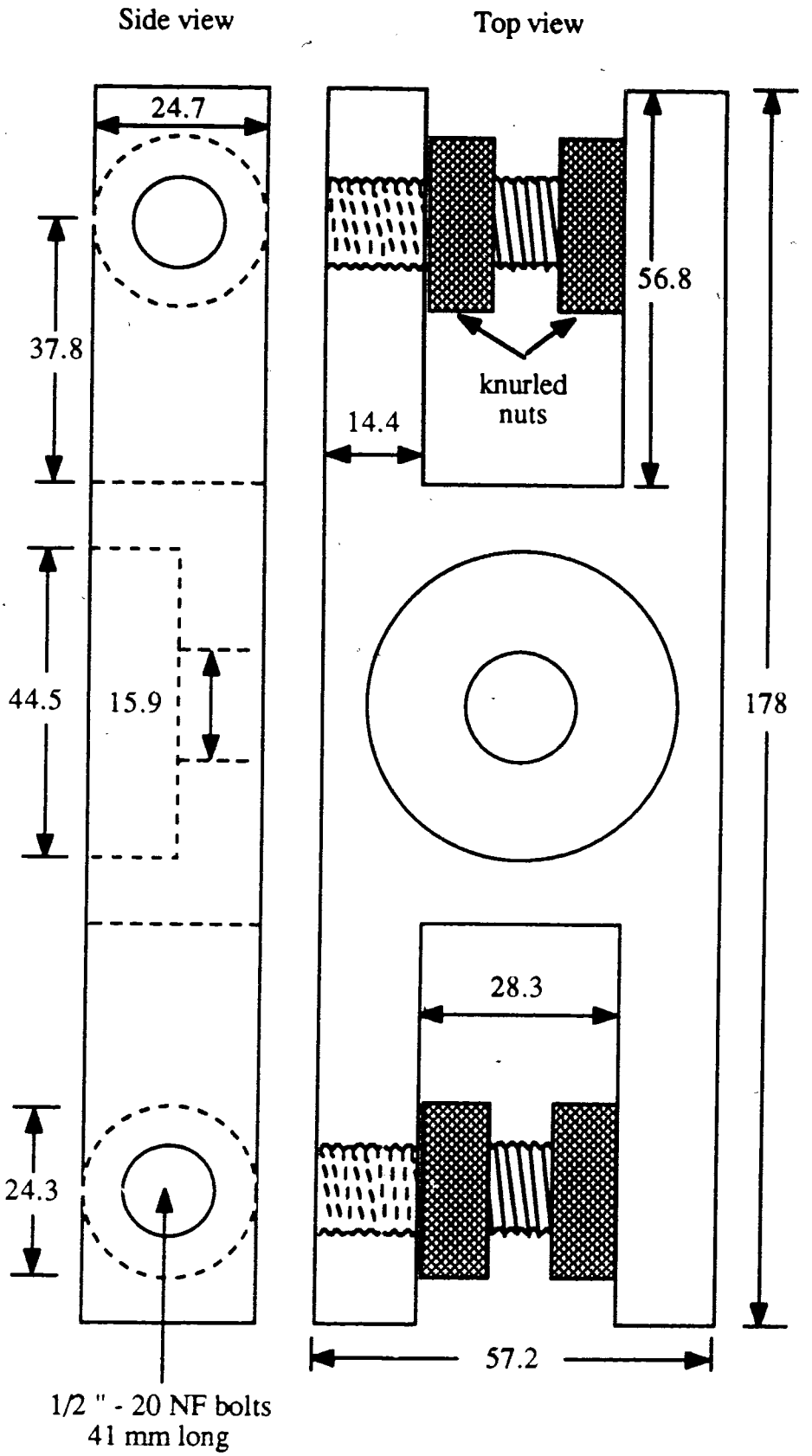

Fig. 2.7 H - shaped plexiglas wedge (all dimensions are in mm)

was "concentric ground" by the Wilmad glass company. A polished pyrex tube, 14 mm O.D. and 11 mm I.D., also "concentric ground" by the Wilmad glass company, serves as a cylinder. This tube is held fixed between the pole faces of the electromagnet by means of the outer two of the three plexiglas H shaped wedges, side views of which can be seen in fig. 2.4. The cylinder is clamped in place by means of two nylon bolts with locknuts. To avoid cracking the cylinder, small pieces of rubber cork are placed between bolts and tube. The cylinder passes through without touching the Al coil mount which is independently supported from below by the third H. A detailed drawing of this third H is shown in fig 2.7. The outer two H's are identical to each other and differ from the third H only by the size of hole drilled through their centre's. H's are slid into position and wedged in place by turning the knurled nuts. In order to maintain symmetric positioning of coils and the sample's motion between the pole faces, holes in the H's are centred and normal to the milled sides that wedge against those faces.

Alignment of the cylinder with respect to coil mount is assisted by the use of a brass rod, machined for this purpose to have a sliding fit through the outer two H's. The procedure used for final positioning is as follows. The upper H, placed in the position shown in fig. 2.4, is aligned with the axis of piston motion and wedged in place. With the knurled nuts only finger tight, fine adjustments of the lower H are made until the brass rod slides freely through both H's. When the pyrex cylinder slides freely through the H's the lower H is tightly wedged into place. The third H with coil mount is then slid into place between the outer two and its nuts are finger tightened. With the cylinder in place, final adjustments are made by observing the gaps between coil mount and cylinder with a mirror, and the H is wedged tightly in place.

Bearing surfaces of the piston motion are the piston end of the delrin sample mount and the close fitting, 3/4" long delrin sleeve located approximately 2 1/2 " above it on the piston (see fig. 2.6). Delrin is an acetyl based polymer which, besides being easy to machine, has the advantages of a relatively (to other polymers) low coefficient of static friction ("self-lubricating") and not being hygroscopic. Care had to be taken, due to delrin's large thermal expansion relative to glass, when machining mount and sleeve for a close fit to the cylinder. After machining, a dial

gauge indicated a "wobble" of less than 10 μm at the sample mount, as the piston was rotated in the cylinder.

A 2" vertical stroke is produced by the motor driven CAM shown in fig. 2.1. The CAM has a rotating cylindrical drum with a groove running about its circumference. Two half inch rods move up and down together through linear bearings as a centrally located ball bearing wheel attached to them rides along the groove. The groove pattern consists of two 120 deg. horizontal sections separated by two 60 deg. linear ramps. This should result in a motionless (for 1/3 of a cycle) sample between up and down strokes. However, the CAM mount is not rigid, and friction produces a back reaction to the stroke which makes the sample bounce up and down momentarily after a stroke. After this dies away, endpoints of CAM motion are found (using a dial gauge and a lever arm) to be reproducible to ~5 μm. Mounted on the end of the two CAM rods is a 12 VDC stepping motor which allows sample rotation with respect to the field. Connecting the stepping motor to piston is a thin walled 304 (low magnetic susceptibility) stainless steel tube ("con rod" in fig. 2.1), 5/8" O.D., and ~29" in length. Alignment of piston with respect to cylinder is improved by the presence of an adjustable teflon guide for the con rod, mounted on an Al plate fixed to the top of the electromagnet's coils. Piston is attached to con rod by means of a snug fitting delrin sleeve pinned into the lower end of the con rod. Slippage of the glass piston relative to the con rod is prevented by use of a phosphor bronze clamp. A 1" vertical cut in the end of the thin walled tube allows a cinching action.

Vertical positioning of the sample with respect to the coils is made in two ways. Coarse adjustments are made by sliding the piston through the delrin sleeve in the end of the con rod (again, to prevent cold flowing, delrin should be warmed by hand). Fine tuning of sample position is allowed by the adjustment of the height of the driving mechanism with the lab jack shown in fig. 2.2. The entire driving mechanism is mounted on a vertically hinged Al plate to provide the necessary clearance for sample replacement. To replace a sample, first disconnect the con rod from the shaft of the stepping motor. Then swing the driving mechanism out of the way

and lift the con rod until the piston's lower end clears the teflon guide. Now piston plus con rod may be pulled down and forward, free of the apparatus.

Timing of sample motion

As shown in fig. 2.2, a horizontally mounted a.c. synchronous motor drives the vertically mounted CAM through a reducing gear. Sample position is inferred from the orientation of the CAM. The latter is indicated by signals obtained when one of two slots, 180 deg. apart on the edge of a circular disk which is attached to the upper end of the CAM drive shaft, pass through one of two fixed optical slotted limit switches mounted directly across from one another (see top of fig. 2.1). Motion of the two slots, corresponding to CAM orientations one half of the way along the upper and lower horizontal sections of the groove in the drum, result in two pulses indicating that the sample is at the top or bottom of its stroke respectively (and will remain there for another 1/6 of a cycle). Referring to fig. 2.8; the leading edge of the pulse selected by the computer, results on the next zero crossing of ~60 Hz line frequency in the following: the IN(0) = 32 input of the computer changes state for 64 cycles (counted by the binary ripple counter, 4040) of line frequency. Normally the ends of this fixed duration pulse correspond to the beginning and ending of the integration of the signal induced in the pickup coils (the computer, between leading and trailing edges, grounding its normally high OUT 0,128 and OUT 0,64 outputs). However, in order to wait for eddy currents to die away, an integration period between the 64 and 128 zero crossings of line frequency available with the circuit shown in fig. 2.8. was desired. Such a variable integration period was obtained by using an adjustable software delay to extend the 64 cycle period.

The timing of the integration of a signal produced by a downward sample stroke is shown in fig. 2.9. Integrations (on either up or down strokes) were performed "on the fly", that is integration occurred on the second of three consecutive strokes. There are two reasons for this. First of all, where the CAM and hence sample comes to rest when the motor is turned off is unpredictable, resulting in a variable location of the stroke with respect to the integration

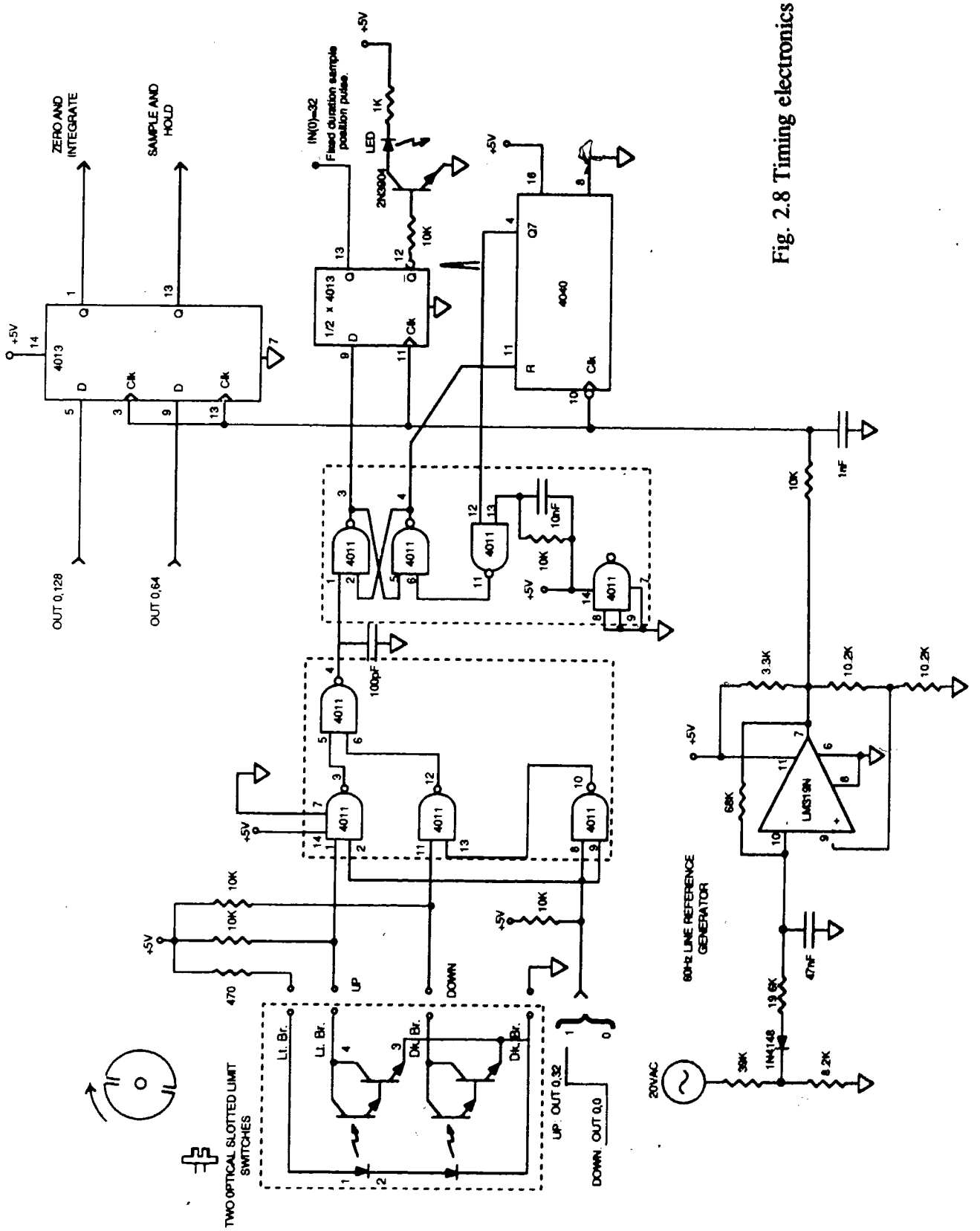

Fig. 2.8 Timing electronics

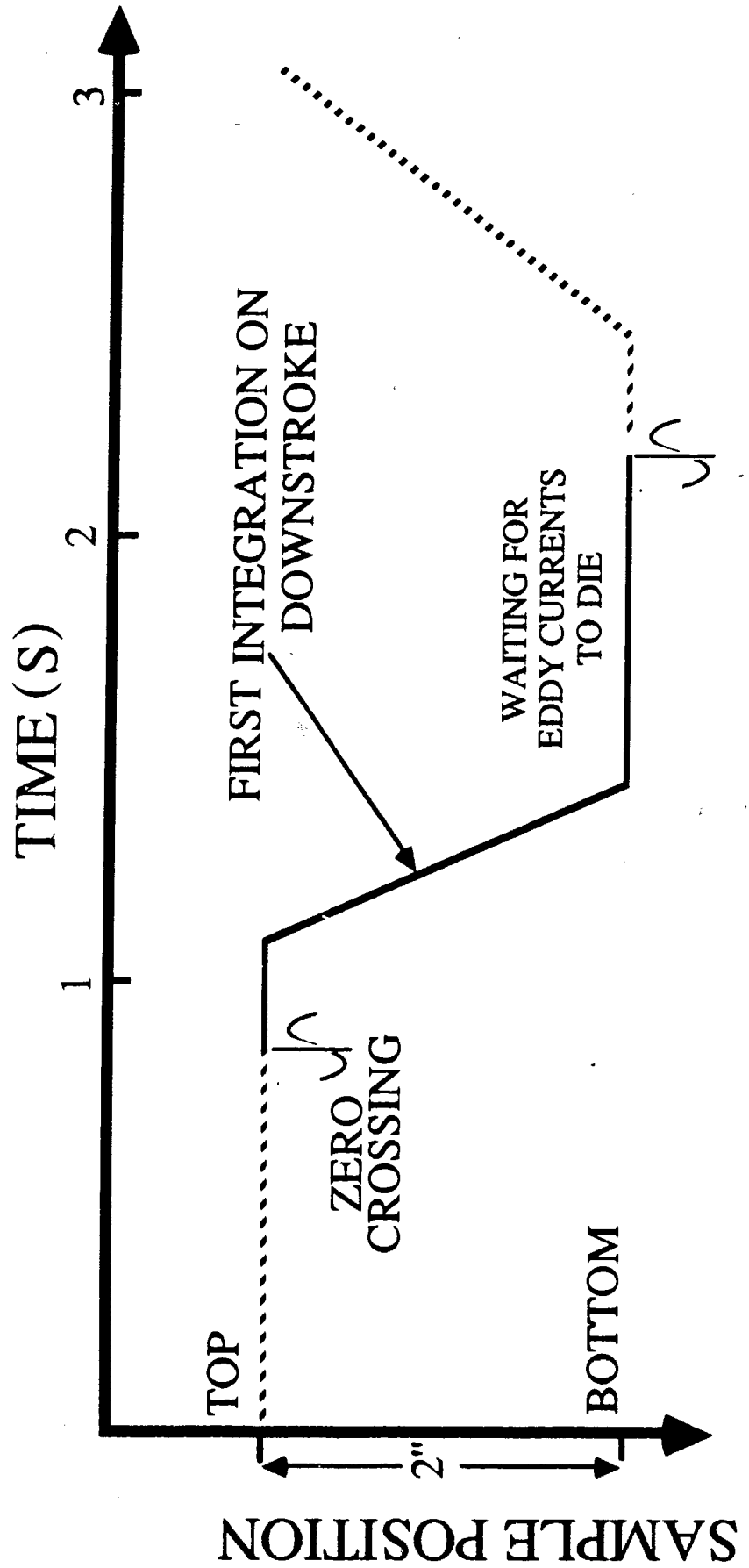

ONE FULL CYCLE OF CAM MOTION IS SHOWN.

Fig. 2.9 Timing of integration.

window. This is undesirable due to the dynamic effects mentioned above. Secondly, due to offsets in the electronics used to amplify and integrate the induce signal it is desirable to alternate integration on up and down strokes (discussed below). Three strokes shift the starting point back and forth as required. For the ~1/3 Hz motion of the CAM used this corresponds to ~4.5 sec. of sample motion. There is a delay of ~1/2 sec. between successive measurements during which the integrated signal is converted by the FLUKE 8842A voltmeter and read by the computer via the IEEE 488 bus.

Temperature control and measurement

One of two sample temperatures, hereafter T_L and T_H whose values were typically 17 and 20 deg. celsius respectively, was obtained by pumping water in a closed cycle from one of two temperature controlled 250 liter tanks (selected by computer control of solenoid valves (see fig. 2.1)). Water flowed through ~45 ft. of 3/8" I.D. polyflow tubing, well insulated with 1" walled Armourlite, tubing to and from the aluminium coil mount. Coil mount and coils, as a unit, was surrounded successively by: a few layers of aluminized mylar, packed polypropylene wool, and 1/2" thick Armourlite sheet. Measurements of the temperature of the air inside the pyrex cylinder, made with the HP quartz thermometer, indicated a ±0.02 K variation of the same period, but lagging behind, the temperature of the tank water selected.

Water flow through the coil mount is as follows. Two holes, 1/4" in diameter, on either side and running parallel to the axis allow the flow of temperature controlled water through the coil mount. Water passes up one side, separates into two channels which flow around the axial clearance hole in the machined cap, and then down the other.

From the point of view of sample temperature control, the higher thermal conductivity of aluminium relative to delrin makes a coil mount made of the former preferable as a constant temperature shroud; firstly, by reducing the thermal lag between sample and shroud and secondly by lowering the time constant of temperature reset. The pyrex tube in which the sample moves is sealed from the outside air by means of a balloon attached to its lower end which acts like a

bladder (see fig. 2.4) in response to the air displacement of the piston-like sample motion. Sealing the upper end are two delrin sleeve bushings on which which the piston rides. The thermal barrier due to the air gap between the coil mount and the pyrex tube was lessened by filling the gap with Wakefield's thermal grease. Possible heat conduction by convection through the 8 mm sample tube (or piston) was eliminated by packing the bore around the thermocouple leads with wads of teflon tape at a few points along its length. Sample temperature was measured, with the sample at rest, using a Cu-constantan thermocouple. The thermocouple junction, as shown is Fig. 2.5, is placed in a close fitting hole packed with thermal grease drilled nearly all the way through the Al tophat on which the sample sits. Removal of sample holder and tophat leave the thermocouple behind in the sample tube. The two thermocouple leads pass part the way up through the con rod emerging through a hole, above the teflon guide, drilled in its side (see fig. 2.2). The sample temperature is measured relative to a reference junction whose temperature is held to within ±0.002 K of a 33.640 K set point by the arrangement shown in Fig. 6. A measure of the reference junction temperature is given by an HP model 2801A quartz thermometer as described below.

Reference junction and an HP model 2850A quartz thermometer probe (serial no.02-32) are placed in the bottoms of two close fitting, thermal grease filled holes drilled in a temperature controlled copper cylinder. On-off control of temperature with a nichrome heater, bifilar wound around the cylinder, is effected by feedback from a thermistor. Placing the thermistor in close proximity to the heater lowers the time constant of the controller, while wrapping insulation tightly about the whole assembly prevents air currents from introducing spurious transitions. The thermal mass of the cylinder, acting like a low-pass filter, smooths the abrupt on-off heat pulses. Thermocouple voltage amplification by a factor of 1000 with a LTC1052 chopper stabilized op-amp (of very low thermal drift), using wire-wound feedback resistors, is rolled off at ~1/3 Hz. Insulated cylinder containing both reference junction and quartz probe, controller, and gain stage are all placed in the bottom of a vacuum dewar (see fig. 2.2) whose mouth is stuffed with insulation. Note that due to voltage offsets of this gain stage knowledge of absolute

temperature is uncertain. Four months after the measurements were completed sample and reference junctions were placed together in a thermal grease filled hole in the Cu cylinder. The voltage measured corresponded to a temperature of 0.3 K.

The relationship of the temperature as measured by the thermocouple to that of the sample is shown by comparing the signal variation obtained in 20 consecutive readings (no rotation) of the Ni D standard (NID) with the variation of the temperature corrected average of those 20 values. Fig. 2.10(c) makes this comparison graphically for T_L. Notice the regular periodicity and lag of up to 1 minute. A comparison is made in figures 2.10 (a) & (b) of rotation data with its temperature corrected average for NID at T_H & T_L respectively. The situation for T_H was not as favorable. Temperature steadily increases as the 20 measurements are taken in this case. This is most likely due to the fact that, at this temperature, ΔT and hence thermal transfer is not as efficient as for T_L.

The coils

The basic philosophy of the coil configuration used was discussed in the introduction. Here two effects that influenced the choice of design, signal variation upon rotation and magnetic images, are discussed in more detail. Details of coils and coil mount used are then presented. Finally the procedures used to balance the coils, against variations in the applied field, and with respect to induced signal are outlined.

Voids

Originally the fine position adjustment was made by means of a fine pitched thread on the sample mount, the sample rotating about the axis that it moves vertically along. For the Ni alloy samples, an unexpectedly large variation of signal with this rotation was observed, independent of the degree to which the sample was off axis (i.e. incongruence of rotation and geometric symmetry axis of sample). Its amplitude (relative to the signal) was found to vary from sample to sample, being particularly large for the Ni standard D (NID), see fig. 2.12(a). Unfortunately

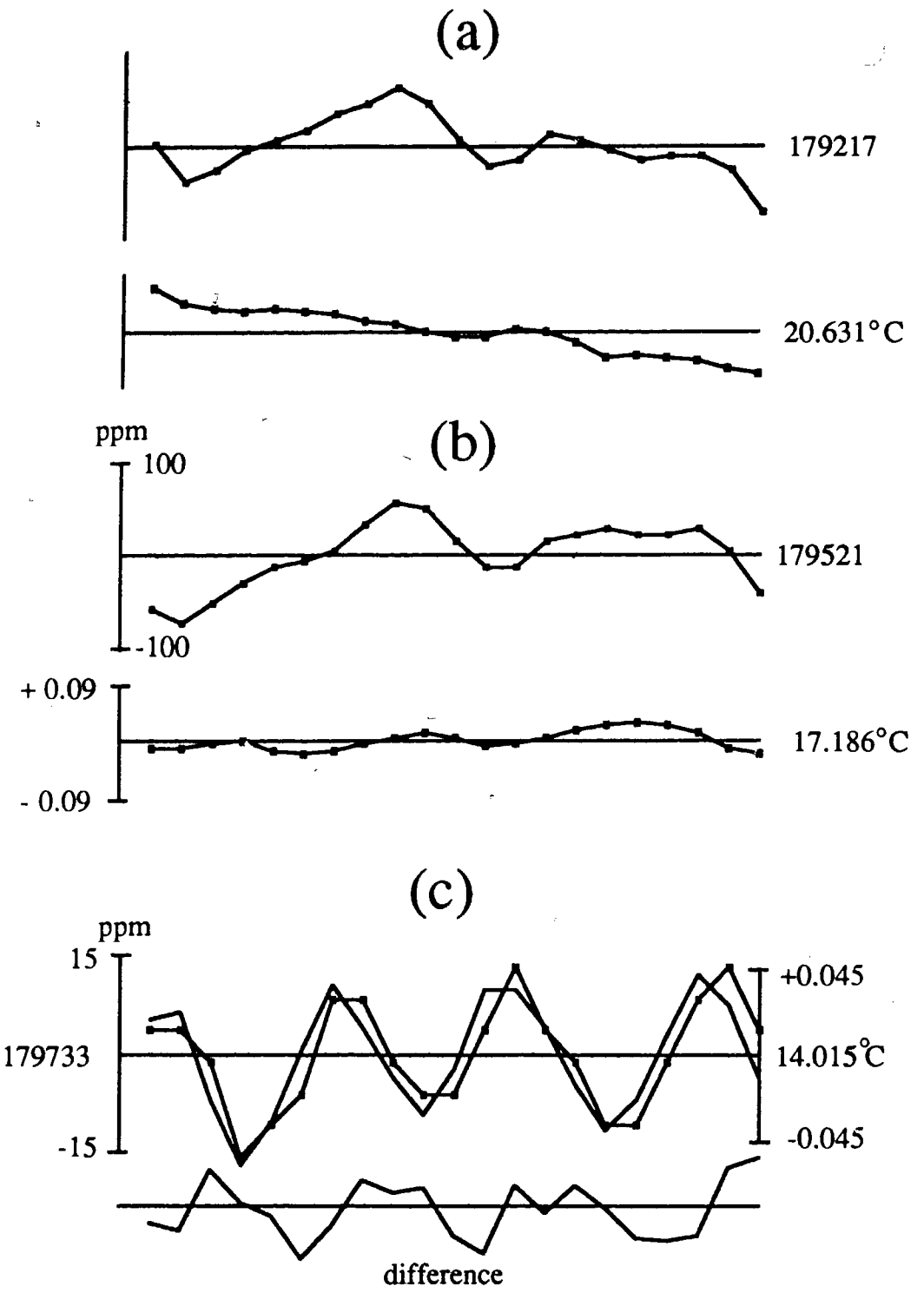

Fig. 2.10 Signal variations over a 30 min. period for NID.
(a) &(b) compare signal variations due to rotation and temperature.(sames scales for (a) & (b))
(c) compares data (no rotation) with its temperature corrected average.

the relative amplitude of this variation is larger than the precision with which measurements must be made in order to correct the muon results for the Lorentz field. A straight average of the 20 measurements may not be the best measure of the sample moment in this case. For NID the mismatch of measured and expected density mentioned above (corresponding with a ~ 2% void volume) supports the claim that an asymmetric (with respect to sample geometry) distribution of macroscopic voids may be responsible. Consider the two dimensional situation of fig. 2.11 below; in which a sample containing an off centre void, situated between two coils of area turns N_1A_1 and N_2A_2, rotates about an axis, A, that may be "off" the symmetry axis of the coil pair, P. If rotation is on axis one expects a signal variation of period π, whereas if the coils are out of balance (i.e. $N_1A_1 \neq N_2A_2$) and or rotation is off axis a 2π variation is expected. A two dimensional model of a sample containing a single spherical void was developed, which allowed the desired moment of a corresponding "voidless" sample to be determined from a fit to data. A fit of this model to NID resulted in a void with a volume of ~1.5 % (compared to the ~2 % expected from density measurements) and located near the outer edge. Unfortunately the fit was not sufficiently conclusive to be useful quantitatively. However qualitative content (i.e.origins of π and 2π contributions) of the model provides a check on the balance and alignment of the coils. Fig. 2.12(a) compares aligned and misaligned cases for NID. This unsatisfactory state of affairs was improved by the use of a more favourable pickup coil design. Fig. 2.12(b) shows the signal variation for NID with the new coils. The smallest observed signal variation with the new coils is shown in fig. 2.12(c).

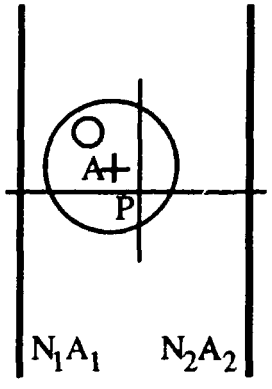

Fig. 2.11
Void model (not to scale). Offset sample with void, viewed along the cylindrical axis, A, shown displaced from symmetric centre of coils, P.

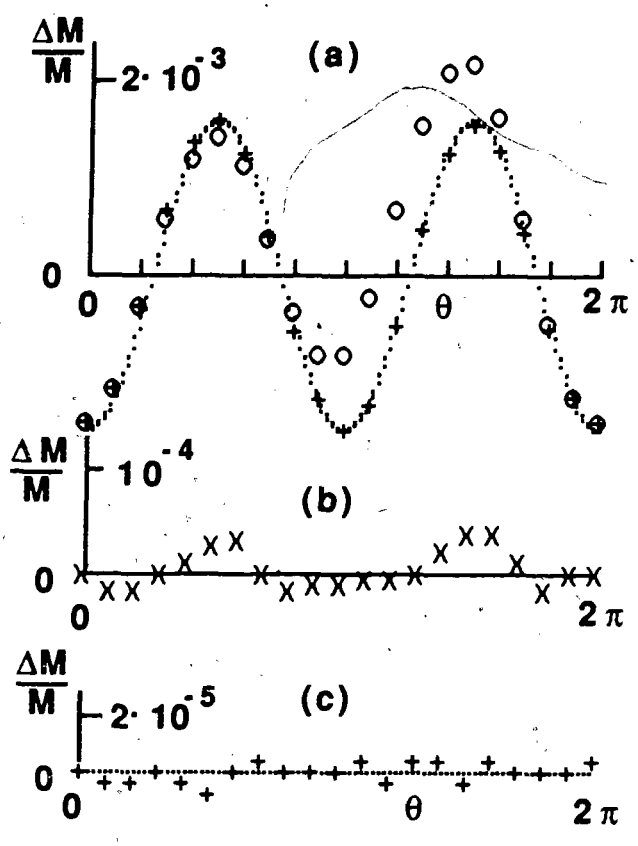

Fig. 2.12 Sample rotation by 2π.

(a) Variation of signal with angle of a Ni sample (NID) about its cylindrical axis. Comparison of signals with sample misaligned by 100μm and aligned with respect to the coil axes.

(b) Signal with larger coils than used in (a).

(c) Minimum variation data for the alloys.

Moment reduction by voids

The presence of voids does more than produce an orientation dependent signal. Canting of magnetization within a sample by the demagnetizing field of a void may reduce it's moment from that of a voidless sample of the same mass. An estimate of this effect can be made by considering a spherical sample of radius R containing a concentric spherical void of radius a. The field due to a dipole moment **m**, aligned with the z axis, can be resolved into components along and normal to the z axis; $B_z = (3m\cos^2\theta - m)/r^3$ and $B_\perp = 3m\cos\theta\sin\theta/r^3$.

For a sufficiently small void (i.e. R » a) B_z can be neglected with respect to the sample magnetization M_s and the void moment is approximately $4\pi M_s(a/R)^3/3$. Neglecting the direct contribution B_z, which goes like $(a/R)^3$, with respect to M_s, the sample magnetization is canted by the radial component $B_\perp$. Inside a spherical sample without a void $M_z = M_s$ and $B_z = H_o - 4\pi M_s/3$. With the void $M_z(\rho,\theta)$ becomes $M_s(1+(B_\perp(\rho,\theta)/B_z)^2)^{-1/2}$ which for R » a gives for, $\Delta M_z/M_s$, the relative change in $M_z(\rho,\theta)$ approximately $-1/2(B_\perp(\rho,\theta)/B_z)^2$. Reduction of the total sample moment, M, by such a void, given by integrating the above expression for $\Delta M_z/M_s$ over the spherical shell from r = a to r = R, is

$$\frac{\Delta M}{M} = \frac{3}{5}\,\frac{(a/R)^3}{\left\{\frac{3H_o}{4\pi M_s} - 1\right\}^2}.$$

For one percent voids (by volume) in a field of 12 kG, this gives an error of 300 ppm in the degree of saturation. The above must be considered an upper bound as complete cancellation, for a sample containing voids distributed randomly in both size and position, would occur between the transverse components $B_\perp$ of their demagnetizing fields. A single such void, if off centre, would induce a variation in moment with sample rotation (a quadrupole moment also appears when the void position is unsymmetrical with respect to the field direction).

Magnetic images

Pole faces of the electromagnet

The signal reflects not only the magnetic state of a polycrystalline Ni alloy sample but that of the electromagnet's polycrystalline iron pole faces as well. Spatial distribution of the flux due to sample moment and hence signal, being proportional to the flux through the pick-up coils, is a function of pole face permeability. Unfortunately pole face permeability varies with field in a nonlinear and history dependent (hysteresis) manner. When the field has been cycled between forward and reverse technical (as opposed to the limit $H \rightarrow \infty$) saturation it is, in relative terms, expected that pole face differential permeability, $\mu_{diff} = \partial B/\partial H$, be large and slowly varying below a value the order of 9 kG, above which it decreases more rapidly as the pole faces begin to saturate. Pole face permeability varies anywhere from 16,000 to 70,000 depending on purity and heat treatment of the ARMCO Fe pole faces used here[14]. Verbal communication with an individual involved in electromagnet manufacture suggests that their carbon content is from 30 to 50 ppm[24].

Field dependence of signal

Measurements, for Ni standards C, G, D and a Ni sphere of uncertain origin, of integrated signal were made in 250 G steps from 7 to 12 kG. Temperature corrected data from 9 to 12 kG are shown in fig. 2.13. Percentage slopes at 12, 10, and 8 kG of $-1.7(10^{-5})$, $3.9(10^{-5})$, and $7.8(10^{-5})$, were used to make corrections of Ni alloy data to these reference fields (see chap. 3 below). Above ~10.5 and ~11.5 kG values begin to decrease for sphere and standards respectively. This behaviour can not be attributed to the magnetic state of the samples themselves. One expects that their approach to saturation would be described by the sum of $1/H$ and $1/H^2$ terms (see theory section in chap. 1). Plots of Ni standard D (which is representative of Ni standards G and C) and Ni sphere data against both $1/H$ and $1/H^2$, are shown in fig. 2.14. Note that, below the break, the sphere data is goes more nearly as $1/H$, while for NID as $1/H^2$. The

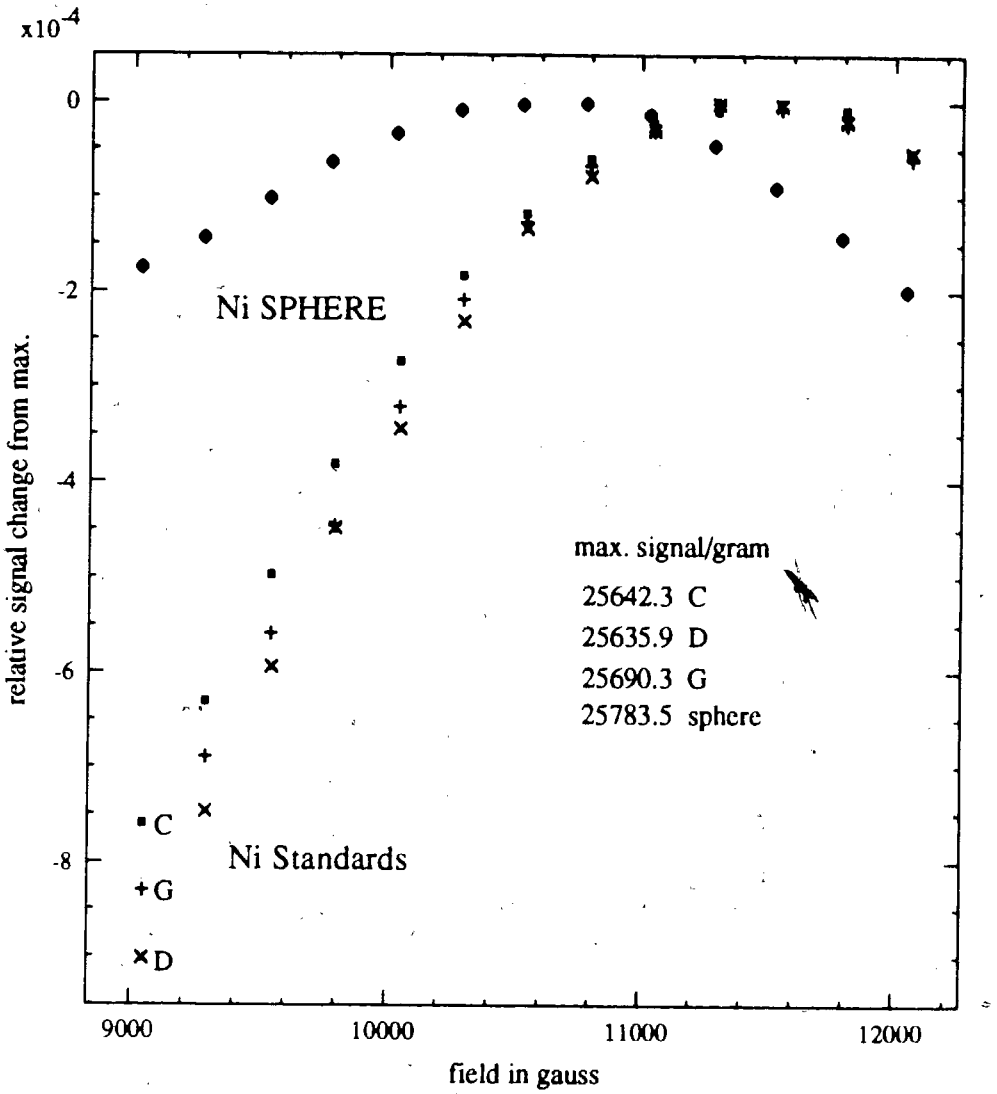

Fig. 2.13 Field dependence of signal per gram for a Ni sphere and Ni standards; C, D, and G.

Data are normalized to their maximun values, shown in the figure. The diameter to height ratios are 1.816, 1.457, and 1.027 for standards C, D, and G respectively.

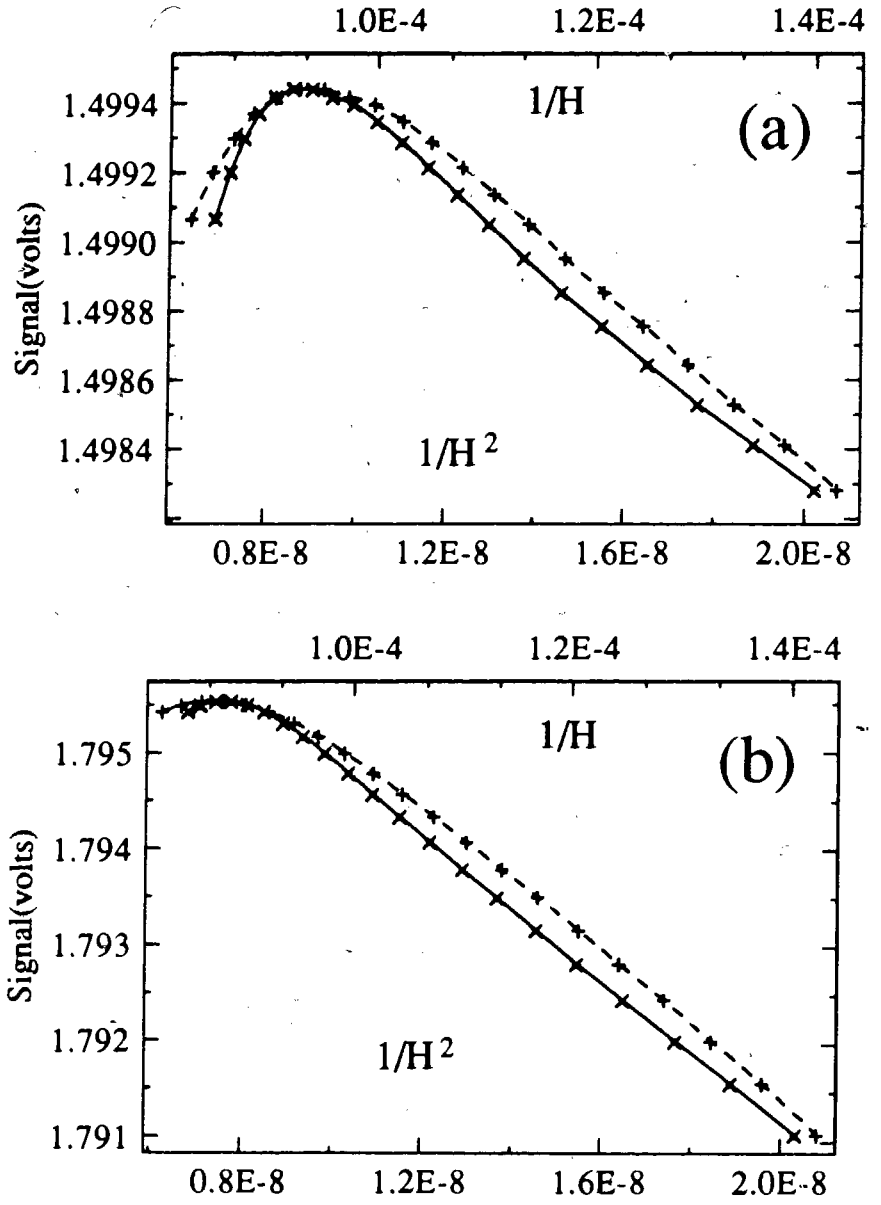

Fig. 2.14 Plots of signal versus 1/H (+) and $1/H^2$ (×) (H in gauss) for a Ni sphere (a) and the NID standard (b).

Lines are drawn to guide the eyes; broken for 1/H and solid for $1/H^2$.

most likely explanation for this difference is shape. As discussed above, the uniform demagnetizing field of a spherically shaped sample results in a linear field dependence below saturation. For the right cylindrical Ni alloy samples however the demagnetizing fields are non-uniform, field dependent, and difficult to calculate. It can be shown that the part of a sample near a sharp edge will not saturate even as $H_a \rightarrow \infty$. Consider a right angle corner with an applied field along one face. At the corner there is an infinite field pointing outwards making an angle of 45 deg. with the direction of H_a. Even though the corners of the Ni alloy samples are rounded, there still exist sizeable shape anisotropy fields in their vicinity. The approach to saturation field dependence due to these fields can be shown to be $1/H^2$ in the same way as was shown for crystalline anisotropy in the theory section. Presumably the field dependence of the Ni alloys would be of the 1/H form if they had a spherical shape.

Based on the above results for the Ni sphere, one concludes that for the highest fields attainable by the electromagnet used here, the magnetic state of the iron pole faces just begins to enter the knee or intermediate field region from in the neighbourhood of 10 kG. In the experiments described here fields were cycled between limits of ±12 kG with measurements being taken as |H| was decreased from 12 to 8 kG. The region involved extends from ~2 kG above to ~2 kG below the "break" which separates the "knee" from the low field region of the pole face magnetization curve. The above amounts to a highly field dependent contribution to the signal relative to the precision of the magnetometer above approximately 11 kG.

One might not expect[7] anything but domain wall motion in the pole faces as long as the field is less than $4\pi M_S\sqrt{3}$ = 12.4 kG for a polycrystalline material on a major hysteresis loop. That the susceptibility of the pole faces decreases noticeably before this geometric limit may be related to the fact that the pole faces are on a minor loop. Decreasing images at higher fields is a well known phenomena[25]. That it occurs below the "knee" was not appreciated by us. Perhaps the assumption that all grains choose to magnetize along the easy axis closest to the applied field is incorrect.

Image calculations

Results of idealized calculation of the effect of pole face permeability are now presented. This boundary value problem is idealized by considering a purely dipolar sample moment normal to and between two parallel, planar pole faces of permeability μ and infinite extent. Utilizing the method of images, the portion of the signal due to the presence of the pole faces is estimated as the image contribution to the flux through the pick-up coil, due to the coaxial dipole sample. The magnitude of an image charge Q_i in a half plane of permeability μ is related to that of the sample Q_s as

$$Q_i = - Q_s \left[\frac{\mu - 1}{\mu + 1}\right].$$

This result follows from the required continuity at the interface of the magnetic potential ϕ (defined $\mathbf{H} = -\nabla\phi$ which may be introduced in the absence of currents since then $\nabla \mathbf{x} \mathbf{H} = 0$) ensuring finite fields and that of the normal component of $\mathbf{B}$ which follows from $\nabla \cdot \mathbf{B} = 0$. Note that images are convenient fiction. More correctly, a charge (or dipole) induces on the surface of the polar ($\mathbf{M}$) half plane (pole face) a magnetic charge density $\sigma_m = - (1/4\pi) \nabla \cdot \mathbf{H}$. Magnetic dipole moments, $\mathbf{m}_i$ and $\mathbf{m}_s$, consisting of two closely spaced, equal and opposite charges, are thereby related

$$\mathbf{m}_i = \mathbf{m}_s \left[\frac{\mu - 1}{\mu + 1}\right].$$

In low fields $\mu \gg 1$ so that sample and image moments are parallel, collinear and nearly equal in magnitude. For a sample between two such half planes (pole faces), two infinite series of image moments, each with a regular image to image spacing of twice the respective pole face to sample distance, are parallel to, collinear with and on either side of the sample moment.

Using the reciprocity of mutual inductance, it may be shown[4] that the flux, $\Phi(r,z)$, through a circular wire loop of radius R about the origin and in the $z = 0$ plane of a cylindrical coordinate system (ρ,θ,z), due to a dipole moment of magnitude m, aligned with the z axis at (ρ,θ) is

$$\Phi(\rho,z) = \frac{2m}{\sqrt{(R+\rho)^2+z^2}}\left(K(k) + E(k)\,\frac{R^2-\rho^2-z^2}{(R-\rho)^2+z^2}\right), \qquad (2.1)$$

where

$$k^2 = \frac{4\rho R}{z^2+(R+\rho)^2}$$

and K and E are complete elliptic integrals of the first and second kind respectively. The on axis ($\rho = 0$) version of the above is

$$\Phi(r) = \frac{2\pi m}{R}\,(1+(r/R)^2)^{-3/2}. \qquad (2.2)$$

This expression falls off from a maximum of $2\pi m/R$ at the origin in a bell-shaped fashion.

Using the expression (2.2) for flux due to an axial dipole, the relative contribution of sample and image moments to the flux were calculated for the idealized situation, of a dipolar sample and a coaxial pair of identical circular coils of finite extent, situated symmetrically with respect to, two parallel, planar pole faces of permeability μ and infinite extent. Separation of the pole faces and dimensions of the coils are in the same ratios as the experimental values. Old and new coils have ~2000 turns of #40 and ~2300 turns of #42 gauge copper wire. Coil dimensions (inches), O.D. x I.D., are .94 x .57 and 1.99 x 1.74 for old and new coils. Finite circular coils are idealized by considering the sum of flux through each of NxM disjoint circular turns which are distributed so as to form in cross section a rectangular array N wide and M deep. Width by depth (inches) for old and new coils are .225 x .185 and .183 x .125. Fig. 2.15(a) shows a comparison of the relative change (in parts per hundred thousand or ppht) of the axial coupling for pairs of coils modeled after the old and new coils as a function of the distance of a dipole

from the symmetric centre. Old and new coil data of variation of signal upon rotation are compared in fig. 2.12. It is seen that new coils approximate the ideal of a position independent coupling. The contribution of 40 pairs of images were taken into account in this calculation. Images account for ~20 % and ~5 % of the total signal for new and old coils respectively. A comparison of the relative change in coupling with and without 40 image pairs is shown in fig. 2.15(b). Images create a minimum at the origin where a maximum existed before. This result is reasonable considering that the first pair of images dominate the image contribution to the axial coupling. The change in these two image positions is such that they compensate for the reduction of the flux due to sample alone. As the dipole is moved towards a pole face the nearest image in this pole face increases its contribution by an amount greater than the decrease of that of the nearest image in the opposite pole face. These encouraging results must be supported by a more realistic calculation.

In order to approach the actual situation a calculation is made, for 2 identical sets of coil pairs, using (2.1). Again symmetric positioning of dipolar sample, coils and pole faces is assumed and the contributions of 40 image pairs are included. The finite coils are approximated by single turns situated at the geometric centre of coil cross sections (this was shown to be a good approximation by comparison with coils for which 20 turns were distributed in over the finite coil cross section). Contributions of flux from upper and lower pairs are of opposite sign (corresponding to the series opposition of the two coil pairs in practice). Fig. 2.15(c) shows a comparison of the new coil axial coupling for one and two pairs. The more "complete" two pair picture is seen to flatten the coupling at the origin but cause it to fall off more sharply for axial displacements beyond 0.1". Note that the two pair relative change corresponds to that obtained from the 2" vertical displacement of the dipole from between one pair to the other. The one pair result corresponds to the extraction of the dipole from its axial position to a point sufficiently far away that the coupling is negligible. In fig. 2.15(d) results are shown of the relative change in coupling upon making a 2" vertical stroke between corresponding points as a function of the displacement of the stroke endpoints along three mutually orthogonal directions from the centre

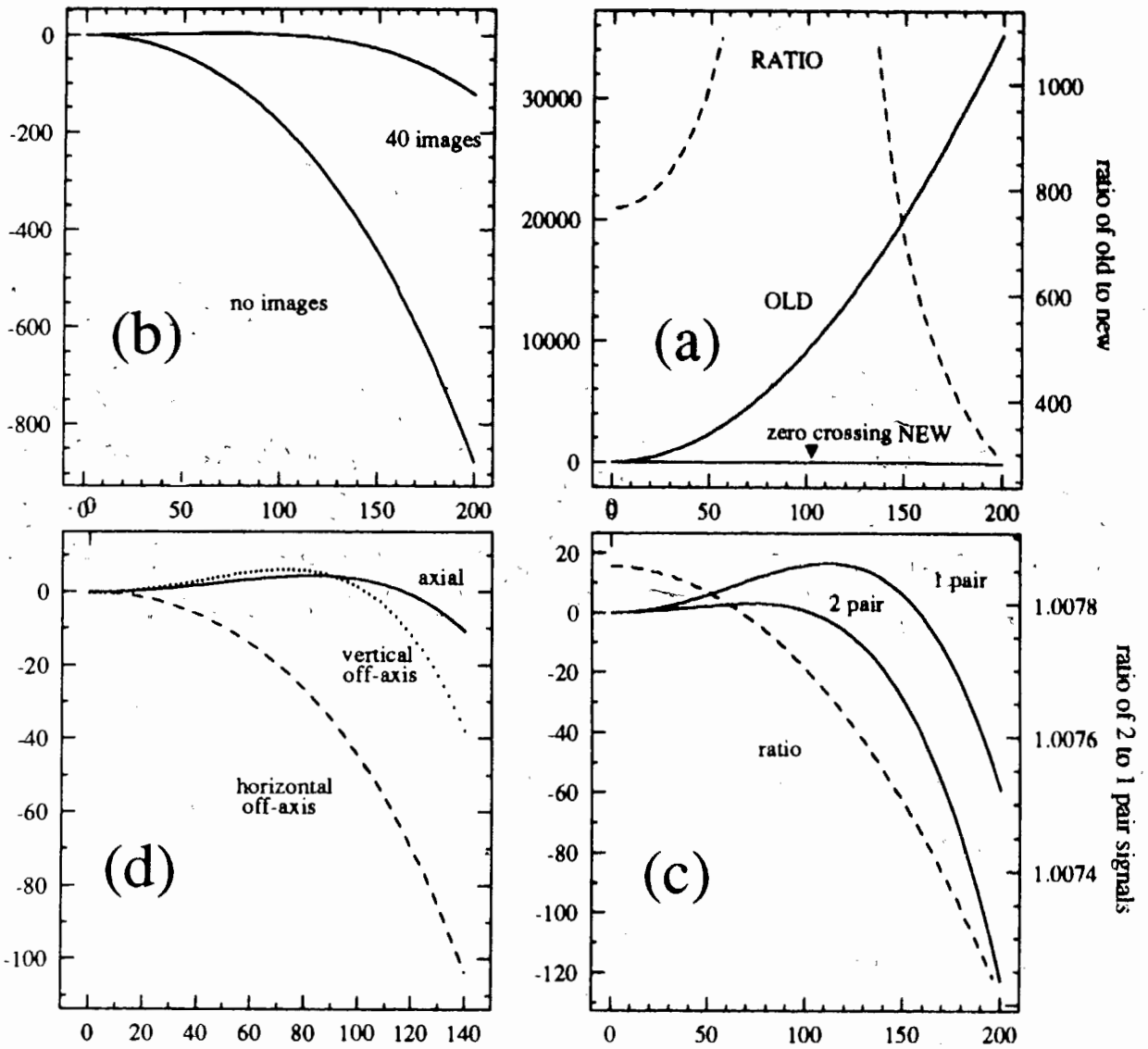

Fig. 2.15 Ideal calculations of dipole coupling to coils

Abscissae are displacement (in 0.001") of dipole position(s) from the centre of a coil pair (origin). Ordinates are relative change from the origin of flux coupling or signal in ppht..
(a) Comparison of axial coupling between OLD and NEW coil pairs.
(b) Axial coupling, with and without 40 images, to a single coil pair.
(c) Axial coupling compared between 1 and 2 NEW coil pairs.
(d) Signal variation in 3 orthogonal directions for NEW coils.

Note that (c) and (d) include the contributions of 40 image pairs.

of a coil pair. Vertical off-axis (along the stroke axis) coupling is also "improved" by the presence of images. The horizontal off-axis, lacking any kind of image compensation of the sort described for the axial one pair case, is seen to be the worst case. Although not shown here, results for two pairs generally confirm the conclusions regarding the effects of images and relative coupling of new and old coils reached for the one pair axial situation. In summary the new coil arrangement decreases the sensitivity of integrated signal to sample positioning while increasing the image contribution.

The extent to which the results of the above calculations reflect actual experimental conditions has not been systematically verified. Tedious simulations of unbalanced coils and asymmetrical position of coils, pole faces, and sample stroke could be made, but the usefulness of the results is doubtful. Assuming that the quantitative results shown in fig. 2.15(d) may be trusted, the possibility that the variation of signal upon rotation is due to a "wobble" of the sample as a whole may be ruled out.

Coil and coil mount design

Each coil had ~2300 turns of insulated #40 AWG copper wire wound randomly on the delrin form shown in fig. 2.16. They are attached to the coil mount with nylon screws by means of the two off centre clearance holes (see fig. 2.2). The large central hole aids alignment of a coil with accurately scribed markings on the coil mount (see fig.2.2). The coil mount itself, shown in fig. 2.17, had the two surfaces which accept the coils milled at the same time to ensure their parallelism. Separation of these flats is ~0.006" greater than the 15 mm diameter of the vertical clearance hole through which the 14 mm O.D. pyrex cylinder passes. Two holes, 1/4" in diameter, on either side and running parallel to the axis allow the flow of temperature controlled water through the coil mount. As shown in fig. 2.17 water passes up one side, separates into two channels which flow around the axial clearance hole in the machined cap (not shown), and then down the other. The whole assembly, coils and mount, is attached to the pole faces of the electromagnet through one of three plexiglas H-shaped wedges shown in Fig. 2. Eddy currents

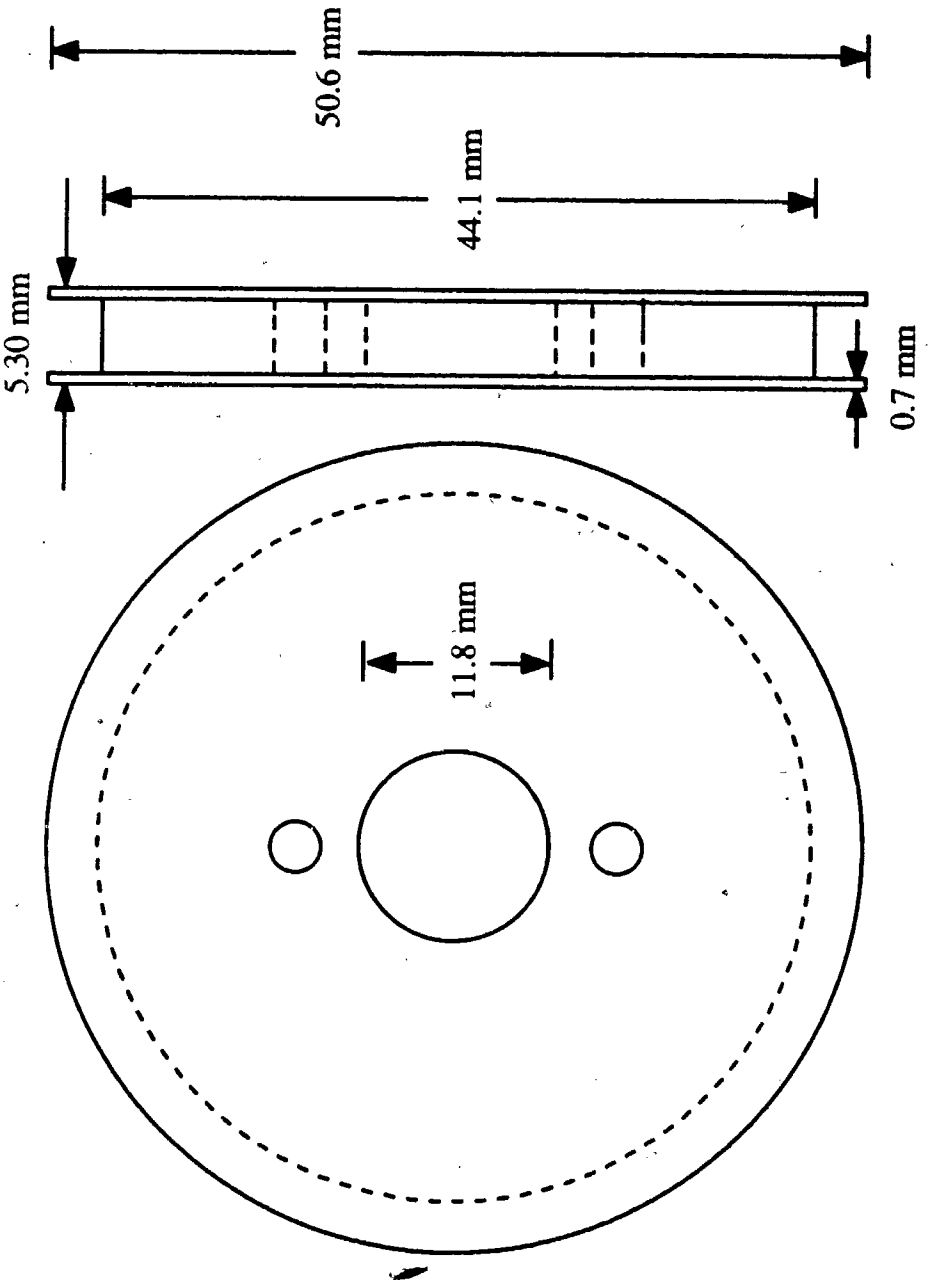

Fig. 2.16 Coil form 2:1 scale (material delrin)

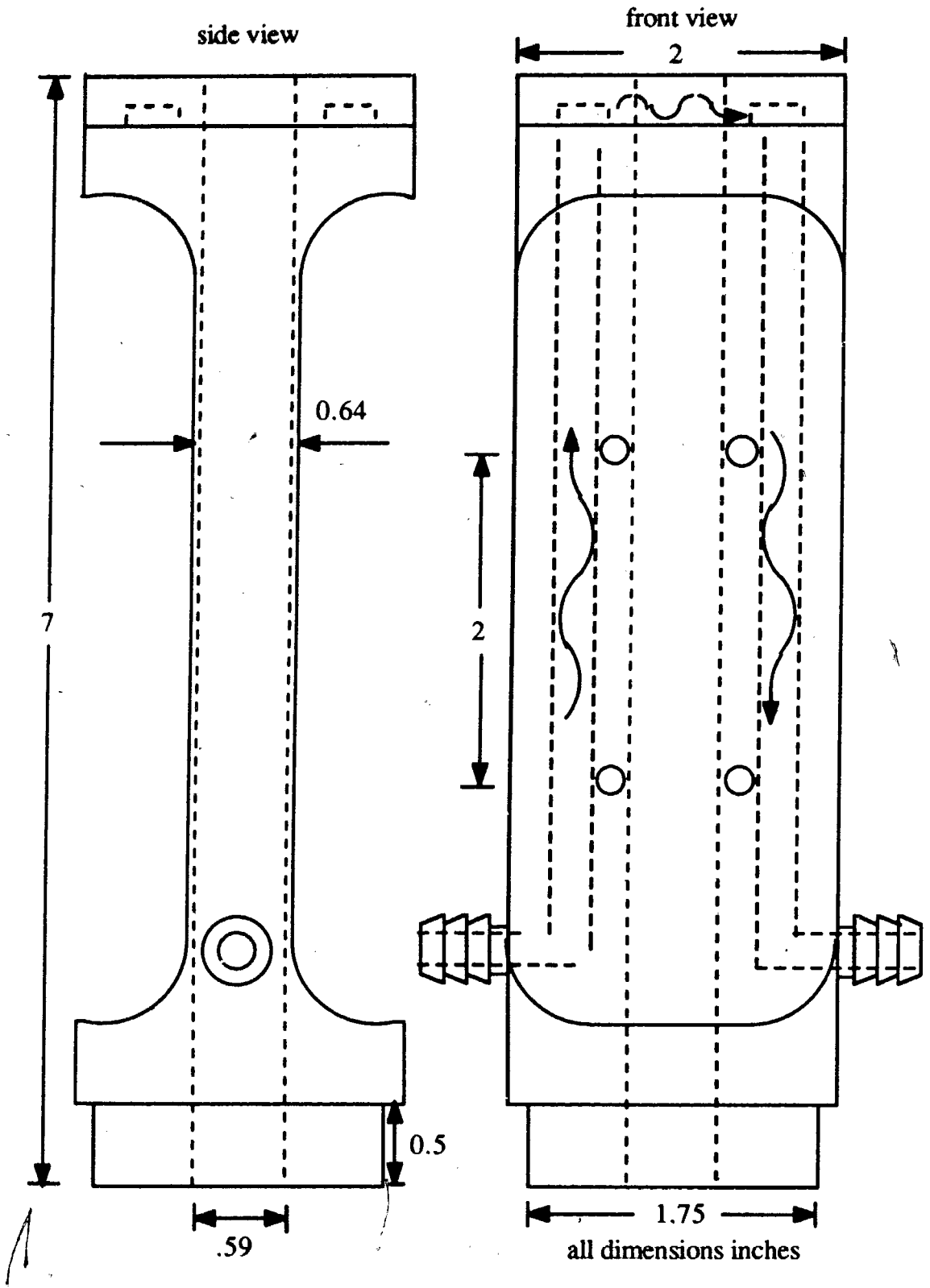

Fig. 2.17 Coil mount 1:1 scale (material aluminium)

in the coil mount produced by sample motion were found to restrict the penetration of sample flux thereby reducing the signal. On increasing the integration period from 64 to 100 zero crossings of the 60 Hz line voltage (see "Timing of sample motion" above), the signal was seen to increase in an approximately exponential approach to a limiting value. In order to put to rest any doubts about the effect of the presence of the Al coil mount, a delrin coil mount of the same dimensions was made. Measurements of 0.9900 cm and 1.0000 cm diameter iron spheres were taken under the same field and temperature conditions with both coil mounts. Ratios of the signals of the iron spheres were found to be the same for the two coil mounts to within 10 ppm. This is within uncertainties of sample temperatures and densities[27].

Balancing of coils

Coils were balanced with respect to both applied field and sample motion. Integration of the signal obtained upon ramping up the applied field was used as an indicator of field balance. The smaller the integrated signal, the better the balance. Upper and lower pairs were balanced against one another by removal of turns from the coil with the largest contribution in the dominate pair. Balance with respect to sample motion was effected by placing 0.005" mylar spacers under a coil in order to modify the amplitude of the variations of its integrated signal obtained upon 2π rotation of the nickel "D" sample. An iterative procedure brings the amplitudes of these variations into collective agreement without significant loss of applied field balance. As mentioned in the discussion of voids above (see fig. 2.12), the variation of the integrated signal from all four coils with sample rotation gives an indication of the overall coil balance with respect to sample motion.

Electronics

In this section the signal is followed from its source at the pick-up coils, to the digital representation of its time integral at the computer. The prime objective is that this number,

excepting an offset to be explained below, be proportional to sample moment. Factors, related to electronics, that prevent the above from being true are discussed below in turn.

The source, consisting of four series connected, "wild wound" coils of ~2300 turns of #42 gauge copper wire, has a nominal d.c. resistance of 7.32 kΩ. For each coil, it's two leads are taken as a twisted pair through a shielded cable to a set a switches, located on the wooden rack, which allow independent selection of the signal across it, allowing balance of signal due to both applied field variation and sample motion to be made.

A digitized version of a scope trace of the signal appearing across the coils upon a downward stroke of the Ni D standard is shown fig. 2.18. The form is that of the superposition of two similar bell shaped curves. The second, corresponding to the contribution of the lower pair, is smaller in amplitude than the first. Note that the leading edge is sharper than the trailing edge. For an up stroke the trace is lower, broader and more symmetric. Due to gravity the down stroke is twice as fast as the up stroke. A likely explanation for the relatively complex shape of the down stroke trace may stem form the fact that in this case (not so for an upward stroke) the plywood board to which the driving mechanism is bolted is free to bow upwards. Stored energy from the back reaction against static friction is released at the beginning of the stroke resulting in observed asymmetry between upper and lower pair contributions. In order to test the dependence of the integrated signal on stroke speed, stroke speeds were adjusted by means of two springs mounted between the fixed CAM body and the moving stepping motor. The springs allowed the "reversal" of up and down stroke speeds. Both up and down signals were seen to increase with stroke speed by ~3 parts in 100000 for the difference between up and down stroke speeds. A possible explanation of this result is that a faster stroke allows more time for eddy currents to die away.

To achieve the prime objective, variations of critical circuit parameters, must be kept to a minimum over the period of time (typically 9 to 12 hours) required to take measurements on a sample and it's flanking pair of standards. Variations due to changing temperature and associated temperature gradients are of primary importance. Electronics are maintained in the temperature

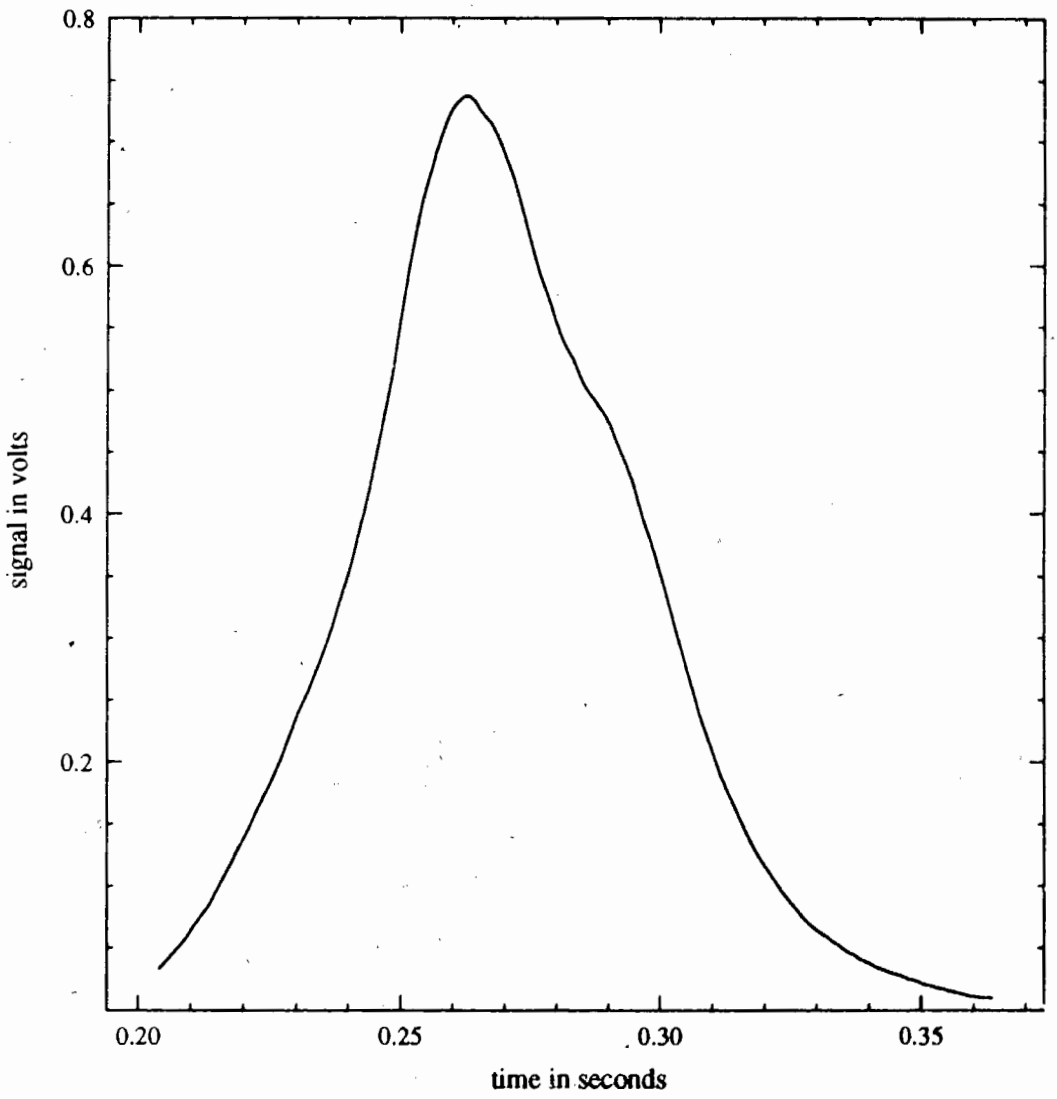

Fig. 2.18 Induced signal for a down stroke of NID standard. The total signal is the sum of contributions from upper and lower coil pairs. Note the shoulder near 0.28 sec..

controlled (to ±0.02 K) chamber described above. Gradients result from either air currents or self heating of components. The former is reduced by packing polypropylene wool around the components while the latter is kept to a minimum by designing for low power levels (i.e. high impedance loads for voltage sources and low impedance for current sources). In what follows temperature coefficients (hereafter designated T.C.) are often given as fractional changes in ppm of component values.

Analog board

A schematic of the analog board is shown below in fig. 2.19. The signal is carried to the analog board by ~3 meters of Belden 9452 shielded cable (twisted pair with low microphonics). Starting on the left hand side of the schematic, the cable shield is connected to one end of the pick-up coils. Analog board components are soldered onto a Vector 3677-2 6.5 " ready-made printed circuit board. The board is carefully cleaned afterwards to prevent excessive leakage. Analog common from an off board ±15 VDC power supply is connected to the broad copper trace that runs around the periphery of the board. The rake-like symbol indicates connections, made with 1/16 " copper bus wire, to a common ground point on the board edge.

Analog board function is shown most clearly by breaking it up into three independent stages; gain, integration, and sample and hold.

Gain stage

First and, from the standpoint of short term reproducibility most important, is the gain stage. An LTC OP07 EN8 operational amplifier (op-amp) is configured as a non-inverting amplifier. It's input offset voltage may be adjusted by means of an Ultronix 2.2 kΩ high precision (T.C. < ± 10 ppm/K) trimpot shown in the network above the OP07. Two 8 kΩ Ultronix metal foil resistors (T.C. ± 5 ppm/K) increase the sensitivity of adjustment. Signal gain is given by the expression $1+ Z_f/R_1$ where $Z_f = R_2/(1 + j\omega R_2 C_1)$. The resistor R_2 is a Caddock model TF020R 100 kΩ thin film resistor (T.C. ± 5 ppm/K). C_1 is a Philips model 368MKT

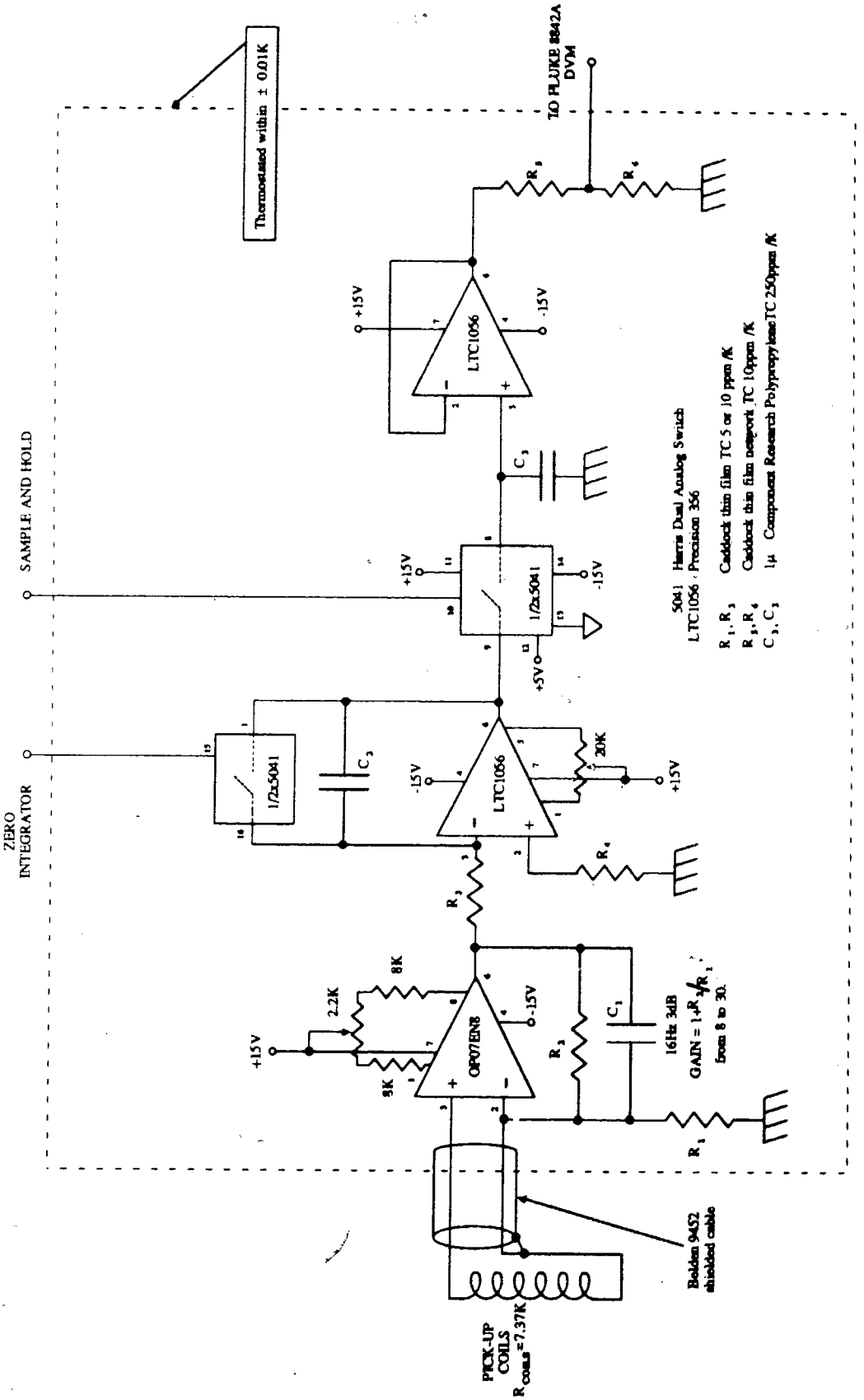

Fig. 2.19 Schematic of induced signal integration electronics

0.1 μF metallized polyester capacitor. Together they form a low pass filter with a 3 dB point of 16 Hz, causing the gain to roll off by 6 dB/octave. D.C. gain is adjusted by replacing R_1 by the appropriate value. In order to retain the maximum available resolution of the FLUKE 8842A voltmeter (1 part in 200,000), gain is adjusted so as to maintain an integrated output of just less than its 2 volt full scale. The values of R_1 used for samples with diameters matching those of D, A, and G standards are 10, 8, and 16 kΩ respectively. These values are made up of combinations of a 10 kΩ version of the thin film resistor and two of the 8 kΩ metal foil resistors described above.

Certainly the most important factor limiting the sensitivity of this system at its full resolution (i.e. determines its maximum dynamic range) is the drift of the input offset voltage V_{os} of the OP07 op-amp. A constant offset voltage results (for both up and down strokes) in a linear ramp upon integration. Due to the opposite polarities of up and down strokes, the contributions of a constant offset to their integrated signals cancel when these signals are added in absolute value. Variations of V_{os} over a period of time small compared to the ~5 sec. necessary to perform consecutive UP and DOWN integrations will contribute to error. Temperature variations on this time scale are highly unlikely when air currents across the op-amp inputs are avoided. The chief contribution to signal noise is from V_{os} noise in the bandwidth of integration. Such voltage noise is inherent and has a 1/f type density. Increasing the gain while integrating with a good quality 7 kΩ resistor clearly illustrates the problem. For large gains (>20), after initially adjusting the drift to zero (see below), the difference between the magnitudes of up and down stroke changes rapidly with time. In order to minimize the size of such contributions the magnitude of V_{os} is initially reduced by "zeroing" the consequent drift (linear ramp mentioned above) of integrated signal. The procedure used is as follows. With both analog switches closed (resulting in a "zero integrator and sample" action of the analog board) the V_{os} of the 1056 op-amp (used as an integrator) is adjusted by means of the 20 kΩ trimpot until the FLUKE shows a zero voltage output from the analog board. Now opening the "zero integrator" analog switch (resulting in a "continuous integration" action of the analog board) the V_{os} of the OP07 is

adjusted (by means of its 2.2 kΩ trimpot) until the output voltage changes with time as little as possible. Adjustments of these trimpots are made from outside of the styrofoam box by means of two ~2 foot long flexible fiberglass screwdrivers.

Integrator

Ideally the LTC 1056 CN8 (precision 356 type) op-amp shown in fig. 2.19 would produce an output, V_{out}, related to the input from the gain stage, V_{in}, as

$$V_{out} = -\frac{1}{R_3 C_2} \int_0^T V_{in}\, dt\ , \qquad (2.3)$$

where T is the intergration period (see fig. 2.9). In practice non-ideal op-amp behaviour and thermal drift of R_3 and C_2 values introduce inaccuracies. Because of its low (pA) bias currents a FET op-amp is used. A 1μF (50 VDC) CRC model K93 polystyrene capacitor, combines good temperature stability -100±50 ppm/K (note the negative temperature coefficient) with very low leakage and dielectric absorption (memory effects). Resistors R_3 and R_4 are 75 kΩ metal film resistors having 50 ppm/K temperature coefficients. Assuming an overall 200 ppm/K temperature coefficient for the integrator stage, temperature stability to 1 part in 200,000 requires temperature control to within ±0.01 K. This suggests that the capacitor, with its large thermal mass (length 1", diameter .75"), may be responsible for long term drifts (as compared with the V_{os} noise mentioned above). Problems with the input offset voltage of the 1056 are reduced by large R and C values and zeroing of the integrator before every measurement. This is done with one of the 2 analog switches (R_{on} ~ 20 Ω) of the Harris 5041 dual analog switch.

Sample and hold

As shown in fig. 2.19 analog switches control all board functions. Switching occurs on zero crossings of the 60 Hz line. At the end of an integration period the sample and hold switch

breaks ~90 ns before the integrator is zeroed. The hold capacitor, C_3, is the same type as C_2. A 1056 (low droop) connected as non-inverting follower supplies the integrated signal to 4 x 1 kΩ Caddock thin film resistor network connected as a x 1/4 divider. This analog voltage (< 2 V) is converted to digital in ~300 msec by the FLUKE 8842A. Leakage due to analog switch, capacitor, and follower cause this voltage to change with time (commonly called droop). Droop during conversion as inferred from repeated measurements, at a 1.25/sec. frequency, after integration, was found to be, $\Delta V/\Delta t$ ~ 4 counts/sec. (a count being 10 μV on the 2 V scale, or 5 ppm of the integrated signal). This would correspond at the hold capacitor to an effective leakage current, $I = C(\Delta V/\Delta t)$, of ~0.2 nA (there is a 0.8 nA maximum specification for the analog switch). The above droop during conversion likely amounts to an acceptable reduction of the signal by 5 ppm.

2.4 Experimental procedure

As mentioned in the introduction uncertainty as to the affect of shape on sample saturation necessitates that alloy measurements be made relative to Ni standards of the same size and shape (and metallurgical origins). Measurements are made "near" the 6 fields; ±12, ±10, and ±8 kG, and two temperatures; 290.45 K and 293.55 K. Twenty consecutive measurements, separated one from the next by a π/10 sample rotation, are made. The average of these twenty measurements is taken as a measure of the sample moment at a given (one of twelve) field and temperature. The integration of the induced signal is not what is meant by "measurement" above.

Measurement

To eliminate offsets, integrations on up and down strokes are alternated. After every four such integrations, with the sample stationary, the field is measured with the NMR magnetometer. In this way fourteen integrations and four field measurements are made. An average of the last thirteen integrations is what is referred to above as a measurement. Each measurement takes two minutes. Associated with each measurement are a field: the average of

the four NMR measurements, an orientation, and a thermocouple voltage. Following a measurement of moment, with the sample at rest, five consecutive samples of thermocouple voltage are made. The average of these five and knowledge of the temperature of the reference junction temperature from the HP quartz thermometer allow a sample temperature to be calculated later. After these five voltage samples have been made, either the sample is rotated by $\pi/10$ and this process is repeated or, if that was the last of twenty measurements, the sample is rotated a full 2π in the opposite sense. This "rewinding" is necessary due to the thermocouple leads. After rewinding the field is changed.

Initializing a run

Once temperature equilibrium has been reached (see below) and a rough vertical positioning of sample has been made, the drift is zeroed as described above in "Gain stage". Fine tuning of vertical positioning is then made with the "lab jack" shown in fig. 2.2. The sample is positioned at the maximum signal point. This is taken as the point midway between two points of equal signal above and below it.

Temperature and field changes

Six sets, one for each field, of these twenty measurements are made for the low temperature T_L and then repeated again for the high temperature T_H. If more data is taken, temperatures alternate. Upon initial startup or temperature change it is necessary to allow the sample temperature to equilibrate. Achievement of temperature equilibrium is made in the following manner. Measurements are repeated without field changes or sample rotations. After each measurement the standard deviation, s, of the previous five measurements is compared with a critical value. When s is less than that value measurements proceed.

For each temperature, fields (in kG) are changed, possibly starting from a no field, initial startup situation, in the following order; 12, 10, 8, -8, -10, -12. This order moves the pole faces through a minor loop as discussed above. After each field change there is a delay of two minutes

while magnetic aftereffects decay. If for some reason the field is lost, the field is recycled to its present value and the run continues.

Time scale and summary

A set of 20 measurements takes ~1/2 hour. This corresponds to six hours for two temperatures. Not included are time delays for field and temperature changes. In total, eight hours were required to obtain the required minimum of data for a given sample or standard. In general, sample runs and standard runs were done during the nighttime and daytime respectively. This is due to the more favourable noise level at nighttime and the fact that flanking standard runs were averaged.

Chapter 3. Results and discussion

The procedure used to measure the magnetic moment per gram of Ni alloy samples (and their standards) is now briefly summarized. Samples move from the centre of one pair of detector coils to the centre of another pair. Measurements are made with symmetry axes perpendicular to the field in fields of ±12, ±10, and ±8 kG. At each field, samples are rotated about the symmetry axis, twenty measurements being made in steps of $\pi/10$. After a set of field cycles the temperature is changed by ~3 K and measurements repeated. Each of the alloys corresponds in size and shape to one of a set of Ni samples. Alloy runs are alternated with those of the appropriate Ni standards.

3.1 Data reduction and reproducibility

For each field and temperature there are twenty sets of numbers recorded. These sets consist of the an integrated signal (average of 13 individual integrations), a NMR magnetometer measure of applied field, and a Cu-constantan thermocouple voltage. An iterative procedure was used to convert thermocouple voltages, E(μV), to temperatures, T(K). Low, T_L, and high, T_H, temperatures were taken as the value $T = T_{ref} + E/(dE/dT)$ (using initial values for dE/dT of 40.5 and 40.7 for T_L and T_H respectively) obtained after 4 iterations with the linear fit to data[26], $dE/dT(\mu V/K) = 0.352(T - 15.85)/4 + 40.127$.

For alloys, averages of these three sets of numbers were used to arrive at an integrated signal corrected to the appropriate temperature and field references. For standards the average of corresponding values from flanking standard runs were used.

Temperature and field corrections

Temperatures were less reproducible than fields. Typically, percentage corrections for temperature and field were 0.01 and 0.0005 % respectively.

For each field linear corrections were made to the temperatures T = 290.45 K and T_1 = 293.55 K using the quantity,

$$\frac{1}{\langle\sigma\rangle}\frac{\Delta\sigma}{\Delta T} = \frac{2}{T_L - T_H}\left(\frac{\sigma(T_L) - \sigma(T_H)}{\sigma(T_L) + \sigma(T_H)}\right) \qquad (3.1)$$

where $\sigma(T)$ is the integrated signal per unit mass at the temperature T.

Data were corrected to the fields, |H|; of 12, 10, and 8 kG. Linear field corrections of all data (alloys and standards), using slopes obtained from data for the Ni D standard (see "Field dependence of signal" above), were small. The final result was independent of whether field corrections were made before or after temperature corrections.

Reproducibility of integrated signal

Data, corrected to a given field and temperature, are reproducible to ±5 ppm in the short term (from ~5 sec to perhaps a few.hours to a day). Reproducibility in the time scale of days to months is at worst ±20 ppm.

Precision of magnetometer

Resolution of a measurement (i.e the average of 13 consecutive integrations (see "Procedure " above)) is that of the FLUKE DVM used as A/D converter; 1 part in 200000 or 5 ppm. Precision is equivalent to resolution if the magnetometer is linear.

Linearity is checked by comparison of the field and temperature corrected signals of two Fe spheres of diameters 0.9900 and 1.0000 cm. Their usefulness as standards serves to illustrate the drawbacks of the Ni alloy samples. The spheres, besides having the same metallurgical history, were subjected to rolling and kneading procedures in order to achieve uniformity of density and a random distribution of small grains[27]. In contrast, Ni alloy samples have a non-ideal shape, voids, large grain sizes, and in some cases a non-uniform distribution of solute (i.e. precipitation). A comparison of Fe sphere moments is both easier and more appropriate than the

measurement of an alloy moment relative to that of its matching standard. Spherical shape results in moments that are more nearly independent of field (i.e. closer to saturation) and ensures that the effect of diameter difference is minimal. Relatively uniform densities yield results that are largely independent of sample orientation. In addition the higher T_c of Fe results in a reduced temperature dependence of magnetic moment. Ratios of signal agree within ±5 ppm at each of several preamplifier gains. Agreement with the ratio of the weights is consistent with expected variations[20] of density from sample to sample; ±20 ppm.

3.2 Magnetic moment per gram

Here the best possible interpretation of data as moment per gram are presented. As mentioned above, from the point of view of magnetic moment measurements these samples (alloys and standards) are less than ideal in three respects; shape, voids, and large grain size (such that the number of grains is small). The first is dealt with by considering alloy moments relative to Ni standards of the same size and shape, while the effects of the last two are minimized by averaging over 20 orientations of the sample with respect to the magnetometer. Possible reduction of magnetic moment by voids is unavoidable with these samples however. Finally, averaging over the six fields both improves statistics and reduces the role of possible differences in field dependence between an alloy and its standard.

Results are presented in table 5 below of the percentage change in magnetic moment per gram of a given alloy relative to that of its standard and the corresponding alloy temperature derivative as given by (3.1). The former is corrected to T = 290.45 K while both of the above are averaged over the 6 fields. Standard deviations follow average values in parentheses.

Table 5: *Change in magnetic moment/gram of Ni alloys with temperature and, at 290.45 K, relative to matching Ni standards.*

Solute	Label	c(at.%)	$100\left(1 - \frac{\sigma(0)}{\sigma(c)}\right)$	$-\left(\frac{1}{\langle\sigma\rangle}\frac{\Delta\sigma}{\Delta T}\right)10^4$	Day
	N59(D)	0.147(1)	-1.160(7)	4.99(1)	89.5
	"		-1.163(6)	5.19(6)	1.0
	N34(D)	0.262(2)	-2.027(9)	5.06(2)	89.0
Ti	"		-2.026(10)	5.32(4)	2.0
	N35(D)	0.538(11)	-4.139(8)	5.37(5)	88.0
	"		-4.135(8)	5.66(2)	3.0
	N14(D)	0.910	-7.631(9)	5.93(8)	86.0
	"		-7.624(9)	6.27(2)	4.0
	N58(D)	0.150(1)	-1.322(1)	4.99(3)	66.0
V	N53(N)	0.251(11)	-1.953(4)	5.13(2)	91.0
	N32(D)	0.537(13)	-2.939(8)	5.21(3)	67.0
	N13(C)	0.923(5)	-9.038(2)	6.26(1)	74.0
	N61(C)	0.144(6)	-1.391(2)	5.00(3)	78.0
	"		-1.389(5)	5.10(19)	26.0
Cr	N33(C)	0.233(30)	-2.424(2)	5.14(3)	79.0
	"		-2.423(1)	5.14(1)	28.0
	N21(D)	0.545(5)	-5.467(9)	5.60(2)	81.5
	"		-5.467(9)	5.74(31)	24.0
	N24(N)	0.886(24)	-9.322(4)	6.19(3)	29.0
Mn	N12(D)	0.110(15)	+0.486(6)	5.07(1)	68.0
	NIE(G)	0.750	+2.661(5)	5.36(9)	104.0
	N45(C)	0.252(7)	+0.932(0.3)	4.80(1)	73.0
Fe	N54(D)	0.542(7)	+1.973(5)	4.66(3)	63.5
	N11(N)	0.922(3)	+3.461(5)	4.66(1)	93.0
	"		+3.458(4)	4.65(3)	92.0
	N27(D)	0.241(17)	+0.553(8)	4.78(4)	65.0
	N06(A)	0.526(23)	+1.387(1)	4.48(5)	101.0
	"		+1.384(3)	4.60(2)	103.0
Co	N52(C)	0.777(23)	+1.900(1)	4.62(2)	77.0
	N07(A)	0.944(28)	+2.196(4)	4.58(2)	100.0
	N08(D)	1.198(14)	+2.800(9)	4.51(5)	64.0
	N10(D)	1.517(13)	+3.444(6)	4.40(3)	67.5
	N01(D)	0.262(5)	-0.576(10)	4.86(2)	32.0
	N02(D)	0.559(22)	-1.198(9)	4.97(1)	33.0
	N51(D)	0.910	-1.702(6)	5.04(1)	34.0
Cu	N03(A)	0.957(44)	-2.004(1)	5.08(5)	102.0
	N04(B)	1.220(14)	-2.772(14)	5.21(1)	99.0
	"		-2.770(15)	5.28(1)	96.0
	N05(N)	1.532(3)	-3.419(6)	5.34(2)	90.0
	N37(D)	0.256(4)	-1.947(8)	5.07(3)	63.5
Zr	N38(B)	0.547(3)	-3.654(12)	5.14(3)	95.0
	N29(D)	0.888(1)	-3.401(4)	4.94(3)	60.0

Table 5 (continued)

Solute	Label	c(at.%)	$100\left(1 - \frac{\sigma(0)}{\sigma(c)}\right)$	$-\left(\frac{1}{\langle\sigma\rangle}\frac{\Delta\sigma}{\Delta T}\right)10^4$	Day
	N43(D)	0.252(7)	-2.513(8)	5.18(6)	47.0
Nb	N56(D)	0.573(6)	-5.707(8)	5.80(7)	48.0
	N25(D)	0.906(2)	-10.091(8)	6.28(6)	49.0
	N41(D)	0.245(14)	-2.819(8)	5.15(4)	62.0
Mo	N42(C)	0.550(1)	-5.439(1)	5.61(3)	73.5
	N18(A)	0.905(5)	-11.630(6)	6.67(9)	103.5
	N50(D)	0.257(4)	-0.197(9)	4.80(3)	61.0
Pd	N57(C)	0.549(1)	-0.456(1)	4.89(2)	75.0
	N26(B)	0.909(3)	-0.708(11)	4.93(3)	97.0
Hf	N60(D)	0.262(1)	-2.268(6)	5.09(4)	58.0
Ta	N39(C)	0.259(2)	-2.269(1)	5.11(2)	59.0
	N28(B)	0.901(1)	-10.839(15)	6.28(3)	98.0
	N55(D)	0.252(8)	-3.445(9)	5.22(1)	57.0
W	N49(B)	0.543(7)	-7.498(15)	5.77(2)	94.0
	N20(D)	0.912(1)	-11.621(9)	6.41(4)	55.0
Pt	NIF(G)	0.750	-2.522(2)	5.05(10)	105.0
	N17(D)	0.902(2)	-2.707(9)	5.11(2)	56.0
	N30(D)	0.257(2)	-1.003(11)	4.78(7)	44.0
Au	N16(D)	0.541(3)	-2.375(9)	5.04(1)	45.0
	N15(D)	0.913(1)	-3.863(9)	5.16(3)	87.0
	"		-3.862(9)	5.14(6)	46.0

Letters in parentheses following labels indicate the standard (one of A, B, C, D, or G) used. A letter N indicates that there is no matching standard and in these cases C was used since its height to diameter ratio is the nearest. Concentrations are as determined by neutron activation except where no uncertainty is given in which case they are "as made" values.

Reproducibility of relative moment change is indicated by the agreement between results of the 12 (~20% of total number) samples for which two runs were taken. Note that, excepting N14 (Ti 0.91%), repeated results agree to within 4 parts in a hundred thousand. Standard deviations over the 6 measurements at fields of ±1.2, ±1, ±0.8 kG cannot be taken as

uncertainties since these numbers reflect, to a large degree, the field dependence of sample moments. Preferred data are the first set (row) in all cases. Temperature derivatives are more well behaved for these data. That is, they are more nearly linear with concentration and extrapolate back to values which agree with the average, $-4.88(10^{-4})$, of all Ni standard runs. For example consider the Ti series, for which measurements were made in March (second row) and June of 87. The June data (first row) extrapolate back to a value closer to the average. Notice that in many cases repeated values do not agree within uncertainties. Comparison of the reproducibility of data with the size of the signal change for $|\Delta T| = 3.1$ K does not account for the magnitude of the noise, suggesting possible problems with the temperature measurement itself. However, a great deal of data is available for the Ni standards, particularly NID. The fact that the average, $-4.88(10^{-4})$. over NID data agrees well with the value extracted (averaged over the 3 fields we used) from Pauthenet's[28] fit to his data, $-(4.87\pm.03)\ 10^{-4}$, is reassuring. Here, as compared with moment changes above, standard deviations more nearly reflect uncertainties. The relative time, in days, that the run was made is given in the last column. This illustrates any dependence of reproducibility on the time between runs.

Application of results to B_{hf} determination

As discussed in the introduction, these experiments were motivated by the need to correct data of B_μ for these alloys for the Lorentz field, B_L. In order to convert the above data into a field (moment/unit volume) knowledge of sample density is necessary. Low angle X-ray diffraction data have been taken by P. Dassonvalle for this purpose (currently unavailable). The quantity of interest is $(1/B_L)(\partial B_L/\partial c)$. Excessive moment reduction due to voids in one of a sample-standard pair may contribute error, especially for samples measured against standards B or D for which measured densities are anomalously smaller than expected. A worst case estimation of ~300 ppm is made from the model presented in chap. 2. An experimental estimation of the magnitude of moment reduction for samples of this kind could be obtained by making measurements before and after a hole was drilled in a sample. Grain size may also make

a significant contribution to error due to the fact that grain sizes decrease with increasing concentration. Single crystal magnetization data[9] indicate that moments change by ~300 ppm from hard to easy directions. The question is; does the averaging over 20 orientations deal with this problem effectively?

At the time of writing, magnetization and muon results have not been combined. Since neither μSR or density results are available another means of assessing the reliability of the results reported here is desirable. This is done by comparison of the concentration dependence of relative moment changes with those expected expected from theory.

3.3 Concentration dependence of Ni alloy magnetic moment per gram

The rate of change of magnetization of Ni with alloy concentration has played an important role in the history of ferromagnetism in metals[22]. Since the studies of Sadron[23] and Marion[24] the essential facts have been known. Concentration dependence is found to depend on the difference between numbers of electrons outside of inert gas cores for solute and Ni host. For transition elements near Ni an average moment change of $-\Delta Z\mu_B$ (where $\Delta Z = Z_S - Z_{Ni}$ is the excess nuclear charge) per atom of solute is seen. While for early transition metal solutes a reduction by $(10 + \Delta Z)\mu_B$ is found, the transition occurring between Cr and Mn for the 3d series. The basic cause of the above behaviour is that solvent conduction electrons of d character, having the necessary energy and symmetry, are required to screen local perturbations of charge neutrality produced by solute atoms. Physically appealing explanations of the above two expressions are offered by Friedel's sum rules of magnetization and charge[32]. In a recent series of papers, Stefanou et al.[33], Zeller[34], and Blügel et al.[34] have used state-of-the-art LSDF (local spin density functional) methods to understand the role of screening by d and sp states in determining the moment on 3d and 4d transition metal solute atoms and the perturbation of the moments of the surrounding Ni atoms. Including exchange as a local potential[34] and assuming the Ni structure, ground state LDOS (local density of states : $\uparrow$ and $\downarrow$) are calculated[33] for clusters of up to 55 atoms (the 1st, 2nd, 3rd, and 4th n.n. shells, which contain 12, 6, 24, and 12 atoms

respectively). From these LDOS the spin density associated with these sites are obtained. A spin only moment of Ni of 0.538 μ_B is calculated using g_e the g-factor of the electron. Tables give solute atom moment as the first entry followed by the excess moment over that of Ni for impurity and four n.n. sites. A weighted sum over the excess values give the net extra moment for one solute atom. These spin-only results are converted to magnetic moment by assuming something about the g-factors, which they do not calculate. The simplest assumption[33] is that the solute has its g-factor, to be deduced from whatever experiments shed light on the behaviour of the solute in various metallic environments, while all the Ni atoms have the g-factor of pure Ni, which is determined by ferromagnetic resonance (FMR). Defining p as the local moment of the solute atom, and the weighted sum as w, the total moment per unit mass at 0 K for an alloy of concentration c and atomic weight A_S would be,

$$\sigma(0,c) = \frac{(((w - p + 0.583)g_{Ni} + pg_S)c + 0.583g_{Ni}(1 - c))\mu_B N_0}{cA_S + A_{Ni}(1-c)}, \quad (3.2)$$

where N_0 is Avogadro's number. A solute atom carries a local moment $(g_S/g_e)p$ and the perturbation of the surrounding Ni atoms gives an additional moment per solute atom $(g_{Ni}/g_e)(w-p+0.583)$. The numbers for w and p are given as ΔM (or ΔM^{cl}) and M^{imp} in Table I of Stefanou et al.[33], e.g. w = -5.319 (or 5.300) and p = -1.700 for Cr. From (3.2) one obtains the following expression for the y(0,c), the relative change in the 0 K magnetic moment with atomic concentration:

$$y(0,c) = \frac{\sigma(0,c) - \sigma(0,0)}{\sigma(0,0)} = c\,\frac{\frac{w}{0.583} - \left(1 - \frac{g_S}{g_{Ni}}\right)\frac{p}{0.583} + 1 - \frac{A_S}{A_{Ni}}}{1 - c\left(1 - \frac{A_S}{A_{Ni}}\right)}. \quad (3.3)$$

In ignorance (our present state) of g-factors (3.3) reduces to,

$$y(0,c) = \frac{\sigma(0,c) - \sigma(0,0)}{\sigma(0,0)} = c\,\frac{\frac{w}{0.583} + 1 - \frac{A_S}{A_{Ni}}}{1 - c\left(1 - \frac{A_S}{A_{Ni}}\right)}. \qquad (3.4)$$

That w is an excess shows clearly here, because w=0 gives no effect on the moment other than the change in atomic weight:

$$y(0,c) = \frac{\sigma(0,c) - \sigma(0,0)}{\sigma(0,0)} = c\,\frac{1 - \frac{A_S}{A_{Ni}}}{1 - c\left(1 - \frac{A_S}{A_{Ni}}\right)}. \qquad (3.5)$$

In the most extreme case of Au, where $(1 - A_S/A_{Ni}) = -3$, (3.5) gives a 3% decrease in slope.

Given a set of properly prepared spheres of dilute Ni alloys and a magnetometer that measures at 4.2 K, it would be a simple matter to obtain the experimental values of y(0,c). Such experimental data are sparse, particularly for 4d and 5d solutes[34]. The data obtained here for dilute Ni alloys at T = 290.45 K and T_1 = 293.55 K are of sufficient precision that we attempt to deduce y(0,c) from measurements of y(T,c) and $\Delta_2(T,T_1,c)$ where

$$y(T,c) = \frac{\sigma(T,c) - \sigma(T,0)}{\sigma(T,0)} \qquad (3.6)$$

and

$$\Delta_2(T,T_1,c) = \frac{(\sigma(T,c) - \sigma(T_1,c)) - (\sigma(T,0) - \sigma(T_1,0))}{\sigma(T,0) - \sigma(T_1,0)}. \qquad (3.7)$$

The form of (3.7) is determined by making the simplest of physically grounded[28] assumptions about the temperature dependence of the moments per gram of Ni and its dilute alloys; that they fall off with temperature as the simple power law,

$$\frac{\sigma(T,c) - \sigma(T,0)}{\sigma(T,0)} = - A \left(\frac{T}{T_c(c)}\right)^r , \tag{3.8}$$

where r and A are the same for Ni and its dilute alloys. With (3.8) it follows that

$$\frac{\sigma(0,c) - \sigma(T,c)}{\sigma(T,c) - \sigma(T_1,c)} = \frac{\sigma(0,0) - \sigma(T,0)}{\sigma(T,0) - \sigma(T_1,0)} \tag{3.9}$$

from which, solving for the magnetization at 0 K, yields (after some manipulation) the desired expression

$$y(0,c) = y(T,c) \frac{\sigma(T,0)}{\sigma(0,0)} + \Delta_2(T,T_1,c) \left(1 - \frac{\sigma(T,0)}{\sigma(0,0)}\right). \tag{3.10}$$

The ratio $\sigma(290.45\ K,0)/\sigma(0,0) = 0.9432$ is accurately known from the work of Pauthenet[28]. That these are dilute alloys, with $0.0011 < c < 0.015$, should give some confidence in the assumption of constant r and A ("corresponding states" for Ni and its dilute alloys). It may not however be a good assumption when the solute is Mn, based on the results of NMR work by Jaccarino et al.[36]. As there is good reason to be skeptical about an extrapolation to 0 K based on measurements made at 290.45 K and 293.55K, the results are shown in fig. 3.1 as pairs with (x or +) and without (o) the Δ_2 term in (3.10) above. Theory lines (solid) are calculated using $g_s = g_{Ni}$ (so that (3.4) applies) for two values given by Stefanou et al.[33]. Broken lines are calculations using the Friedel expressions - $\Delta Z\mu_B$ and $(10 + \Delta Z)\mu_B$. Fig. 3.1(a) shows some

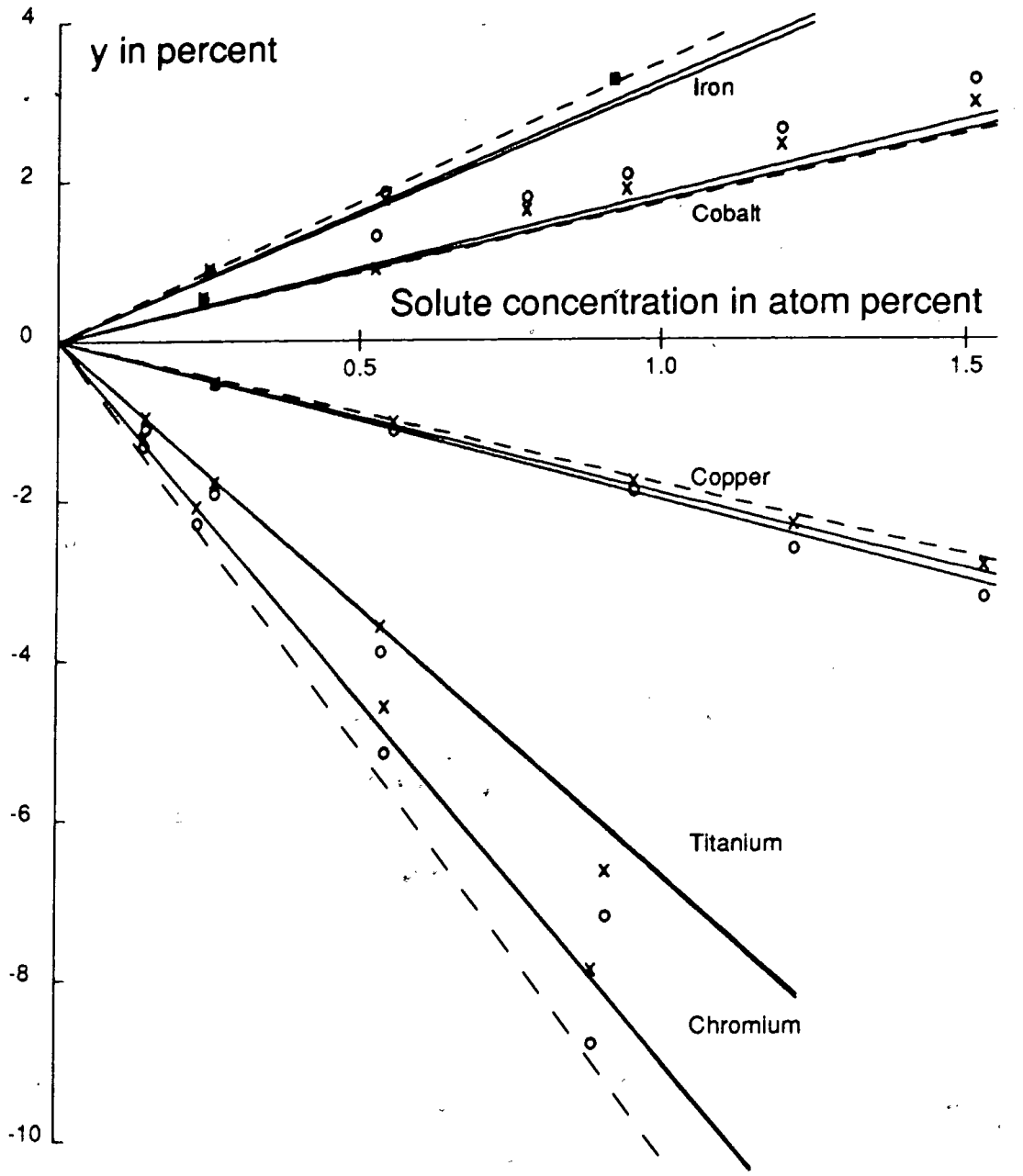

Fig. 3.1 (a) Dilute alloy series with Ni. The relative magnetic moment per unit mass $y(0,c) = (\sigma(0,c) - \sigma(0,0))/\sigma(0,0)$ obtained starting from theory (solid lines) or from measurements (× or +) using eq. 3.10. The points O are computed by setting $\Delta_2 = 0$. The theory lines are calculated using $g_S = g_{Ni}$ for two values given by Stefanou et al.[33]. (a) Some elements in the first transition series.

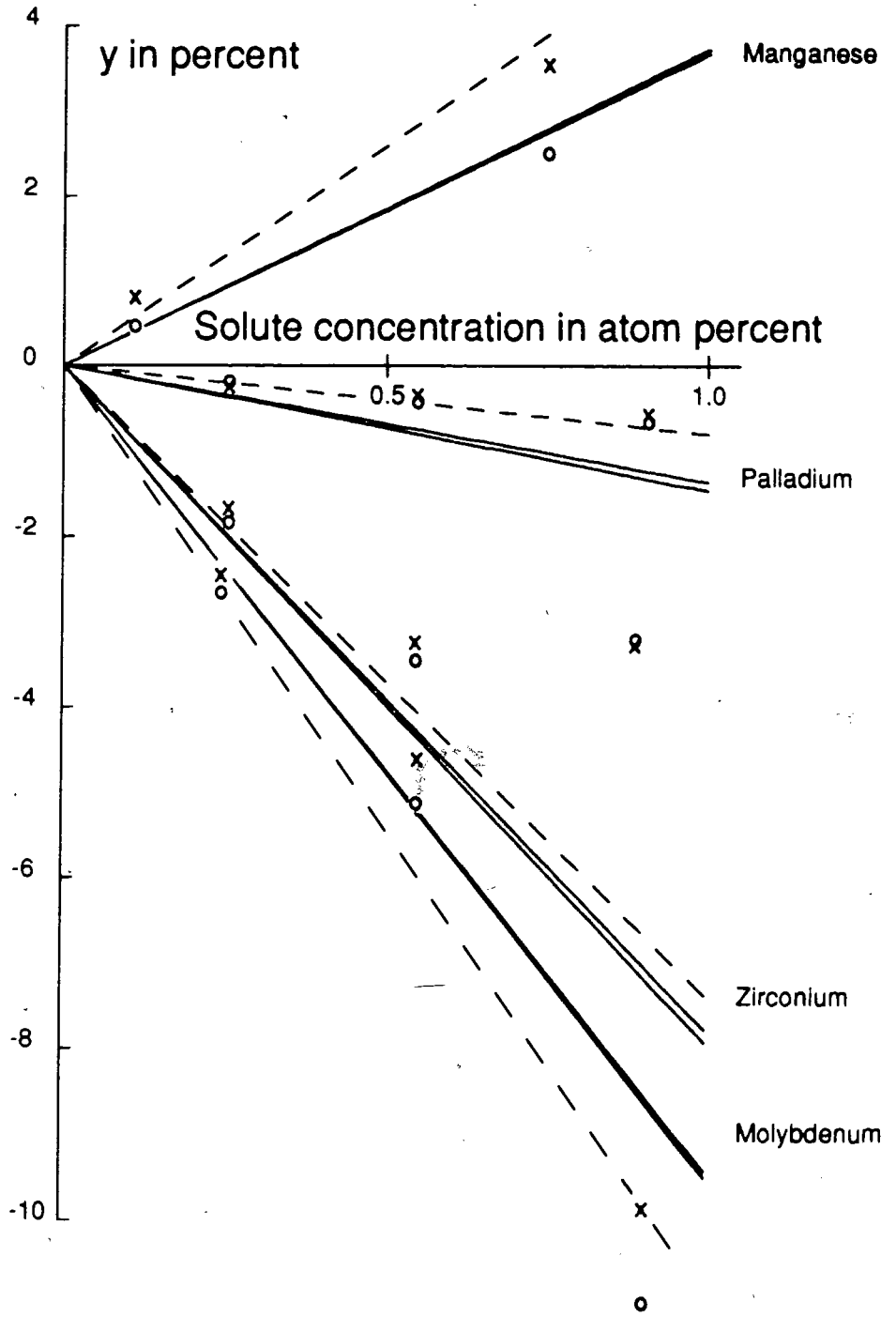

Fig. 3.1 (**b**) Dilute alloy series with Ni. The relative magnetic moment per unit mass $y(0,c) = (\sigma(0,c) - \sigma(0,0))/\sigma(0,0)$ obtained starting from theory (solid lines) or from measurements (× or +) using eq. 3.10. The points O are computed by setting $\Delta_2 = 0$. The theory lines are calculated using $g_S = g_{Ni}$ for two values given by Stefanou et al.[33]. (**b**) Some elements in the second transition series.

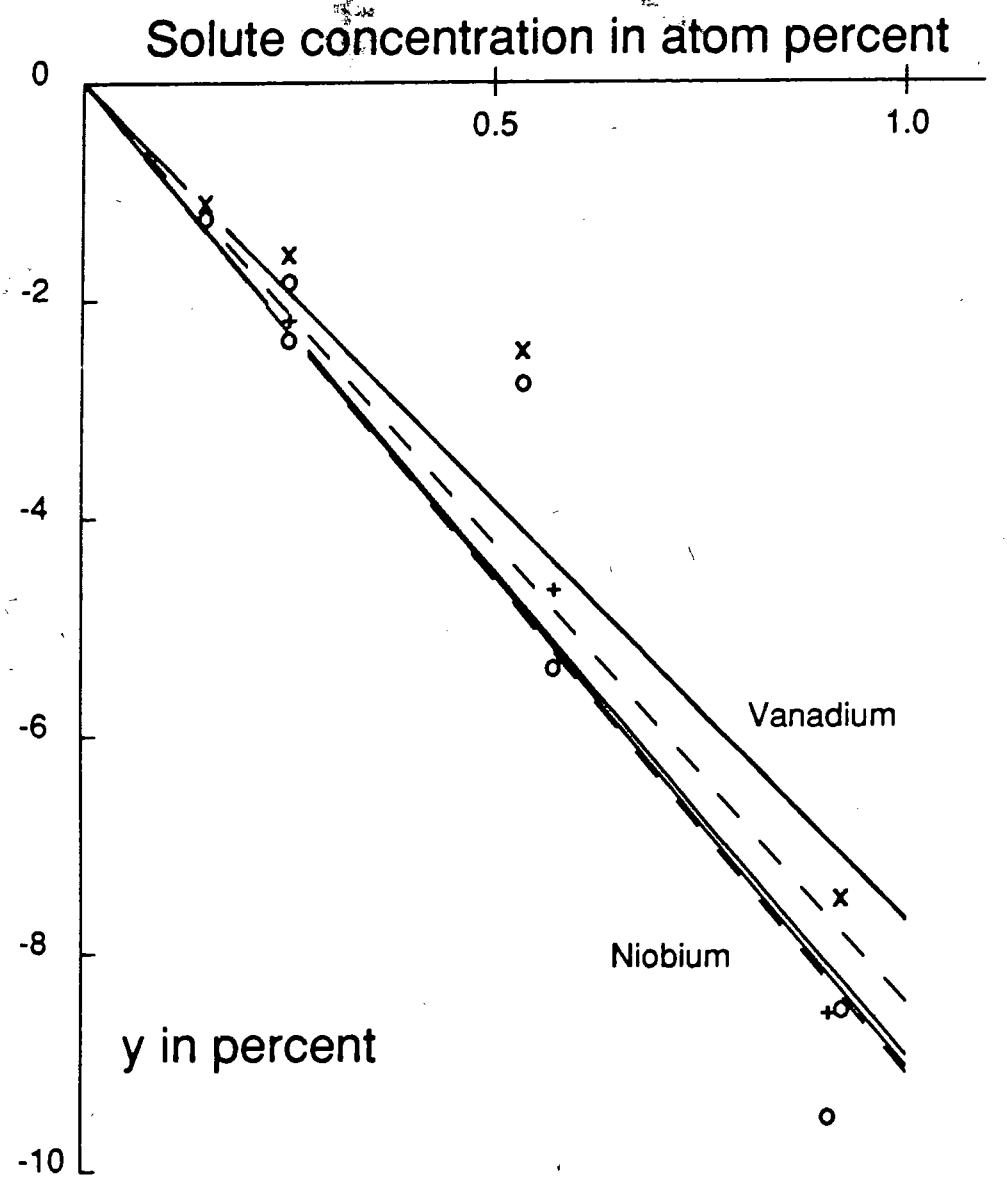

Fig. 3.1 (c) Dilute alloy series with Ni. The relative magnetic moment per unit mass $y(0,c) = (\sigma(0,c) - \sigma(0,0))/\sigma(0,0)$ obtained starting from theory (solid lines) or from measurements (× or +) using eq. 3.10. The points O are computed by setting $\Delta_2 = 0$. The theory lines are calculated using $g_S = g_{Ni}$ for two values given by Stefanou et al.[33]. (c) For alloys where the moment decreases rapidly with concentration, precipitation would increase the magnetization.

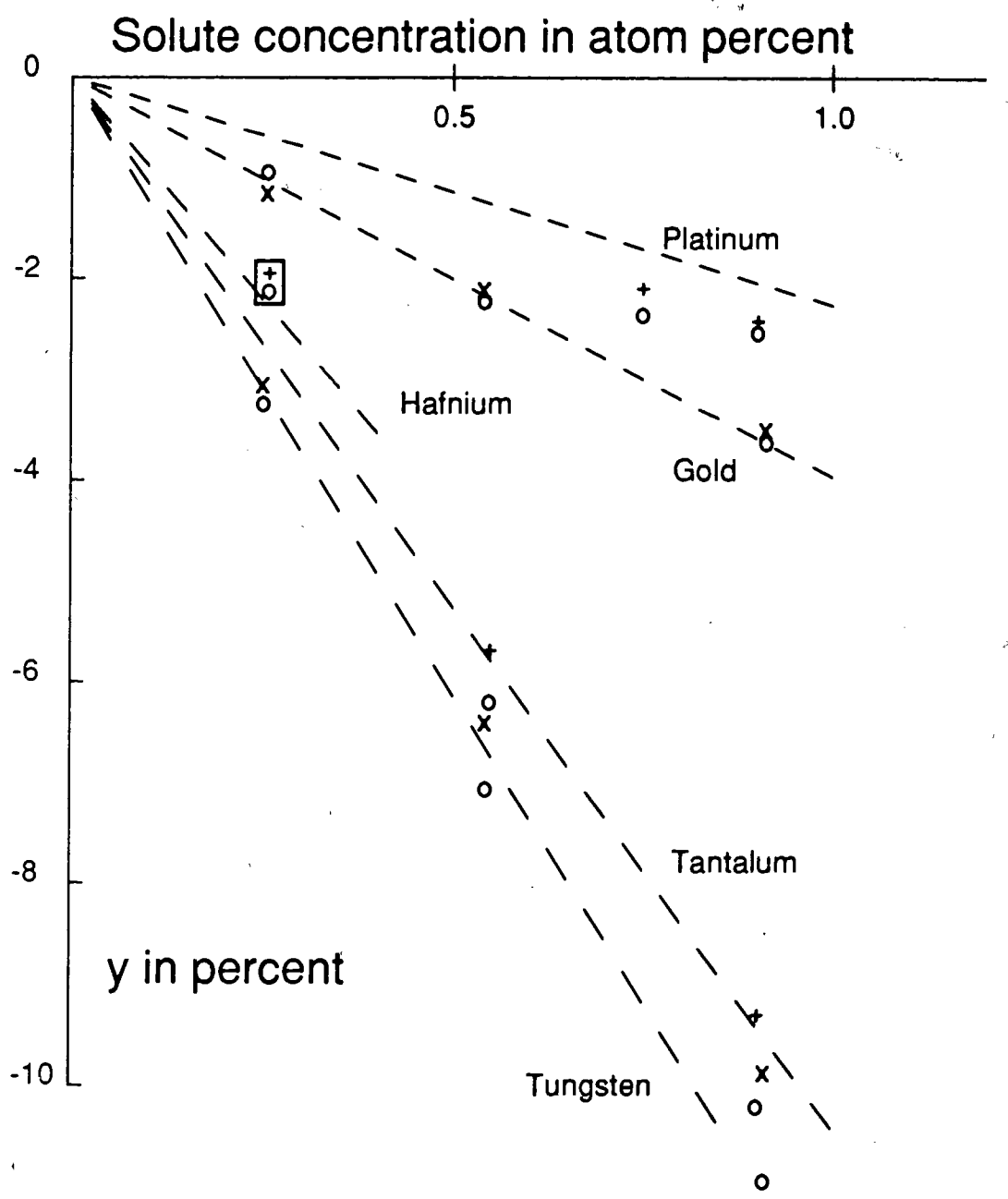

Fig. 3.1 (d) Dilute alloy series with Ni. The relative magnetic moment per unit mass $y(0,c) = (\sigma(0,c) - \sigma(0,0))/\sigma(0,0)$ obtained starting from theory (solid lines) or from measurements (× or +) using eq. 3.10. The points O are computed by setting $\Delta_2 = 0$. The theory lines are calculated using $g_S = g_{Ni}$ for two values given by Stefanou et al.[33]. (d) Theory has no been carried out for the 5d solutes. The data points for the single Hf sample are buried under the Ta points in the box.

(results for Mn and V are shown in (b) and (c) respectively) elements the first transition series. Experiment and LSDF both match the Friedel expression for Ti. LSDF seems to be slightly low for Cu, Co and Fe however. For Pd LSDF predicts a moment on the Pd atom less than that of Ni, where as this and other[31] experiments indicate (see fig. 3.1(b)) that Pd has the same effective moment as Ni in agreement with the expression - $\Delta Z\mu_B$ where $\Delta Z=0$.

For alloys with early solutes, where the moment decreases rapidly with concentration, precipitation would increase the moment per gram since it removes the reduction of surrounding Ni moments and replaces it with a (smaller) reduction resulting from the incorporation of Ni and solute in non-magnetic phases. As shown in fig. 3.1(b), this is evident for the 0.0055 V alloy and especially, 0.0091 Zr, and 0.0055 Zr alloys for which there are corroborating indications of precipitation (see chap. 2).

As shown in fig. 3.1(b), alloys with Mn show a large temperature dependence leading to an overestimation of the low temperature moment. Jaccarino et al.[36] offer an explanation for their NMR data on Fe-Mn alloys that may apply in this case.

LSDF calculations of this sort have not been carried out for the 5d solutes. Our 5d data are shown in fig. 3.1(d). Data points for the single Hf sample are buried under the Ta points in the box. The effective Pt moment is less than that of Ni in agreement with the results of Sadron[30] and Marion[31].

3.4 Conclusions

The above agreement of our data with theory suggests that they may be useful in extracting the hyperfine field, B_{hf}, from the results of muon experiments of Grynszpan et al.[15] which motivated this work. Results of the combination may shed some light on the accuracy of moment determination. A highly undesirable set of sample characteristics from the point of view of magnetometry have resulted in the development of an instrument of considerable precision and dynamic range. A very similar instrument, the primary difference being the use of a commercial integrating DVM for the integration of induced signal, was developed by Rebouilliat[37].

Reproducibility and linearity are very similar for the two magnetometers. This device, as part of a high field (100 kG), low temperature (4.2 K) system, is the one used by Pauthenet[28] to obtain the results we have used to compare our data to the LSPD calculations.

References

1 S. Foner, Rev. Sci. Instr., 548 (1959)

2 P. Weiss and R. Forrer, Ann. de Physique [10] **12**, 279 (1929)

3 L.D. Landau & E.M. Lifshitz, *The Classical Theory Of Fields*, Pergamon Press, 2nd Ed., (1962)

4 L.D. Landau & E.M. Lifshitz, *Electrodynamics of Continuous Media*, Pergamon Press, 1st Ed., (1960)

5 R.M. White, *Quantum Theory of Magnetism*, Springer-Verlag, Berlin (1983)

6 W.F. Brown, Jr., *Micromagnetics*, Wiley, (1963)

7 A.S. Arrott, J. Appl. Phys., **61** (8), 4219, (1987)

8 S. Chikazumi, *Physics of Magnetism*, Wiley; New York (1964)

9 E.P. Wohlfarth, in vol. 1 of *Ferromagnetic Materials*, Ed. E.P. Wohlfarth, North-Holland, Amsterdam (1980)

10 E.C. Stoner, Repts. Prog. Phys., **11**, 43, (1946-7)

11 N.W. Ashcroft & N.D. Mermin, *Solid State Physics*, Holt, Rinehart & Winston, (1976)

12 H.A. Lorentz, *The Theory of Electrons*, Dover Ed., (1952)

13 A. Arrott and H. Sato, Phys Rev., **114**, 1420 (1959)

14 R.M. Bozorth, *Ferromagnetism*, D. Van Nostrand Co., Princeton, N.J., (1951)

15 R.I. Grynszpan‡, P. Dassonvalle, and P. Langlois‡, Centre d'Etudes de Chimie Metallurgique, Vitry, France

‡Present address: Laboratoire Microstructure et Méchanique des Matériaux, Ecole Nationale Supérieure d'Arts et Métiers, 151, boulevard de l'Hôpital, 75640 PARIS CEDEX 13

16 P. Dassonvalle, PhD Thèse, Université de Paris VI, (1986)

17 A. Schenck, *Muon Spin Rotation Spectroscopy, Principles and Applications in Solid State Physics*., Adam & Hilger Ltd., Bristol & Boston, (1987)

18 D. Hunter, A.S. Arrott, R.I. Grynszpan, P. Dassonvalle, and P. Langlois, J. Appl. Phys., **63**, 3043-3045 (1988)

19 W. B. Pearson, *A Handbook of Lattice Spacings and Structures of Metals and Alloys*, Pergamon Press, (1964)

20 L. I. Mirkin, *Handbook of X-ray Analysis of Polycrystalline Materials*, Consultants Bureau, New York, (1964)

21 C. Winter, PhD Thesis, Simon Fraser University, (1982)

22 K. Borer & G. Fremont, Nucl. Instr. and Meth., **154**, 61 (1978)

23 B. Heinrich, A.S. Arrott, & S.D. Hanham, J. Appl. Phys., **50**, 2146-2148 (1979)

24 Personal communication: Pete Peterson of the MAGNION division of Walker Scientific, Ph. (617) 852 3674 ext. 505

25 P. Weiss, Ann. de Physique [10] **5**, 171 (1926)

26 A.I.P. Handbook, 2nd Ed., McGraw-Hill, (1963)

27 A. Arrott and J. E. Noakes, in *Iron and Its Dilute Solid Solutions*, Edited by C.W.Spenser and F.E. Werner (Interscience, New York, 1964), p. 91.

28 R. Pauthenet, J. Appl. Phys., **53**, 8187 (1982), **53**, 2029 (1982)

29 A.P. Malozemoff, A.R. Williams, and V. L. Moruzzi, Phys. Rev. B, **29-2**, 1620 (1984): A.R. Williams, V. L. Moruzzi, A.P. Malozemoff, and K. Terakura, IEEE Trans. Magn., **MAG-19**, 1983 (1983) and references therein.

30 C. Sadron, C. R. Acad. Sci., **190**, 1330 (1930); Ann. Phys. **17**, 371 (1932)

31 V. Marion, Ann. Phys., **7**, 457 (1932)

32 J. Friedel, Nuovo Cimento, **10-2**, 287 (1958)

33 N. Stefanou, A. Oswald, R. Zeller and P.H. Dederichs, Phys. Rev., **B35**, 6911-6922, (1987)

34 R. Zeller, J. Phys. F, **17**, 2123-2137 (1987)

35 S. Blügel, H. Akai, R. Zeller, and P.H. Dederichs, Phys. Rev. **B35**, 3271 (1987)

36 V. Jaccarino, L.R. Walker, and G.K. Wertheim, Phys. Rev. Letters, **13**, 752 (1964)

37 J.P. Rebouilliat, PhD Thèse, Univ. Grenoble (1972)